Stony Brook University

Hydrodynamics and transport in low-dimensional interacting systems

A Dissertation Presented

by

Manas Kulkarni

to

The Graduate School

in Partial Fulfillment of the Requirements

for the Degree of

Doctor of Philosophy

in

Physics

Stony Brook University

August 2011

Stony Brook University

The Graduate School

Manas Kulkarni

We, the dissertation committee for the above candidate for the Doctor of Philosophy degree, hereby recommend acceptance of this dissertation.

Alexander G. Abanov - Advisor
Associate Professor, Department of Physics and Astronomy

Robert M. Konik
Associate Physicist, Brookhaven National Laboratory

Marivi Fernandez-Serra - Committee Chair
Assistant Professor, Department of Physics and Astronomy

Dominik Schneble
Assistant Professor, Department of Physics and Astronomy

Alexander Kirillov
Associate Professor, Department of Mathematics

This dissertation is accepted by the Graduate School

Lawrence Martin
Dean of the Graduate School

Abstract of the Dissertation

Hydrodynamics and transport in low-dimensional interacting systems

by

Manas Kulkarni

Doctor of Philosophy

in

Physics

Stony Brook University

2011

Recent ground-breaking experiments have realized strongly interacting quantum degenerate Fermi gas in a cold atomic system with tunable interactions. This has provided a table-top system which is extremely hydrodynamic in nature. This experimental realization helps us to investigate several aspects such as the interplay between nonlinearity, dissipation and dispersion. We find, for instance, that the dynamics in such a system shows near perfect agreement with a hydrodynamic theory. In collaboration with the group of John Thomas at Duke we interpreted studies of collision of two strongly interacting Fermi gases that led to shock waves which are a hallmark of nonlinear physics. Due to reasons such as the nature of interactions, higher dimensionality, these cold atomic systems are non-integrable and moreover the underlying field theory construction is mostly phenomenological in nature.

On the other hand there are certain one-dimensional systems which are not only integrable but also facilitate more formal and rigorous

ways of deriving the corresponding integrable field theories. One such family of models is the family of Calogero models (and their generalizations). They provide an extraordinary insight into the field of strongly correlated systems and hydrodynamics. We study the collective field theory of such models and address aspects of nonlinear physics such as Spin-Charge Interaction, Emptiness Formation Probability, Solitons etc; We derive a two-component nonlinear, nonlocal, integrable field theory. We also show that the Calogero family which is integrable even in an external harmonic trap (usually unavoidable in cold atom setups) is relatively "short ranged" thereby qualifying as a toy model for cold atom experiments.

Transport in certain strongly correlated systems (impurity models) was studied using few low-dimensional techniques such as a 1/N diagrammatic expansion, Slave Boson Mean Field Theory and the Bethe Ansatz. A mesoscopic setup such as parallel quantum dots forms an ideal platform for such an investigation and comparison between different low-dimensional techniques. We studied transport, correlations and nature of the ground state of double quantum dots. We probed several non-perturbative aspects of this double-impurity model. For example, we showed that the RKKY interaction in closely spaced dots can be non-ferromagnetic due to its non-pertubative nature. This study helped us to point some discrepancies between different methods (such as the Numerical Renormalization Group). We give possible reasons for these discrepancies.

To my family.

Contents

List of Figures **xi**

List of Tables **xvi**

Acknowledgements **xvii**

List of Publications **xx**

1 Introduction and Outlook of the thesis work **1**

1.1 Hydrodynamics of low-dimensional interacting systems 1

1.1.1 Hydrodynamics in Cold Atomic systems 2

1.1.2 Collective Field Theory for Integrable Models 3

1.2 Transport and Correlations in low dimensional strongly correlated electrons 5

1.2.1 RKKY interaction and nature of the ground state of double quantum dots arranged in parallel: Slave Boson Mean Field Theory and the Bethe Ansatz 6

1.2.2 1/N diagrams for coupled parallel quantum dots: Transport, Correlations and evidence of Fermi Liquid 6

2 Shock waves in a strongly interacting Fermi gas **8**

2.1 Introduction 8

2.2 Experiment: colliding fermi-clouds 9

2.3 Theory: Nonlinear hydrodynamics of quantum matter and dimensional reduction 11

2.4 Model and the grid method 16

2.5 Smoothed particle formulation of nonlinear hydrodynamics . . 17

2.6 Results from smoothed particle hydrodynamics 19
2.7 Conclusion 21

3 Nonlinear dynamics of spin and charge in the spin-Calogero model 25
3.1 Introduction 25
3.2 Free fermions with spin 28
3.3 The spin-Calogero model 31
3.4 Gradientless hydrodynamics of the spin-Calogero model 32
3.4.1 Spinless limit 36
3.4.2 $\lambda = 0$ – free fermions with spin 36
3.4.3 $\lambda \to \infty$ limit. 36
3.5 Equations of motion and separation of variables 36
3.5.1 Equations of motion 36
3.5.2 Free fermions ($\lambda = 0$) and Riemann-Hopf equation . . . 37
3.5.3 Riemann-Hopf Equations for the sCM 40
3.6 Freezing trick and hydrodynamics of the Haldane-Shastry model 41
3.6.1 $O(\mu)$ 43
3.6.2 $O(1)$ 43
3.6.3 $O(1/\mu)$ 44
3.6.4 Evolution equations for the Haldane-Shastry model from the freezing trick 44
3.7 Illustrations 44
3.7.1 Charge dynamics in a spin-singlet sector 45
3.7.2 Dynamics of a polarized center 45
3.7.2.1 Applicability of gradientless hydrodynamics . 46
3.7.2.2 Free fermions with spin: $\lambda = 0$ 46
3.7.2.3 λ-dependence of spin and charge dynamics . . 47
3.8 Conclusions 48

4 Cold Fermi-gas with inverse square interaction in a harmonic trap 51
4.1 Introduction 51
4.2 Collective Field theory 54
4.3 Static solutions 56

4.4 Dynamics 61
4.5 Conclusions 66

5 Emptiness and Depletion Formation Probability in spin models with inverse square interaction 69
5.1 Introduction 69
5.2 Two-fluid description 73
5.3 The instantonic action 75
5.4 Depletion Formation Probability 78
5.4.1 Asymptotic singlet state 79
5.5 Emptiness Formation Probability 80
5.5.1 Free fermions with spin 81
5.5.2 Splinless Calogero-Sutherland model 81
5.5.3 Probability of Formation of Ferromagnetic Strings . . . 81
5.5.4 The freezing limit 82
5.5.5 Haldane-Shastry model 83
5.6 Spin Depletion Probability 84
5.7 Charge Depletion Probability 86
5.8 Discussion of the results 88
5.9 Conclusions 90

6 The RKKY Interaction and the Nature of the Ground State of Double Dots in Parallel 93
6.1 Introduction 93
6.2 Model Studied 95
6.2.1 Bethe Ansatz 96
6.2.2 Slave Boson Mean Field Theory 98
6.3 Results 100
6.3.1 Zero Temperature Conductance 100
6.3.2 Finite Temperature Conductance 105
6.3.3 Spin-Spin Correlation Function 109
6.3.4 Impurity Entropy 111
6.4 Discussion and Conclusions 111

7 $1/N$ diagrammatic expansion for coupled parallel quantum dots 116
7.1 Introduction . . . 116
7.2 Model studied and method used . . . 117
7.3 Results . . . 119
7.3.1 Greens Function Matrix . . . 119
7.3.2 Partition function and dot-occupancy . . . 121
7.3.3 Friedel Sum Rule (FSR) for double quantum dots . . . 122
7.3.3.1 Friedel Sum Rule. . . . 122
7.3.3.2 Proof that FSR is satisfied perturbatively for double quantum dots . . . 123
7.3.3.3 Evaluation of conductance using FSR and $1/N$ diagrams . . . 123
7.4 Discussions and Conclusions . . . 124

Bibliography 125

A Asymptotic Bethe Ansatz solution of the spin Calogero Model and separation of variables in hydrodynamics 140

B Hydrodynamic velocities 144

C Hydrodynamic regimes for the spin-Calogero model 147
C.1 Conserved densities and dressed Fermi momenta . . . 147
C.2 Complete Overlap Regime (CO) . . . 150
C.3 Partial Overlap Regime (PO) . . . 151
C.4 No Overlap Regime (NO) . . . 152
C.5 All cases combined . . . 153

D Hydrodynamic description of Haldane-Shastry model from its Bethe Ansatz solution 156

E Exact solution for Riemann-Hopf equation in arbitrary potential 161

F Action for the DFP solution 164

G Linearized Hydrodynamics and DFP **168**

H Analysis of the Ground State Entropy via the TBA Equations **171**

I Derivation of the Conductance in SBMFT **176**

J SBMFT for double dots in the symmetric case **178**

List of Figures

2.1 False color absorption (in situ) images of the atomic cloud at different time points during the collision[1]. Time evolution is from left to right (0 ms, 2 ms, 4 ms, 6 ms, 8 ms). The atoms are divided into two clouds then accelerate towards each other. As the two clouds collide a sharp rise in density can be seen at the center of the trap. Over time the region of high density evolves from a “peak-like” shape into a “box-like” shape. The central zone in the last two coloumns exhibits first evidence of shock wave formation in a unitary Fermi-gas. The length of the cigar is about 400 μm 10

2.2 1D density profiles divided by the total number of atoms versus time for two colliding unitary Fermi gas clouds. The normalized density is in units of $10^{-2}/\mu$m per particle. Red dots show the measured 1D density profiles. Black curves show the simulation, which uses the measured trap parameters and the number of atoms, with the kinetic viscosity as the only fitting parameter. 23

2.3 (Left) The process of equilibration by molecular dynamics of pseudo-particles in presence of a "knife". The x-axis is time and the y-axis are the positions of pseudo-particles. (Right) Red denotes the density obtained from the position of the pseudo-particles and black denotes the analytical formula. 24

2.4 World-line diagram depicting trajectory of pseudo-particles after removing the knife. 24

3.1 Distribution functions are shown for the three nonequivalent regimes: *Complete Overlap* in (a), *Partial Overlap* in (b) and *No Overlap* in (c). Three additional regimes exist, but are physically equivalent to the ones considered in these pictures and can be obtained by exchanging $\uparrow \leftrightarrow \downarrow$. 34
3.2 Diagram capturing all cases 35
3.3 Dynamics of density field $\rho_\uparrow(x)$ (left panel) and of velocity field $v_\uparrow(x)$ (right panel) for free a fermion case ($\lambda = 0$). The initial density profile at $t = 0$ is a Lorentzian (3.46) of height $h = 0.25$ and half-width $a = 4$. The initial velocity is zero. 39
3.4 Phase-space diagram of a hydrodynamic state characterized by four space-dependent Fermi momenta. 41
3.5 *Left panel*: Spin dynamics of polarized center for free fermions. The initial charge density profile is constant and the initial spin density profile is a Lorentzian (3.61) of a height $h = 0.25$ and a half-width $a = 4$. Profiles at times $\tau = t/2 = 0, 1, 3.5, 7$ are shown. *Right panel*: A snapshot of spin density at time $t = \tau/(\lambda + 1/2)$ for $\tau = 7$ for $\lambda = 0, 1, \infty$. 47
3.6 *Left panel*: Charge dynamics of polarized center for free fermions. The initial charge density profile is constant and the initial spin density profile is a Lorentzian (3.61) of a height $h = 0.25$ and a half-width $a = 4$. Profiles at times $\tau = t/2 = 0, 1, 3.5, 7$ are shown. *Right panel*: A snapshot of a rescaled charge density $(\lambda+1/2)(\rho_c-1)$ at time $t = \tau/(\lambda+1/2)$ for $\tau = 7$ for $\lambda = 0, 1, \infty$. 48

4.1 Phase-space picture for sCM with $\lambda = 2$ in equilibrium with an overall magnetization $\nu = 0.8$. The radii of circles are given by $\sqrt{N(2\lambda + 1)(1 - \nu)}$ and $\sqrt{N(2\lambda + 1 + \nu)}$ for inner and outer circles respectively. Particles fill the phase space uniformly with the density of two particles (up and down) per the area $2\pi(2\lambda+1)$ in the inner circle and of one particle (up) per the area $2\pi(\lambda+1)$ in the annulus area between inner and outer circles. 59

4.2 Equilibrium charge density profile for various values of coupling constant λ for fixed magnetization $\nu = 0.8$ is shown in re-scaled variables (4.20,4.21). $\lambda = 0$ corresponds to noninteracting fermions. Upon increasing the interaction strength λ the equilibrium profile eventually loses its bump feature. This prediction for the sCM is very similar to recent predictions of Ma and Yang for fermions with contact interaction[2]. 61

4.3 Equilibrium spin density profile for various values of coupling constant λ for the fixed magnetization $\nu = 0.8$. In re-scaled variables the dip in the spin density profile depends weakly on the interaction strength λ. Compare with the charge density profile of Fig. 4.2. 62

4.4 (left to right) a) Attractive knife potential in the presence of which the fermi gas is cooled. b) The distortion of phase space circles due to the knife. c) The corresponding charge density profile. The values of ν and λ are $\nu = 0.5$ and $\lambda = 2$. 62

4.5 Top Row: (left to right) Evolution of phase space for time t=0,0.08 and 0.23 respectively. We see that this is merely a rotation by angle t. Bottow Row: Corresponding charge density evolution for times t=0,0.08,0.23. The additional peak created by the attractive knife flattens and eventually splits into two peaks. The values of ν and λ are $\nu = 0.5$ and $\lambda = 2$. 64

6.1 A schematic of the double dot system. 96

6.2 The zero temperature conductance of a symmetrically coupled double dot computed using slave boson mean field theory and the Bethe ansatz. For slave bosons we assume the symmetric case $V_{ij} = 1$. 101

6.3 The number of electrons displaced by the dots, n_d of a symmetrically coupled double dot computed both using SBMFT and the Bethe ansatz. In the case of SBMFT, n_d is simply the dot occupation, $n_{dot} = \sum_{i\sigma}\langle d^\dagger_{i\sigma} d_{i\sigma}\rangle$. In the case of the Bethe ansatz, the quantity plotted is equal to the dot occupation *plus* the $1/L$ correction to the electron density in the leads induced by coupling the dots to the leads. For slave bosons we assume the symmetric case $V_{ij} = 1$. 102

6.4 The zero temperature conductance of asymmetrically coupled double dot computed using slave boson mean field theory. The conductance is plotted as a function of V_{11}. The remaining dot-lead hopping strengths are all set to 1 while $\epsilon_{d1} = -4.7$ and $\epsilon_{d2} = -4.6$. The system is in the Kondo regime. 104

6.5 The conductance and the number of displaced electrons as a function of $\epsilon_{d1} (= \epsilon_{d2})$ as computed using SBMFT and the Bethe ansatz. For slave bosons we assume the symmetric case $V_{ij} = 1$. 106

6.6 A plot of the low energy density of states, $\rho(\omega)$ for $\epsilon_{d1} = \epsilon_{d2} = -4.45\Gamma_{1,2}$ in the Kondo regime as computed using SBMFT. As we are argue in the text, this is an artifact of SBMFT (the BA shows that in this case $\rho_d(\omega)$ vanishes[3]). 107

6.7 The linear response conductance as a function of temperature of a symmetrically coupled double dot computed using both slave boson mean field theory and the Bethe ansatz. For small separation in slave boson approach we had $\epsilon_1 - \epsilon_2 = 0.05\Gamma_{1,2}$ and $\epsilon_1 = -4.1\Gamma_{1,2}$. For large separation in slave boson approach we had $\epsilon_1 - \epsilon_2 = 5\Gamma_{1,2}$ and $\epsilon_1 = -9.4\Gamma_{1,2}$. In slave bosons we consider the symmetric case $V_{ij} = 1$. 108

6.8 The spin-spin correlation function of symmetrically coupled double dot computed using slave boson mean field theory. We consider the symmetric case $V_{ij} = 1$. 110

6.9 The impurity entropy as a function of temperature of a symmetrically coupled double dot computed using slave boson mean field theory and the Bethe ansatz. For small separation in slave boson approach we had $\epsilon_1 - \epsilon_2 = 0.05\Gamma_{1,2}$ and $\epsilon_1 = -4.1\Gamma_{1,2}$. . For large separation in slave boson approach we had $\epsilon_1 - \epsilon_2 = 5\Gamma_{1,2}$ and $\epsilon_1 = -9.4\Gamma_{1,2}$. In slave bosons we consider the symmetric case $V_{ij} = 1$. 112

C.1 Phase-space diagrams of a hydrodynamic states characterized by four space-dependent Fermi momenta in three regimes CO, PO, and NO respectively. 153

List of Tables

C.1 Summary of three regimes. 149
C.2 Classification of different regimes: + indicates that the field takes positive values, − that it is negative. A blank means that its sign is arbitrary. 154

Acknowledgements

It is all too obvious that the academic training one receives during doctoral undertaking has a crucial and decisive importance insofar as it defines the broad contours, determines the overall direction and decides the fundamental orientation of one's professional and even personal life. I am overwhelmed by a sense of profound gratitude for the wholesomeness and the abundance of such a training in the hands of my teachers who have made me what I am by their precept and practice even while overlooking my limitations and shortcomings.

First and foremost, my debt to Prof. Alexander Abanov is, to say the least, immense. Apart from providing scrupulous guidance to my research work and related undertakings, he was instrumental in procuring financial support without which this work would have been impossible. My work at Brookhaven which has been an integral part of my doctoral endeavor would not have been possible without constant help and guidance of Prof. Robert Konik.

I have no words to thank both the advisors, Prof. Alexander Abanov and Prof. Robert Konik working with whom has been an edifying experience which I cherish forever. While guiding me at every step, they taught me the courage to be independent. Mathematical rigour, conceptual clarity and creative imagination constitute the fountain-head of worthwhile research and this is the thumbrule of the scientific craftsmanship. My advisors made me comprehend this truth. My relation with them has been and remains forever very special.

It is my pleasant duty to thank Prof. Alexei Tsvelik, a doyen and a luminary among the condensed matter physicists. As soon as I joined the department as a graduate student, he extended me the privilege of interacting with him and he was kind enough to consider me for including in the condensed matter theory group at Brookhaven National Laboratory. He has been a source of inspiration and encouragement. I have immensely benifited from

protracted discussions and constant interaction with him. I owe a great deal to him in relation to the intricate texture of the matrix of the discipline within which I worked.

I am obliged to my teacher Prof. Adam Durst interaction with whom has been academically highly rewarding and personally very gratifying. I cherish his goodwill and the sweet memory of working with him on two publications.

I am beholden to all my teachers at Stony Brook whose pedagogical excellence ensured that I internalized the lexicon of Fundamental Physics. Physics owes its paradigmatic status to the deep structure of its grammar to which their courses did full justice.

As I submit this thesis I am overwhelmed by the memory of my association with Prof. Bikram Phookun who taught me Physics in my undergraduate years at St. Stephens College, Delhi. As a consummate teacher and a great motivator, he inculcated in me a love for physics and made me comfortable with the intimidating demands of the subject. Prof. Subhashish Dutta Gupta of University of Hyderabad and Prof. Chandan Dasgupta of Indian Institute of Science, Bangalore obliged me by supervising my summer projects of 2003 and 2004 respectively. They ensured that even as a young student I got an idea of what it is to engage in a focussed work on a research theme. Apart from its academic dimension, my brief but memorable association with them gave me self-confidence which holds me in good stead even today. They gave me a picture of what it is to do physics. I cannot forget their warmth and academic zeal.

I would also like to place on record my deep appreciation for the valuable co-operation and enormous goodwill shown by my collaborators in research. I must specially mention here Fabio Franchini, Prof. John Thomas, James Joseph, Andrey Gromov and Sriram Ganeshan. I enjoyed every bit of my interaction with them.

I was very much touched by the interest shown by Prof. Dominik Schneble, Prof. Austen Lamacraft, Prof. Anatoli Polkonikov and Dr. Maxim Khodas in my work. My discussions with them on the topics of mutual interest were highly rewarding. I am thankful to them for the cordiality and spontaneity of their interaction with me.

My interaction with my friends in the department and outside has been

extremely refreshing. To grow with them and helping each other in growing is a memorable experience in a lifetime. They have helped me in innumerable ways apart from providing comic reliefs in an otherwise sombre atmosphere of high tension research in a redhot science. I fondly mention the names of Patty, Abhijit, Sheng, Tom, Somnath, Soumya, Prasad, Ritwik, Marija, Shivani, Sangram, Nitin, Arijeet and Prasenjit.

I place on record my deep appreciation of all the help rendered by the office staff both at the Department of Physics and Astronomy, Stony Brook University and Department of Condensed Matter Physics and Material Sciences, Brookhaven National Laboratory.

Throughout my stay at Stony Brook, I have enjoyed the emotional support provided by my parents, my brother and other near and dear ones back home in India whose pride in my work as a researcher has kept my spirits buoyant throughout. My parents' trust in me, confidence in my ability to pursue research and their conviction in the intrinsic value of academic endeavour has sustained me in every way. I cannot thank them enough.

Finally, I am highly indebted to both the Stony Brook University and Brookhaven National Laboratory for providing all facilities for research, congenial ambience and exciting environment.

List of Publications

[I] A. G. Abanov, A. Gromov, M. Kulkarni, J. Phys. A: Math. Theor. **44**, 295203 (2011)
"Soliton solutions of Calogero model in harmonic potential"

[II] J. Joseph, J. E. Thomas, M. Kulkarni, A. G. Abanov, Phys. Rev. Lett. **106**, 150401 (2011)
"Observation of shock waves in a strongly interacting Fermi Gas"

[III] M. Kulkarni and R. M. Konik, Phys. Rev. B **83**, 245121 (2011)
"The RKKY Interaction and the Nature of the Ground State of Double Dots in Parallel"

[IV] S. Ganeshan, M. Kulkarni and A. C. Durst, arXiv: 1010.2213 (2010), accepted in Phys. Rev. B.
"Berry phase contribution to quasiparticle scattering from vortices in d-wave superconductors"

[V] M. Kulkarni, S. Ganeshan and A. C. Durst, arXiv: 1006.2818 (2010), accepted in Phys. Rev. B.
"Superflow contribution to quasiparticle scattering from vortices in d-wave superconductors"

[VI] M. Kulkarni and A. G. Abanov, Nucl. Phys. B, **846**, 122 (2011)
"Cold Fermi-gas with long range interaction in a harmonic trap"

[VII] F. Franchini and M. Kulkarni, Nucl. Phys. B, **825**, 320 (2010)
"Emptiness and Depletion Formation Probability in spin models with inverse square interaction"

[VIII] M. Kulkarni. F. Franchini and A. G. Abanov, Phys. Rev B **80**, 165105 (2009)
"Nonlinear dynamics of spin and charge in spin-Calogero model"

[IX] M. Kulkarni and R. M. Konik, in preparation
"1/N diagrammatic expansion for coupled parallel quantum dots"

[X] M. Kulkarni, A. G. Abanov, J. Joseph, J. E. Thomas, in preparation
"Smoothed-particle-hydrodynamics for cold atomic systems: Nonlinearity, dissipation and dispersion"

Chapter 1

Introduction and Outlook of the thesis work

In this chapter, we will provide a brief history and introduction to the topics covered in the thesis. We will also present here the questions addressed in this thesis, thereby elaborating the contents of the thesis. This thesis can be broadly divided into two parts. The first part of the thesis studies hydrodynamics or collective field theory of low dimensional interacting systems. The second part of the thesis consists of the study of transport and correlations in low dimensional strongly correlated electron systems. Chapter 2 is based on the publications **[II]** and **[X]**. Chapter 3,4 and 5 are based on publications **[VIII]**, **[VI]** and **[VII]** respectively. Chapter 6 is based on publication **[III]** and chapter 7 is based on publication **[IX]**. For the sake of brevity, the thesis doesnot cover work done in publications **[I]**, **[IV]** and **[V]**.

1.1 Hydrodynamics of low-dimensional interacting systems

Studying strong correlations in low-dimensional systems has been of increasing experimental and theoretical interest. The very nature of low-dimensionality facilitates strong interactions and this has been explored since the 1970's. Understanding the collective behaviour of strongly interacting systems has been of increasing experimental and theoretical importance. Experimental setups

in cold atoms are usually higher dimensional by setup but none-the-less tight harmonic confinement in two of the three dimensions helps us to understand the physics with a dimensionally reduced quasi-1D theory. The construction of these quasi-1D theories is sometimes phenomenological in nature. On the other hand there are certain families of models which are purely one-dimensional models and which facilitate a more formal construction of a field theory. Moreover, these models are integrable, thereby giving rise to very rich integrable field theories.

1.1.1 Hydrodynamics in Cold Atomic systems

There have been several experiments which have realized and studied the collective behaviour of a system of particles both bosonic (for example, [4–7])and fermionic (for example, [8–12]). In this thesis, we study a system of very strongly interacting fermionic atoms. This system (for example observed in the group of John Thomas at Duke) shows an extremely hydrodynamic behaviour. This enables us to probe the physics of nonlinear hydrodynamics of quantum matter. In Chapter 2 we present clear evidence of shock waves in this system of strongly interacting Fermi gas. We study collisions between two strongly interacting atomic Fermi gas clouds. We observe exotic nonlinear hydrodynamic behavior, distinguished by the formation of a very sharp and stable density peak as the clouds collide and subsequent evolution into a box-like shape. We model the nonlinear dynamics of these collisions using quasi-1D hydrodynamic equations. Our simulations of the time-dependent density profiles agree very well with the data and we identify the time evolution of these density fields as shock waves in this universal hydrodynamic system.

We describe how to apply smoothed particle hydrodynamics [13, 14] to cold atomic systems in general and to the experiment conducted at Duke in particular. This technique involves mapping the original hydrodynamic problem to a system of Lagrangian pseudo-particles. Molecular dynamics of these pseudo-particles are studied and one can then, by *mapping-back*, obtain the evolution of the original hydrodynamic density and velocity fields. This approach gives very good agreement between theory and experiment. We will address the interplay between nonlinearity, dissipation and dispersion in cold atomic systems.

The hydrodynamic description employed in understanding these strongly degenerate Fermi gases is not derived starting from a microscopic point of view. This is of course due to the highly complicated nature of the problem, some reasons for example being, nature of interactions, higher dimensionality etc; In addition the hydrodynamic description is not integrable, thereby not facilitating the use of the machinery for integrable models.

1.1.2 Collective Field Theory for Integrable Models

In order to understand the collective behaviour of interacting particles from a more microscopic starting point one can study a certain family of integrable one-dimensional models. This family of integrable models called the Calogero family not only facilitates a more formal way to derive the collective field theory but also gives rise to very rich integrable field theories. We are interested both in deriving a collective field theory starting from the microscopic Hamiltonian and in exploiting the nature of these integrable field theories.

In Chapter 3 the nonlinear dynamics of spin and charge in the spin-Calogero model is studied [15]. This is an integrable one-dimensional model of quantum spin-1/2 particles interacting through an inverse-square interaction and exchange. Classical hydrodynamic equations of motion are written for this model in the regime where gradient terms of the exact hydrodynamic formulation of the theory may be neglected. In this approximation variables separate in terms of dressed Fermi momenta of the model. Hydrodynamic equations reduce to a set of decoupled Riemann-Hopf (a.k.a inviscid Burgers') equations for the dressed Fermi momenta. We study the dynamics of some non-equilibrium spin-charge configurations for times smaller than the time-scale of the gradient catastrophe. We find an interesting interplay between spin and charge degrees of freedom. In the limit of large coupling constant the hydrodynamics reduces to the spin hydrodynamics of the Haldane-Shastry model.

One speciality of the Calogero family is that it remains integrable even in the presence of an external harmonic trap. To the best of our knowledge this is the only example of this kind. This is very convenient as the presence of an external harmonic trap is most often unavoidable in cold atomic experiments. In Chapter 4 we study the spin-Calogero model in the presence of an

external trap. We obtain analytic results for the statics and dynamics of the system. For instance, we find how the equilibrium density profile changes as a function of the interaction strength. The results we obtain for equilibrium configurations are very similar to the ones obtained recently by Ma and Yang [2] for a model of fermions with short ranged interactions. Our main approximation again is the neglect of the terms of higher order in spatial derivatives in equations of motion, ie, gradientless approximation [15]. Within this approximation the hydrodynamic equations of motion can be written as a set of decoupled forced Riemann-Hopf equations for the dressed Fermi momenta of the model. This enables us to write analytical solutions for the dynamics of spin and charge. We describe the time evolution of the charge density when an initial non-equilibrium profile is created by cooling the gas with an additional potential in place and then suddenly removing the potential. We present our results as a simple "single-particle" evolution in the phase-space reminiscent a similar description of the dynamics of non-interacting one-dimensional fermions. Importantly, we find that this model is relatively "short-ranged" and can serve as a toy model for cold atom experiments.

The spinless analog of the spin-Calogero model has been very well studied and its fully nonlinear field theory is known. The integrable field theory of the Calogero model facilitates one to study extremely nontrivial nonlinear hydrodynamic aspects such as shock waves and solitons in Calogero model. Solitons solutions of the Calogero model on a straight line were obtained by Polychronakos [16] and Andric et. al. [17]. However, till recently the meaning and the existence of solitons in presence of an external trap was not clear despite the field theory being integrable even in the trap. In Ref [18] we provide the answer to this question. In this paper [18] we consider here reductions of the classical Calogero model which play a role of "soliton" solutions of the model. We obtain these solutions both for the model with a finite number of particles and in the hydrodynamic limit. In the latter limit the model is described by hydrodynamic equations on continuous density and velocity fields. Soliton solutions in this case are finite dimensional reductions of the hydrodynamic model and describe the propagation of lumps of density and velocity in the nontrivial background.

The availability of the collective field theory also helps in computing certain

correlation functions, such as the Emptiness Formation Probability (EFP) that measures the probability $P(R)$ that a region of length $2R$ is completely void of particles. In Chapter 5 we calculate the EFP in the spin-Calogero Model and Haldane-Shastry Model using their hydrodynamic description. We use an instanton approach and consider the more general problem of an arbitrary depletion of particles (DFP). In the limit of a large size of the depletion region the probability is dominated by a classical configuration in imaginary time that satisfies a set of boundary conditions and the action calculated on such solution gives the EFP/DFP with exponential accuracy. We show that the calculation can be elegantly performed by representing the gradientless hydrodynamics of spin particles as a sum of two spin-less Calogero collective field theories in auxiliary variables. Interestingly, the result we find for the EFP can be cast in a form reminiscent of spin-charge separation, which is suprising. We also highlight the connections between sCM, HSM and $\lambda = 2$ spin-less Calogero model from a EFP/DFP perspective.

In the above mentioned chapters we have, broadly speaking, studied collective field theory or hydrodynamics of interacting particles. In each of these cases we go beyond a quadratic field theory, ie, beyond what is known as a Luttinger liquid or conventional Bosonization. A quadratic field theory would not be able to capture nonlinear effects such as the interaction between spin and charge sectors, steepening of density profiles, shock waves, solitons etc; This aspect of nonlinearity will be elaborated further in the context of each of the mentioned topics in the respective introduction sections of the chapters.

1.2 Transport and Correlations in low dimensional strongly correlated electrons

In the second part of the thesis we turn to transport properties. In particular, we discuss transport and correlations in a low dimensional strongly correlated system of quantum dots. The mesoscopic system of quantum dots forms an ideal platform for using, studying and comparing a variety of low dimensional techniques such as Bethe Ansatz, Diagrammatic Expansions, Mean Field Theories, Numerical Renormalization Group and Quantum Monte Carlo. As will be elaborated in each of the subsequent chapters, the presence of multiple dots

can lead to exotic nonperturbative effects.

1.2.1 RKKY interaction and nature of the ground state of double quantum dots arranged in parallel: Slave Boson Mean Field Theory and the Bethe Ansatz

In chapter 6 we argue, through a combination of slave boson mean field theory and the Bethe ansatz, that the ground state of closely spaced double quantum dots in parallel coupled to a single effective channel is a Fermi liquid. We do so by studying the dots' conductance, impurity entropy, and spin correlation. In particular, we find that the zero temperature conductance is characterized by the Friedel sum rule, a hallmark of Fermi liquid physics, and that the impurity entropy vanishes in the limit of zero temperature, indicating the ground state is a singlet. This conclusion is in opposition to a number of numerical renormalization group studies. We suggest a possible reason for the discrepancy. This chapter describes the role of the effective Ruderman-Kittel-Kasuya-Yosida (RKKY) interaction in parallel quantum dots. An important message of chapter 6 is that RKKY interaction can induce non-ferromagnetic like correlations due to their non-perturbative nature. The recent ability to engineer these multi-dot systems have greatly enhanced the theoretical interest in understanding transport and correlation in multiple quantum dot systems.

1.2.2 1/N diagrams for coupled parallel quantum dots: Transport, Correlations and evidence of Fermi Liquid

Chapter 7 is devoted to another technique called $1/N$ expansion. A large-N diagrammatic approach is used to study coupled quantum dots in a parallel geometry. We show that the Friedel Sum Rule holds perturbativly in 1/N for a parallel double dot system, thereby, strongly suggesting that the ground state is a Fermi liquid. We also extract fully the pole structure of its Green's function matrix and obtain the partition function and dot occupancy via diagrams in a 1/N expansion. Using the FSR, we calculate the conductance from the dot occupancy. We find that the conductance vanishes at the particle-hole

symmetric point. When applicable, we compare our results to a recent Bethe ansatz and a slave boson mean field analysis of the same system. Our main finding from $1/N$ expansion about the ground state being a Fermi Liquid is consistent with both Bethe Ansatz and slave boson mean field theory.

Chapter 2

Shock waves in a strongly interacting Fermi gas

2.1 Introduction

Many interesting Fermi systems such as quark-gluon plasmas[19], neutron stars, and super-conducting electrons exhibit hydrodynamic flow. Phenomena such as high energy collisions, star core collapse, or vortex formation offer the rich and complex dynamics. Solutions of linearized hydrodynamic equations often times cannot provide an adequate description of these exotic systems. In those cases it becomes necessary to solve the full nonlinear hydrodynamic equations to capture the essential physics.

Since the first observation of a strongly interacting degenerate Fermi gas [20], hydrodynamic flow has been observed in studies of collective dynamics [21–23], sound velocity [24], and rotation dynamics [25]. For example, in Ref. [24] a propagation of a small density perturbation over a background has been observed and interpreted as a sound propagation described by linearized hydrodynamic equations. While, the formalism of linearized hydrodynamics gives a good description of experiments where perturbations are small, it does not capture such exotic fingerprints of nonlinear hydrodynamics as shock waves. In this chapter we discuss the first observation of this nonlinear effect and describe it using nonlinear hydrodynamic equations.

We present here an observation of a collision between two clouds of cold strongly interacting Fermi atoms in the unitary regime. This collision can

be understood as essentially nonlinear hydrodynamic behavior of an atomic gas/fluid. The false color absorption images of the atomic clouds at different times during the collision are shown in Fig. 2.1. We would like to focus on two features clearly seen in this data: (i) the formation of a central peak which is well-pronounced and robust (ii) the evolution of this peak into a box-like shape with very sharp boundaries. We notice here that the first feature, though mysterious at the first sight, is present already in solutions of linear wave equations. One should just consider the process not as a collision of atomic clouds but as of a splitting of a central dip in the cloud density into two dips propagating to the left and to the right respectively. The second feature is fundamentally nonlinear and we consider it as a strong evidence of shock wave formation in this system. The sharp boundaries of the "box" are identified then as the shock wave fronts. By reducing the hydrodynamic theory to one dimension and solving the hydrodynamic equations numerically we find an evolution of the density of atoms which is in excellent agreement with the experimental findings.

2.2 Experiment: colliding fermi-clouds

In this section we will briefly describe the experimental setup [1] involved in the collision of Fermi gas clouds at Duke. One of the main goals of this chapter is to interpret the experiment described in this section which was conducted at Duke. The Fermi-gas is comprised of a 50:50 mixture of the two lowest hyperfine states of ^6Li. The gas is confined in a cigar-shaped CO_2 laser trap, and bisected by a blue-detuned beam at 532 nm, which produces a repulsive potential. The gas is then cooled via forced evaporation near a broad Feshbach resonance at 834 G [26]. After evaporation, the trap is adiabatically recompressed to 0.5% of the initial trap depth. This procedure produces two spatially separated atomic clouds, containing a total of $\simeq 10^5$ atoms per spin state. In the absence of the blue-detuned beam, the trapping potential is cylindrically symmetric with a radial trap frequency of $\omega_x = \omega_y = \omega_\perp = 2\pi \times 437$ Hz and an axial trap frequency of $\omega_z = \sqrt{\omega_{Oz}^2 + \omega_{Mz}^2} = 2\pi \times 27.7$ Hz, where the axial frequency of the optical trap is $\omega_{Oz} = 2\pi \times 18.7$ Hz and $\omega_{Mz} = 2\pi \times 20.4$ Hz arises from curvature in the bias magnetic field. When

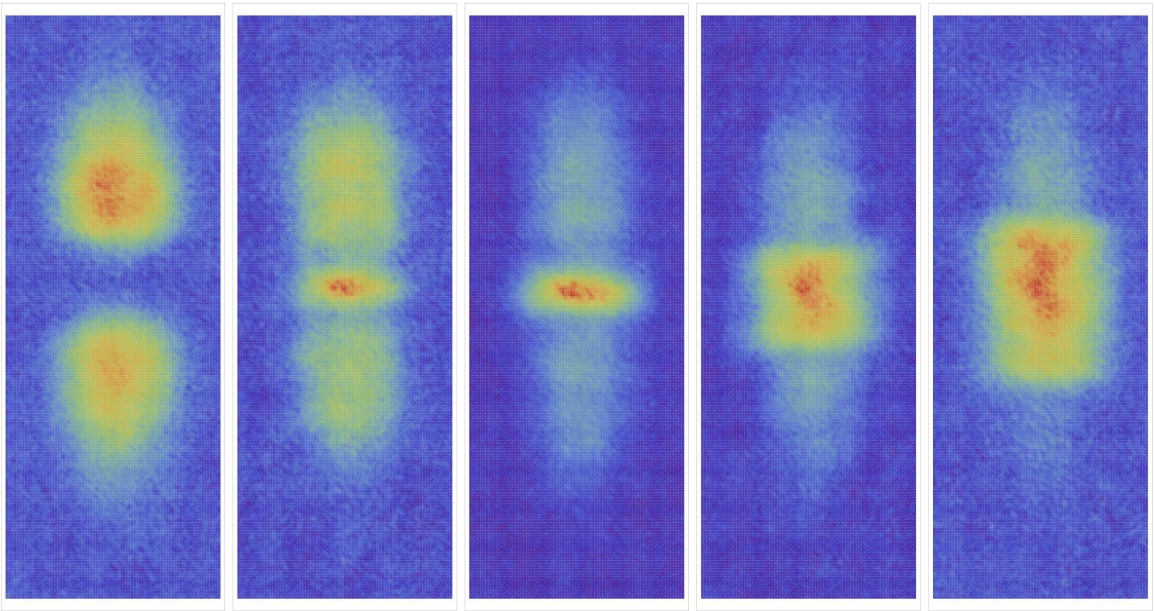

Figure 2.1: False color absorption (in situ) images of the atomic cloud at different time points during the collision[1]. Time evolution is from left to right (0 ms, 2 ms, 4 ms, 6 ms, 8 ms). The atoms are divided into two clouds then accelerate towards each other. As the two clouds collide a sharp rise in density can be seen at the center of the trap. Over time the region of high density evolves from a "peak-like" shape into a "box-like" shape. The central zone in the last two coloumns exhibits first evidence of shock wave formation in a unitary Fermi-gas. The length of the cigar is about 400 μm

the repulsive potential is abruptly turned off, the two clouds accelerate toward each other and collide in the CO_2 laser trap. After a chosen hold time, the CO_2 laser is turned off, allowing the atomic cloud to expand for 1.5 ms, after which it is destructively imaged with a 5 μs pulse of resonant light. The blue-detuned beam produces a repulsive potential which varies only in the z (axial) direction. The form it takes is

$$V_{rep}(z) = V_0 \exp\left(-(z - z_0)^2/\sigma_z^2\right) \tag{2.1}$$

The width was measured by the Duke group to be $\sigma_z = 21.2\mu m$. Using the beam intensity and the ground state static polarizability of ^6Li at 532 nm, we find $V_0 = 12.7\mu K$. This system is a three-dimensional hydrodynamic gas. However, the reasonably tight confinement in the radial direction facilitates the possibility of a dimensional reduction. In the next section we will describe the hydrodynamic theory that helps in understanding the results obtained in the above mentioned experiment.

2.3 Theory: Nonlinear hydrodynamics of quantum matter and dimensional reduction

We assume that the cloud is a strongly interacting Fermi-gas at zero temperature. In addition we model the gas as a single fluid which is consistent with sound velocity measurements [24] (which falls under the paradigm of linear hydrodynamics) and was also shown to work very well for nonlinear hydrodynamics [1]. In this case, the local chemical potential has the universal form $\mu(n_{3D}) = (1 + \beta)\epsilon_F(n_{3D})$, where $\epsilon_F(n_{3D}) = \frac{\hbar^2}{2m}(3\pi^2 n_{3D})^{2/3}$ is the ideal gas local Fermi energy corresponding to the three-dimensional density n_{3D}. Here, $\beta = -0.61$ is a universal scaling factor [20, 27, 28]. Without including the viscous nature of the system we can write the Hamiltonian to be

$$H = 2\pi \int r dr dz m \left[\frac{1}{2} n_{3D} v_{3D}^2 + C n_{3D}^{\frac{5}{3}} + \frac{1}{8} n_{3D} \left(\nabla \log n_{3D}\right)^2\right] \tag{2.2}$$

Here $C = \frac{\hbar^2}{2m}(3\pi^2)^{2/3}(1 + \beta)$ and m is the mass. Eq. 2.2 is a three di-

mensional hydrodynamic theory. Upon assuming an equilibrium profile in the r direction and slow dynamics in the z direction we can do a dimensional reduction to obtain a quasi-1D field theory. The assumptions can be casted as

$$n_{3D}(z,r,t) = F\left[n_{1D}(z,t), r\right] \tag{2.3}$$

$$v_{3D} = v_{1D}(z,t)\hat{z} \tag{2.4}$$

where F is a function that relates the quasi-1D density to the 3D density. A Thomas-Fermi approximation in 3D gives us

$$n_{3D}(z,r) = \bar{n}\left(1 - \frac{r^2}{R_\perp^2} - \frac{z^2}{R_z^2}\right)^{\frac{3}{2}} \tag{2.5}$$

where $\tilde{n} = [(2m\mu_G/\hbar^2)/(1+\beta)]^{3/2}/(3\pi^2)$. In Eq. 2.5, $R_{z,\perp} = \sqrt{2\mu_G/(m\omega_{z,\perp}^2)}$ and μ_G is the global chemical potential, which is determined by normalizing the integral of the 3D density to the total number N of atoms in both spin states. For $N = 2\times10^5$, we find $\mu_G = 0.53\,\mu$K, $R_z = 220\,\mu$m, and $R_\perp = 14\,\mu$m. Integrating Eq. 2.5 in radial direction straightforwardly gives us the effective 1D density

$$n_{1D}(z) = \frac{2\pi}{5}R_\perp^2\bar{n}\left(1 - \frac{z^2}{R_z^2}\right)^{\frac{5}{2}}. \tag{2.6}$$

From Eq. 2.5 and Eq. 2.6 it is easy to find the function F that relates the quasi-1D density to the 3D density. We find

$$n_{3D}(r,z) = \bar{n}\left[\left(\frac{n_{1D}(z)}{\frac{2\pi}{5}R_\perp^2\bar{n}}\right)^{\frac{2}{5}} - \frac{r^2}{R_\perp^2}\right]^{\frac{3}{2}} \tag{2.7}$$

The action is

$$\begin{aligned} S &= \int L dt \\ &= 2\pi\int r dt dr dz\, m\Bigg\{\phi_{3D}\frac{\partial n_{3D}}{\partial t} - \frac{1}{2}n_{3D}(\nabla\phi_{3D})^2 - Cn_{3D}^{\frac{5}{3}} - \frac{1}{8}n_{3D}\left(\nabla\log n_{3D}\right)^2 \\ &\quad -\frac{1}{2}n_{3D}(\omega_z^2 z^2 + \omega_r^2 r^2)\Bigg\} \end{aligned} \tag{2.8}$$

Using the variational method [29] one can arrive at the continuity equation and the Euler equation. It turns out that the hydrodynamic velocity is given by $v = \nabla\phi$. We will first do a dimensional reduction of Eq (2.8)

Plugging in Eq. 2.7 and Eq. 2.4 into the 3D action (Eq. 2.8) we get the following quasi-1D action,

$$\begin{aligned} S &= \int Ldt \\ &= m\int dtdz\Bigg\{\phi\frac{\partial n}{\partial t} - n\big[\frac{(\nabla\phi)^2}{2} + An^{\frac{2}{5}} + \\ &\quad Bn^{-\frac{2}{5}} + \frac{1}{2}\omega_z^2 z^2 + \frac{9\hbar^2}{40m^2}n\left(\partial_z \log n\right)^2\big]\Bigg\} \end{aligned} \tag{2.9}$$

where $A = \frac{5}{14}\omega_\perp^2 l_\perp^2 \left(\frac{15\pi}{2}l_\perp\right)^{2/5}(1+\beta)^{3/5}$ and $l_\perp = \sqrt{\frac{\hbar}{m\omega_\perp}}$ is the oscillator length. It turns out that $B = \frac{\hbar^2}{m^2}\frac{1.06}{(1+\beta)^{\frac{3}{5}}}l_\perp^{-\frac{12}{5}}$. Note that in Eq. 2.9 we have dropped the subscript "1D" for the sake of brevity (the subscript "z" in ω will be dropped henceforth). In Eq. 2.9 the term proportional to B is much smaller than the term proportional to A and therefore we can neglect it.

The Hamiltonian corresponding to the above dimensionally reduced action (Eq. 2.9) is

$$\begin{aligned} H[n,v] &= m\int dzn\big[\frac{v^2}{2} + An^{\frac{2}{5}} + \\ &\quad \frac{1}{2}\omega_z^2 z^2 + \frac{9\hbar^2}{40m^2}n\left(\partial_z \log n\right)^2\big]. \end{aligned} \tag{2.10}$$

The continuity and Euler equation[1] can be obtained by taking the variation [29] of the above action with respect to ϕ ($\frac{\delta S}{\delta\phi}$) and n ($\frac{\delta S}{\delta n}$) respectively. They read as

[1]The last term in Eq. 2.12 doesnot come via variational principle and is added phenomenologically.

$$\partial_t n = -\partial_z (nv) \tag{2.11}$$

$$\partial_t v = -\partial_z \left\{ \frac{v^2}{2} + \frac{7A}{5} n^{\frac{2}{5}} + \frac{1}{2}\omega^2 z^2 + \frac{9\hbar^2}{20m^2} \frac{\partial_z^2 \sqrt{n}}{\sqrt{n}} \right\} + \nu \frac{\partial_z (n \partial_z v)}{n} \tag{2.12}$$

It is easy to check that Eq. (2.10) along with the Poisson relation $\{mn(x), v(y)\} = \delta'(x-y)$ also gives the above quasi-1D continuity (Eq. 2.11) and quasi-1D Euler equation (Eq. 2.12).

In Eq. 2.12 we have added a "viscosity" term *phenomenologically* to describe dissipative effects. For the unitary 1D fluid, ν is the effective kinematic viscosity, which has a natural scale $\hbar/m$. It is the only fitting parameter in the theory [2].

Below, we will provide a derivation of the *phenomenologically* added viscosity term as arising from a shear viscosity[31, 32] in 3D. The Euler equation can be generally written as

$$\frac{\partial}{\partial t}(n_{3D} v_i) = -\frac{\partial \Pi_{ik}}{\partial x_k} \tag{2.13}$$

where $\Pi_{ik} = p\delta_{ik} + n_{3D} v_i v_k - \sigma'_{ik}$, with p being the pressure term. For an isotropic fluid, σ'_{ik} takes the form

$$\sigma'_{ik} = \eta \left(\frac{\partial v_i}{\partial x_k} + \frac{\partial v_k}{\partial x_i} - \frac{2}{3}\delta_{ik} \frac{\partial v_l}{\partial x_l} \right) + \zeta \delta_{ik} \frac{\partial v_l}{\partial x_l} \tag{2.14}$$

where η is the coefficient of shear viscosity and ζ is the coefficient of bulk viscosity (which is zero for a Unitary Fermi gas). Now, if we plug in Eq. 2.7 and Eq. 2.4 into Eq. 2.14 then we obtain

$$\sigma'_{zz} = \frac{4\nu}{3} \frac{\partial v_{1D}}{\partial z} \tag{2.15}$$

[2] In a unitary Fermi gas, which is scale invariant, the bulk viscosity vanishes. We expect that ν arises from shear viscosity, which has a natural scale $\eta \propto \hbar n$, so that $\nu = \eta/(nm) \propto \hbar/m$. See Ref. [30].

and it is easy to check that $\sigma'_{zr} = 0$. The equation of motion for a viscous fluid is obtained by adding the term $\frac{\partial \sigma'_{zz}}{\partial z}$ to the right hand side of the Euler equation. We define here the kinematic viscosity as given by $\nu = \frac{\eta}{n_{3D}}$. Plugging this into Eq. 2.15 gives the following term in the Euler equation (we are writing below only the viscous term).

$$\frac{\partial}{\partial t}(\int d^2r\, n_{3D} v_{1D}) = \frac{4\nu}{3}\frac{\partial}{\partial z}\left[\int d^2r\, n_{3D}\frac{\partial v_{1D}}{\partial z}\right] \tag{2.16}$$

Integrating both sides of Eq. 2.16 precisely results in the previously *phenomenologically* added viscosity term, ie, $\nu\frac{\partial_z(n\partial_z v)}{n}$. We have thus shown here that the 1D dimensionally reduced bulk viscosity term arises from a 3D shear viscosity.

The last term in the curly brackets in Eq. 2.12 come from the dimensional reduction of the Quantum Pressure term. There are several mechanisms at work in Eq. 2.12. There is essentially a nonlinear term (ie, a term without derivatives and just powers of n), one dissipative term (viscosity) and one term which can induce oscillations (dispersive terms). We therefore see that this system of strongly interacting fermions can be an ideal setup to study the interplay and role of all these three mechanisms (nonlinearity, dissipation and dispersion). However, we will show in the experiment described above that the role of the dispersive term is negligible and viscosity (dissipative) plays a dominant role. Nonlinear terms which appear in the Euler equation as powers of n result in creating steep gradients and these are counter-balanced by dissipative or dispersive terms. When steep gradients start getting counter-balanced then we can call it an "onset" of shock waves (dissipative or dispersive shock depending on which term plays a role). One could introduce artificial tuning numerical coefficients in front of the dissipative and dispersive terms and modulate their effect.

Eq. 2.11 and Eq. 2.12 are fully nonlinear coupled partial differential equations and do not admit exact solutions. However, in certain limits, for instance the sound wave experiments with a small pulse V_0, one can linearize the differential equations (2.11) and (2.12) around an equilibrium density configuration $n_0(z)$ in a harmonic trap. Defining $n(z,t) \equiv n_0(z) + \delta n(z,t)$, the linearized

evolution equation for $\delta n(z,t)$ (neglecting viscosity) is

$$\partial_t^2 \delta n = \partial_z \left[n_0 \partial_z \left(\frac{14A}{25m} n_0^{-\frac{3}{5}} \delta n \right) \right]. \tag{2.17}$$

For a flat background density, i.e., constant n_0, with $\mu_G = \frac{7A}{5} n_0^{2/5}$, Eq. 2.17 reduces to $\partial_t^2 \delta n = c^2 \partial_z^2 \delta n$ with the sound velocity $c = \sqrt{2\mu_G/5m}$, in agreement with previous theory [33, 34] and experiment [24].

Our aim is to study the fully nonlinear hydrodynamics of the system with initial conditions from the experiment described in Sec 2.2. We do so in two different ways. First, we employ the method of a discretized grid and later we will use another method known as smoothed-particle hydrodynamics. The second method involves mapping the quasi-1D Hamiltonian (Eq. 2.10) and the Continuity (2.11) and Euler equations (2.12) to a system of Lagrangian pseudo-particles [13, 14].

2.4 Model and the grid method

We establish initial conditions of our model to match the experiment as closely as possible. The one-dimensional integrated density equation which includes the effect of the repulsive potential is given in Eq. (2.6). In our simulation we use the measured experimental parameters for $\omega_\perp$ and ω_z. We measure the width $\sigma_z = 21.2\,\mu$m. The offset $z_0 = 5\,\mu$m of the focus from the center in the long direction of the optical trap is determined by a fit to the first density profile at 0 ms. Using the beam intensity and the ground state static polarizability of ^{6}Li at 532 nm, we find $V_0 = 12.7\,\mu$K.

We use the average measured total number of atoms $N = 2.1 \times 10^5$ to determine the global chemical potential, μ_G. The black curve in the left top-most panel of Fig. 2.2 represents the initial density of the trapped atoms after expansion obtained using the above parameters.

For numerical simulation we create and load a density array as well as a velocity array with grid spacing δ_z. The initial velocity is set to zero. The simulation then updates the density and velocity field in discrete time steps δ_t according to Eq. (2.11) and Eq. (2.12). The simulation provides a near perfect representation of the observed density evolution (see Fig. 2.2). For the

simulation curves shown in the figure we use a grid of 50 points relating to a $\delta_z = 4.2\mu m$ and a $\delta_t = 17.7\mu s$, which minimizes the χ^2. A χ^2 fit to the data is constant for smaller δ_z as long as the time step was set according to the relation $\delta_t = \delta_z^2 \times 10^6$ for grids of 100 and 200 points. Therefore the simulation converges for small δ_t. To check for numerical consistency we also used an alternate approach of *smoothed-particle-hydrodynamics*[13] (see Sec 2.5) where a fluid is described by discrete pseudo particles and the results obtained indeed coincide with the previously mentioned *discretized grid* approach. As shown in Fig. 2.2 we observe a dramatic evolution of the density of the gas. During the collision, a distinct and stable density peak forms at the point of collision in the center of the trap. At its apex, the peak density is nearly twice that of the equilibrium integrated central density. This central peak appears early on in the collision and grows in intensity. At a certain point the 2D images show that the peak evolves into a box shape. In 1D this is seen as a flattop line shape which expands in size as more atoms are present in the collision zone. As the time evolution of the gas progresses the maximum density gradient increases.

Upon careful inspection of the data we can find only small deviations from the simulation. At the 4 ms time point the maximum density of the observed central peak exceeds that of the simulation. This apart the simulation provides a very good description of the evolution of the 1D density. Changing the phenomenological parameter ν in Eq. 2.12 in simulations allows us to conclude that numerics are compatible with the experiment in the range of effective bulk viscosities $\nu \sim 1 - 10\ \hbar/m$.

2.5 Smoothed particle formulation of nonlinear hydrodynamics

In this section we describe the mapping of the quasi-1D Hamiltonian (Eq. 2.10), the Continuity (2.11) and Euler equations (2.12) to a system of Lagrangian pseudo-particles [13, 14]. The pseudo-Hamiltonian in the continuum limit reproduces all the hydrodynamic terms in the field theory. It turns out that Eq. 2.10 can be mapped to a system of N_p pseudo-particles obeying the following microscopic Hamiltonian,

$$
\begin{aligned}
H &= m\sum_{j=1}^{N}\frac{v_j^2+\omega^2 x_j^2}{2}+ \\
&\quad m\sum_{j=1}^{N_p} U_{NL}[x_{j+1},x_j]+U_{QP}[x_{j+2},x_{j+1},x_j] \qquad (2.18)
\end{aligned}
$$

Here U_{NL} and U_{QP} are pseudo-particle mapping [3] of the nonlinear (pressure) term and the Quantum Pressure (dispersive) term respectively. They are given by

$$
\begin{aligned}
U_{NL}[x_{j+1},x_j] &= \frac{A}{[N_p(x_{j+1}-x_j)]^{\frac{2}{5}}} \\
&+ \frac{B}{[N_p(x_{j+1}-x_j)]^{-\frac{2}{5}}} \qquad (2.19)
\end{aligned}
$$

$$
U_{QP}[x_{j+2},x_{j+1},x_j]=\frac{1}{8}\left(\frac{1}{x_{j+2}-x_{j+1}}-\frac{1}{x_{j+1}-x_j}\right)^2 \qquad (2.20)
$$

Now, one can use the Hamilton equations,

$$
\dot{x}_j = \frac{\partial H}{m\partial v_j} \qquad (2.21)
$$

$$
\dot{v}_j = -\frac{\partial H}{m\partial x_j} \qquad (2.22)
$$

to get the following Newtonian equations.

$$
\dot{x}_j = v_j \qquad (2.23)
$$

[3] This prescription of course is not unique. However, in the limit of large pseudo-particles they are supposed to reproduce the original field theory upon taking the continuum limit.

$$
\begin{aligned}
\dot{v}_j &= -\frac{\partial}{\partial x_j} U[x_j] \\
- \quad & \frac{\partial}{\partial x_j} \left(\sum_j \left[U_{NL}[x_{j+1}, x_j] + U_{QP}[x_{j+2}, x_{j+1}, x_j] \right] \right) \\
+ \quad & \eta \left[\frac{v_{j+1} - v_j}{(x_{j+1} - x_j)^2} - \frac{v_j - v_{j-1}}{(x_j - x_{j-1})^2} \right]
\end{aligned} \tag{2.24}
$$

In Eq. 2.24, the term $U[x_j]$ is any external potential. In our case this is an external Harmonic trap given by

$$
U[x_j] = \frac{1}{2}\omega^2 x_j^2 \tag{2.25}
$$

The last term in Eq. 2.24 is the pseudo-particle representation of the viscosity term. One can observe that in the pseudo-particle language the terms that counter-balance steep gradients (dispersive or dissipative) necessarily involve more that one nearest neighbor. A continuum limit of the pseudo-Hamiltonian (Eq. 2.18) gives back the quasi-1D collective field theory (Eq. 2.10) with some additional terms which are of order $\mathrm{O}(\frac{1}{N_p})$ or higher. Therefore for large enough N_p one could get back all the hydrodynamic properties of the real system (Eq. 2.10) by solving the "molecular dynamics" of N_p pseudo-particles(Eq. 2.23 and Eq.2.24).

2.6 Results from smoothed particle hydrodynamics

In this section, we study the nonlinear hydrodynamics via the method described in previous section. The experiment involved cooling the system in the presence of an additional blue-detuned laser beam which provides an external potential (Eq.2.1) in addition to the Harmonic trap. The quasi-1D density in this case will read

$$
n_{1D}(z) = \frac{2\pi}{5} R_\perp^2 \tilde{n} \left(1 - \frac{z^2}{R_z^2} - \frac{V_{rep}(z)}{\mu_G} \right)^{\frac{5}{2}}. \tag{2.26}
$$

We put the pseudo-particles in initial positions such that they mimic the above density. As the system is cooled the initial velocities of the pseudo particles are zero[4].

The blue-detuned laser is then switched off which means we solve the molecular dynamics of the particles whose initial positions imitate Eq. 2.26 and which evolve according to Eq. 2.23 and Eq.2.24[5].

For the experimental conditions and initial profiles described in this chapter we find that there is an interplay between nonlinearity and dissipation, thereby the phenomenon of dissipative shock waves. For these conditions we donot see any significant role of the quantum pressure (dispersive) term, however it always exists.

We find near perfect agreement between the experiment and the method of smoothed particle hydrodynamics. There is a dramatic evolution for the density of the gas. During the collision we see a distinct and stable density peak at the point of collision in the center of the trap. The absorption images shown in Fig. 2.1 already suggest shock wave formation. Further analysis of the simulation curves provides additional evidence for shock waves. Without any dissipation, the numerical integration of the quasi-1D theory breaks down due to a "gradient catastrophe." A gradient catastrophe is a situation where hydrodynamic profiles develop infinite gradients. We find that the dissipative force in Eq. 2.12, which is described by the kinematic viscosity coefficient ν, is required to attenuate the large density gradients and avoid gradient catastrophe. We find that the best fits are obtained with the viscosity parameter $\nu = 10\,\hbar/m$. This range is the same as described in the discretized grid method. For smaller values of ν, the simulation produces qualitatively similar

[4]We could also put the pseudo particles at arbitrary places and solve the continuity and Euler equations, with an additional damping term such as $-\gamma v$ in the Euler equation. This will result in equilibrating the particles (See Fig. 2.3) and will produce the initial density profile (Eq. 2.26).

[5]To compare the numerical solutions of Eq. 2.23 and Eq.2.24 with experiment, we note that the images are taken after an additional free expansion for 1.5 ms, during which n_{1D} continues to slowly evolve in the axial potential of the bias magnetic field, i.e., $\omega_z \to \omega_{Mz} = 2\pi \times 20.4$ Hz. We assume that during this expansion, the transverse density profiles keep the same form, but the radius increases with time. Then $n_{3D}(r,z) \to n_{3D}(r/b_\perp, z)/b_\perp^2$, where $b_\perp(t)$ is a transverse scale factor, which obeys $\ddot{b}_\perp = \omega_\perp^2\, b_\perp^{-7/3}$, with $b_\perp(0) = 1$ and $\dot{b}_\perp(0) = 0$ [20, 35, 36]. Since the 3D pressure scales as $n_{3D}^{5/3}$, the 1D pressure scales as $b_\perp^{-4/3}$. This leads to a simple modification of Eq. 2.12: $A \to A(t) = A/b_\perp^{4/3}(t)$.

results to those shown in the figure, only with steeper density gradients at the edges of the collision zone. The dissipative term $\propto \nu$ has a relatively small effect on the density profiles, unless we are in a shock wave regime, where the density gradients are large. Hence, the numerical model suggests that the large density gradient observed at the edge of the collision zone is the leading edge of a dissipative shock wave. A world-line diagram depicting trajectory of pseudo-particles is shown in Fig 2.4. Although, this trajectory does not bear any direct meaning as far as the original physical system of a Unitary Fermi gas is concerned, it is none-the-less very useful in deriving certain conclusions. For instance, the *"straight-line like visual image"* suggests that the shock waves reasonably maintains a constant speed throughout. In a similar way one could also see different visual patters for different values of dynamic viscosity.

2.7 Conclusion

We observed that the collision of two ultra-cold clouds of Fermi atoms in the unitary regime was accompanied by the formation of shock waves. We considered nonlinear hydrodynamic equations of a superfluid reduced to a quasi-1D hydrodynamics. We showed that numerical solutions of these hydrodynamic equations (2.11,2.12) are in a very good agreement with the experimental data. Shock waves are a hallmark of nonlinear physics and it is remarkable that the oversimplified hydrodynamic approach works so well under the considered experimental conditions. This happens, probably, because the interactions in a unitary Fermi gas are very strong and a special feature of a unitary gas, i.e., the dynamic properties are strongly constrained by an underlying scale invariance. We introduced an effective bulk viscosity of one-dimensional hydrodynamics as a phenomenological fitting parameter. It is essentially the only fitting parameter in hydrodynamics and the values of $\nu \sim 1 - 10\ \hbar/m$ seem to be consistent with the experimental data. This is the right order of magnitude of the effective viscosity dictated by dimensional considerations. We showed how the effective bulk viscosity in 1D arises from a shear viscosity in 3D.

Studies of nonlinear hydrodynamics can now be done over a wide range of temperatures, in both the superfluid and normal fluid regimes and the

magnetic field control of the interaction strength enables continuous tuning from a dispersive BEC to a dissipative Fermi-gas. We showed that in this experiment on a Unitary Fermi gas, dispersive terms do not cause any effect such as those observed in BEC's [7, 37].

The method of smoothed particle hydrodynamics has several benefits over traditional grid-based techniques. SPH (also known as meshless algorithm or adjustable grid algorithm) guarantees conservation of mass without extra computation since the particles themselves represent mass. The method of SPH results in mapping coupled nonlinear partial differential equations for hydrodynamic fields into a set of ordinary differential equations (Newton's Equations) for pseudo-particles. These resulting Newton's equations are easier to handle. Dealing with pseudo-particles rather than fields help us in avoiding to worry about issues such as boundary conditions and possible infinities resulting from regions where there are vanishing fields. Once the pseudo-particles are placed to mimic the hydrodynamic field we can just solve the Newton's equations for particles. One drawback over grid-based techniques is the need for large numbers of particles to produce simulations of equivalent resolution. However, our results from SPH show near perfect agreement already with 500 pseuso-particles which is easy to handle as far as solving Newton's equations are concerned.

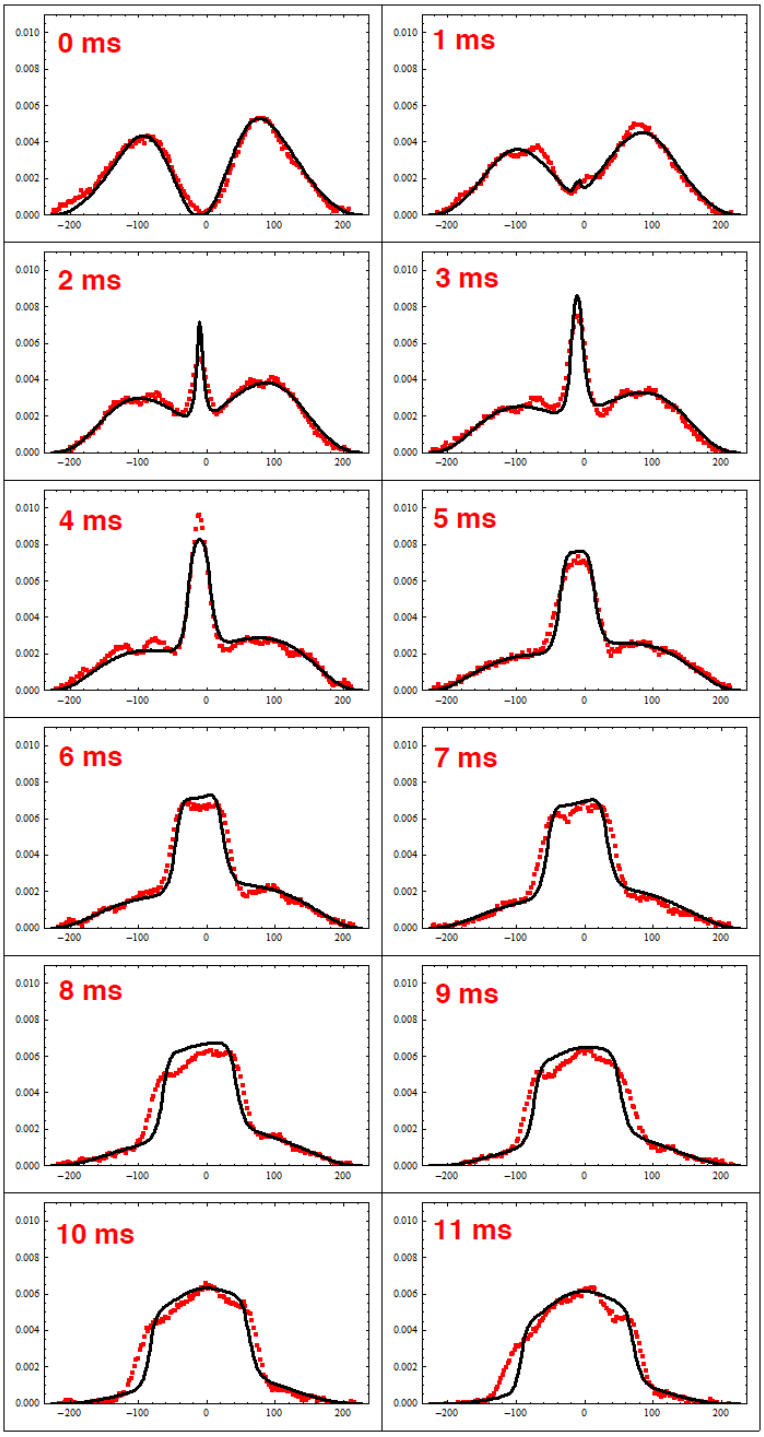

Figure 2.2: 1D density profiles divided by the total number of atoms versus time for two colliding unitary Fermi gas clouds. The normalized density is in units of $10^{-2}/\mu$m per particle. Red dots show the measured 1D density profiles. Black curves show the simulation, which uses the measured trap parameters and the number of atoms, with the kinetic viscosity as the only fitting parameter.

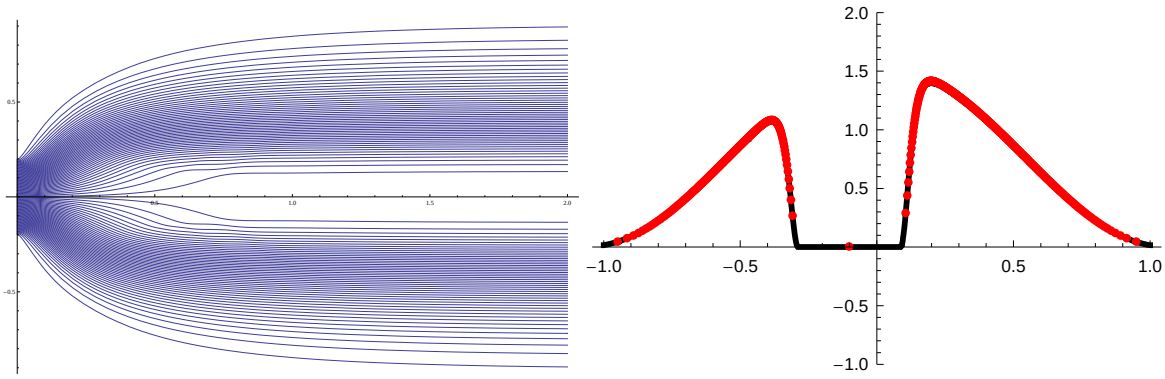

Figure 2.3: (Left) The process of equilibration by molecular dynamics of pseudo-particles in presence of a "knife". The x-axis is time and the y-axis are the positions of pseudo-particles. (Right) Red denotes the density obtained from the position of the pseudo-particles and black denotes the analytical formula.

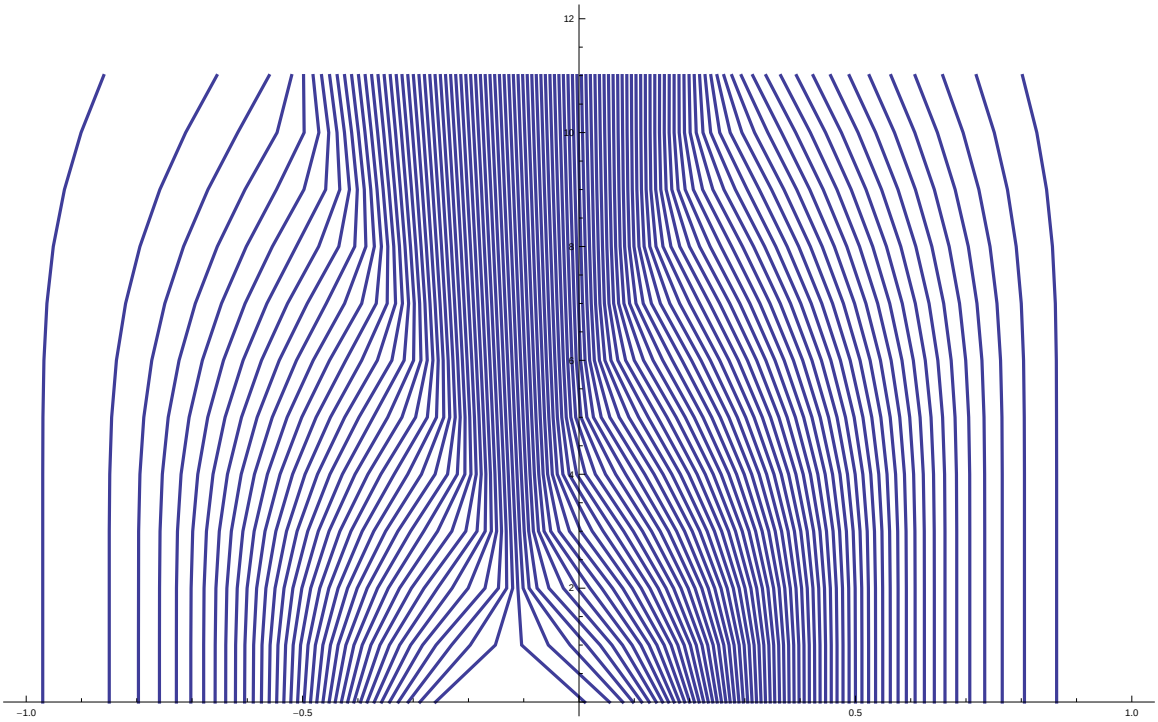

Figure 2.4: World-line diagram depicting trajectory of pseudo-particles after removing the knife.

Chapter 3

Nonlinear dynamics of spin and charge in the spin-Calogero model

3.1 Introduction

One-dimensional models of many body systems have been a subject of intensive research since the seventies. Due to the low dimensionality, standard perturbative approaches developed in many body theory are often inapplicable. On the other hand some techniques specific to one spacial dimension are available and allow to treat systems of interacting particles non-perturbatively. The Fermi Liquid paradigm is replaced by the Luttinger Liquid theory [38] in one dimension. One of its most striking predictions is that at low energies spin and charge degrees of freedom decouple. One can say that at low energies physical electrons exist as separate spin and charge excitations. At higher energies it is expected that spin and charge recombine into the original electrons. One can see the traces of spin-charge interaction taking into account corrections to the Luttinger liquid model arising from the finite curvature of band dispersion at Fermi energy [38]. The coupling between spin and charge in one-dimensional systems was studied both perturbatively and using integrable models available in one dimension [39].

In this chapter we study the interaction between spin and charge in another integrable model – the spin-Calogero model (sCM). This model is a spin generalization [40–42] of the well-known Calogero-Sutherland model [43].

Calogero-Sutherland type models occupy a special place in 1D quantum

physics. They are exactly solvable (integrable) but are very special even in the family of integrable models. In particular, they can be interpreted as systems of "non-interacting" particles with fractional exclusion statistics [43–48].

The sCM model is given by the following Hamiltonian:

$$H \equiv -\frac{\hbar^2}{2}\sum_{j=1}^{N}\frac{\partial^2}{\partial x_j^2} + \frac{\hbar^2}{2}\sum_{j\neq l}\frac{\lambda(\lambda \pm \mathbf{P}_{jl})}{(x_j - x_l)^2} \tag{3.1}$$

where we took the mass of particles as a unity and $\mathbf{P}_{jl}$ is the operator that exchanges the positions of particles j and l [40]. The $\pm$ sign in the exchange term corresponds to the ferromagnetic and anti-ferromagnetic ground state respectively if we are studying fermions. Similarly, it corresponds to the anti-ferromagnetic and ferromagnetic ground state respectively if we are considering bosonic particles. The four cases can be summarized as:

$$\text{Bosons} \longrightarrow \begin{cases} + & \Rightarrow & \text{Anti-ferromagnetic} , \\ - & \Rightarrow & \text{Ferromagnetic} , \end{cases}$$

$$\text{Fermions} \longrightarrow \begin{cases} + & \Rightarrow & \text{Ferromagnetic} , \\ - & \Rightarrow & \text{Anti-ferromagnetic} . \end{cases}$$

The coupling parameter λ is positive and N is the total number of particles.

As it has been already noted above the sCM is a very special model. In particular, in contrast to more generic integrable or non-integrable models the spin and charge in sCM are not truly separated even at low energies [41]. Of course, one can still describe the low-energy excitation spectrum of the sCM by two independent harmonic fluid Hamiltonians, one for the charge and the other for spin. However, it turns out that for the sCM the spin and charge velocities are the same [41], i.e. spin and charge do not actually separate.

Here we study the spin-Calogero model in the limit of an infinite number of particles using the hydrodynamic approach. Even though the collective field theory/quantum hydrodynamics of the spinless Calogero-Sutherland model has been studied in great detail [16, 49–53], a complete understanding of its spin generalization is still lacking although a considerable progress has been done recently in Refs. [54, 55].

We study the nonlinear collective dynamics of the sCM in the semiclassical

approximation, additionally neglecting gradient corrections to the equations of motion. This limit is justified as long as we consider configurations with small gradients of density and velocity fields. The gradientless approximation is commonly employed in studying nonlinear equations [56] and allows to study the evolution for a finite time while the first nonlinear contributions are dominant. For longer times, the solution will inevitably evolve toward configurations with large field gradients (such as shock waves) and the gradientless approximation becomes inapplicable. Nevertheless, in the initial stage of the evolution, corrections due to gradient terms in the equations of motion can be neglected (see further discussion in the Sec. 3.5.2). We derive the gradientless hydrodynamics Hamiltonian from the Bethe Ansatz solution of the model.

The chapter is organized as follows. In Sec. 3.2 we start with the simplest spinful integrable model – a system of free fermions with spin. We briefly review the Bethe Ansatz solution for spin-Calogero model in Sec. 3.3 and deduce the hydrodynamic Hamiltonian for the sCM from this solution in Sec. 3.4 neglecting gradient corrections. The corresponding classical equations of motion are given in Sec. 3.5. It is shown that variables separate and the system of hydrodynamic equations is decoupled into four independent Riemann-Hopf equations for a given special linear combinations of density and velocity fields – the dressed Fermi momenta. In Sec. 3.6 we illustrate that in the limit of strong coupling the hydrodynamics of sCM is reduced to the hydrodynamics of the Haldane-Shastry lattice spin model giving the hydrodynamic formulation of the so-called *freezing trick* [57]. We present some particular solutions of the hydrodynamic equations demonstrating nonlinear coupling between spin and charge degrees of freedom in the sCM in Sec. 3.7 and conclude in Sec. 3.8. To avoid interruptions in the main part of the chapter some important technical details are moved to the appendices and are organized as follows. In Appendix A we use an asymptotic Bethe ansatz to derive the hydrodynamics of the sCM and to explain why variables separate in this system. In Appendix B we describe the notion of true hydrodynamic velocities. In Appendix C we relate the hydrodynamics of sCM to two infinite families of mutually commuting conserved quantities and collect our results for the hydrodynamics in the different regimes of sCM. Finally, in Appendix D we derive a hydrodynamic description of the Haldane-Shastry model from its Bethe Ansatz solution.

3.2 Free fermions with spin

For one-dimensional free fermions without internal degrees of freedom the lowest state with a given total number of particles and total momentum corresponds to all single-particle plane wave states filled if the corresponding momentum k satisfies $k_L < k < k_R$. Here $k_{L,R}$ are left and right Fermi momenta respectively which are defined by the given number of particles and momentum of the system:

$$N/L = \int_{k_L}^{k_R} \frac{\mathrm{d}k}{2\pi} = \frac{k_R - k_L}{2\pi} = \rho \,, \tag{3.2}$$

$$P/L = \int_{k_L}^{k_R} \frac{\mathrm{d}k}{2\pi}\, \hbar k = \hbar \frac{k_R^2 - k_L^2}{4\pi} = \rho v \,. \tag{3.3}$$

Here we introduced the (overall) velocity of the system v which is given from (3.2,3.3) by

$$v/\hbar = \frac{k_R + k_L}{2} \,. \tag{3.4}$$

Inverting (3.2,3.4) we express the left and right Fermi points $k_{L,R}$ in terms of the density ρ and velocity v as

$$k_{R,L} = v/\hbar \pm \pi\rho. \tag{3.5}$$

The energy of this state is given by

$$E/L = \int_{k_L}^{k_R} \frac{\mathrm{d}k}{2\pi}\, \frac{\hbar^2 k^2}{2} = \hbar^2 \frac{k_R^3 - k_L^3}{12\pi} = \frac{\rho v^2}{2} + \frac{\hbar^2\pi^2}{6}\rho^3. \tag{3.6}$$

Up to this moment $\rho, v, k_{R,L}$ are just numbers characterizing the chosen state of free fermions (only two of them are independent). Assuming the locality of the theory we promote these numbers to quantum fields and write the hydrodynamic Hamiltonian of free spinless fermions as

$$\mathcal{H} = \int \mathrm{d}x\, \left[\frac{\rho(x)v^2(x)}{2} + \frac{\hbar^2\pi^2}{6}\rho^3(x)\right] = \int \mathrm{d}x\, \hbar^2 \frac{[k_R(x)]^3 - [k_L(x)]^3}{12\pi}. \tag{3.7}$$

Here we consider $\rho(x)$ and $v(x)$ as quantum field operators of density and velocity (and $k_{R,L}$ as given by (3.5)) having canonical commutation relations

[32]

$$[\rho(x), v(y)] = -\mathrm{i}\hbar\delta'(x-y)\ . \tag{3.8}$$

Of course, gradient corrections to (3.7) are generically present and the above "derivation" is just a heuristic argument (semiclassical in nature). It turns out that (3.7) is, in fact, exact for free fermions.[1] It can be derived rigorously either using the method of collective field theory [58–60] or the conventional bosonization technique (but without linearization at Fermi points)[38, 61, 62].

The two terms of (3.7) have a very clear physical interpretation. The first term is the kinetic energy of a fluid moving as a whole – the only velocity term allowed by Galilean invariance. The second one is the kinetic energy of the internal motion of particles. This term is finite due to the Pauli exclusion principle. Within the hydrodynamic approach we have to think of this term as of an internal energy of the fluid.

Commuting the Hamiltonian (3.7) with the density and velocity operators one obtains the continuity and the Euler equations of quantum hydrodynamics. Alternatively, using $[k_L(x), k_L(y)] = -[k_R(x), k_R(y)] = 2\pi i\delta'(x-y)$ the equations of motion can also be written as a system of quantum Riemann-Hopf equations

$$\dot{k}_{R,L} + \hbar\, k_{R,L}\, \partial_x k_{R,L} = 0\ . \tag{3.9}$$

For free fermions with spin, we simply add the Hamiltonians (3.7) written for spin up and spin down fermions:

$$H = \int \mathrm{d}x \left\{ \frac{1}{2}\rho_\uparrow v_\uparrow^2 + \frac{1}{2}\rho_\downarrow v_\downarrow^2 + \frac{\pi^2\hbar^2}{6}\left(\rho_\uparrow^3 + \rho_\downarrow^3\right) \right\}\ . \tag{3.10}$$

Expanding (3.10) around the background density $\rho_0 = \frac{k_F}{\pi}$ and the background velocity $v_0 = 0$ up to quadratic terms in v_α and $\delta\rho_\alpha = \rho_\alpha - \rho_0$, we obtain the harmonic fluid approximation

$$\begin{aligned} H &\approx \frac{\rho_0}{2}\int \mathrm{d}x \left(v_\uparrow^2 + \pi^2\hbar^2\delta\rho_\uparrow^2 + v_\downarrow^2 + \pi^2\hbar^2\delta\rho_\downarrow^2\right) \\ &\approx \frac{\rho_0}{4}\hbar^2 \sum_{\alpha=\uparrow,\downarrow}\int \mathrm{d}x\ \left[(\partial_x\phi_{R,\alpha})^2 + (\partial_x\phi_{L,\alpha})^2\right] \end{aligned} \tag{3.11}$$

[1] It is exact if the nonlinear terms in (3.7) are properly normal ordered.

with right and left bosonic fields defined as $\partial_x \phi_{R(L),\alpha} = v_\alpha/\hbar \pm \pi \delta\rho_\alpha$. This procedure is equivalent to the conventional linear bosonization procedure where the fermionic spectrum is linearized at the Fermi points.

In the spin-charge basis,

$$\rho_{c,s} \equiv \rho_\uparrow \pm \rho_\downarrow \qquad \text{and} \qquad v_{c,s} = \frac{v_\uparrow \pm v_\downarrow}{2} \,, \tag{3.12}$$

the harmonic theory (3.11) is described by a sum of two independent harmonic fluid Hamiltonians, one for charge and the other for spin degrees of freedom

$$H \approx \frac{\rho_0}{4} \int \mathrm{d}x \left(4v_c^2 + \pi^2 \hbar^2 \delta\rho_c^2 + 4v_s^2 + \pi^2 \hbar^2 \delta\rho_s^2 \right) . \tag{3.13}$$

After linearization, the quantum Riemann-Hopf Eq. (3.9) reduces to (where $\pm$ stands for $\chi = \{R, L\}$ respectively)

$$\dot{k}_{\alpha,\chi} \pm \hbar\pi\rho_0 \, \partial_x k_{\alpha,\chi} = 0 \,, \qquad \alpha = \{\uparrow, \downarrow\} \,; \tag{3.14}$$

from which we identify that the quadratic excitations propagate like wave equations with sound velocities $u_{charge} = u_{spin} = \pi\hbar\rho_0$, equal for spin and charge. Turning on interactions between fermions generally renormalizes spin and charge sound velocities differently and results in genuine spin-charge separation at the level of harmonic approximation. The spin-Calogero-Sutherland model happens to be very special in this respect. Despite a non-trivial interaction for spin and charge, their sound velocities remain the same.

Although spin and charge are not truly separated for a free fermion system (and for the sCM), the interaction between spin and charge is absent at the level of the harmonic approximation (3.13). This interaction appears if nonlinear corrections to (3.13) are taken into account (e.g., by the fully nonlinear Hamiltonian (3.10)) and due to gradient corrections to the hydrodynamics. The latter are not considered in this chapter.

In the proper classical limit $\hbar \to 0$ all terms of (3.10) but the velocity terms vanish (Fermi statistics does not exist for classical particles). Instead, we are interested in a "semi-classical" limit in which $\rho \sim v/\hbar$. In this limit we rescale time and velocity by $\hbar$ ($t \to t/\hbar$ and $v \to \hbar v$) and measure everything in length units. This is equivalent to dropping all $\hbar$ from equations. For instance, the

Hamiltonian (3.10) becomes

$$H = \int \mathrm{d}x \left\{ \frac{1}{2}\rho_\uparrow v_\uparrow^2 + \frac{1}{2}\rho_\downarrow v_\downarrow^2 + \frac{\pi^2}{6}\left(\rho_\uparrow^3 + \rho_\downarrow^3\right) \right\}. \tag{3.15}$$

We replace the commutation relations (3.8) by the corresponding classical Poisson brackets (for up and down species)

$$\{\rho_\alpha(x), v_\beta(y)\} = \delta_{\alpha\beta}\delta'(x-y) \tag{3.16}$$

and consider the classical equations of motion generated by the Hamiltonian together with the Poisson brackets. In the remainder of the chapter all hydrodynamic equations are obtained in this *semi-classical* limit.

3.3 The spin-Calogero model

In this work we concentrate on the hydrodynamics of the sCM (3.1) for the case of spin-1/2 fermions with an anti-ferromagnetic sign of interaction. It is convenient to impose periodic boundary conditions, i.e. consider particles living on a ring of the length L. This Hamiltonian is given by

$$H = -\frac{\hbar^2}{2}\sum_{j=1}^{N}\frac{\partial^2}{\partial x_j^2} + \frac{\hbar^2}{2}\left(\frac{\pi}{L}\right)^2 \sum_{j\neq l}\frac{\lambda(\lambda - \mathbf{P}_{jl})}{\sin^2\frac{\pi}{L}(x_j - x_l)} \tag{3.17}$$

and is known to be integrable[43]. All eigenstates of can be enumerated by the distribution function

$$\nu(\kappa) = \nu_\uparrow(\kappa) + \nu_\downarrow(\kappa). \tag{3.18}$$

Here, κ are integer-valued quantum numbers identifying a given state in a Bethe Ansatz description and $\nu_{\uparrow,\downarrow}(\kappa) = 0, 1$ depending on whether a given κ is present in the solution of the Bethe Ansatz equations.

The total momentum P and energy E of the eigenstate are given in terms

of the distribution function $\nu(\kappa)$ as[63, 64]:

$$P = \left(\frac{2\pi}{L}\right) \sum_{\kappa=-\infty}^{+\infty} \kappa\, \nu(\kappa), \tag{3.19}$$

$$E = E_0 + \left(\frac{1}{2}\right)\left(\frac{2\pi}{L}\right)^2 \epsilon, \tag{3.20}$$

$$\epsilon = \sum_{\kappa=-\infty}^{+\infty} \kappa^2 \nu(\kappa) + \frac{\lambda}{2} \sum_{\kappa,\kappa'} |\kappa - \kappa'| \nu(\kappa)\nu(\kappa'), \tag{3.21}$$

where $E_0 = \frac{\pi^2\lambda^2}{6} N(N^2-1)$ is the energy of a reference state[64]. The numbers of particles with spin up and spin down are separately conserved in (5.1) and are given by

$$N_{\uparrow,\downarrow} = \sum_{\kappa=-\infty}^{+\infty} \nu_{\uparrow,\downarrow}(\kappa). \tag{3.22}$$

The ground state wave function for (5.1) is[41, 64]

$$\psi_{GS} = \prod_{j<l} \left|\sin\frac{\pi}{L}(x_j - x_l)\right|^{\lambda} \prod_{j<l} \left[\sin\frac{\pi}{L}(x_j - x_l)\right]^{\delta(\sigma_j,\sigma_l)} \exp\left[i\frac{\pi}{2}\mathrm{sgn}\,(\sigma_j - \sigma_l)\right] \tag{3.23}$$

and corresponds to the distributions [2]

$$\begin{aligned} \nu_\uparrow(\kappa) &= \theta(-N_\uparrow/2 < \kappa < N_\uparrow/2)\ , \\ \nu_\downarrow(\kappa) &= \theta(-N_\downarrow/2 < \kappa < N_\downarrow/2)\ . \end{aligned} \tag{3.24}$$

3.4 Gradientless hydrodynamics of the spin-Calogero model

Following the example of free fermions, we consider a uniform state specified by the following distributions

$$\nu_\uparrow(\kappa) = \theta(\kappa_{L\uparrow} < \kappa < \kappa_{R\uparrow}), \tag{3.25}$$

$$\nu_\downarrow(\kappa) = \theta(\kappa_{L\downarrow} < \kappa < \kappa_{R\downarrow}). \tag{3.26}$$

[2] We neglect $1/N$ corrections and replace combinations like $(N-1)/2$ simply by $N/2$.

This state is the lowest energy state with given numbers of particles, momentum, and total spin current. It is specified by four integer numbers $\kappa_{L,R;\uparrow,\downarrow}$. All physical quantities such as energy, momentum, and higher integrals of motion of the state can be expressed in terms of these numbers using (4.23,3.19,3.20). These conserved quantities written as integrals over constant quantities are:

$$N_\alpha = \int \mathrm{d}x\, \rho_\alpha = \frac{2\pi}{L} \int \mathrm{d}x \left[\frac{\kappa_{R\alpha} - \kappa_{L\alpha}}{2\pi} \right] , \qquad \alpha = \{\uparrow, \downarrow\} \quad (3.27)$$

$$P = \int \mathrm{d}x\, j_c = \left(\frac{2\pi}{L} \right)^2 \sum_{\alpha=\{\uparrow,\downarrow\}} \int \mathrm{d}x \left[\frac{\kappa_{R\alpha}^2 - \kappa_{L\alpha}^2}{4\pi} \right] . \quad (3.28)$$

Comparison with (3.2,3.3) suggests the following hydrodynamic identifications:

$$v_\uparrow \pm \pi\rho_\uparrow \equiv \frac{2\pi}{L}\, \kappa_{(R,L);\uparrow} , \quad (3.29)$$

$$v_\downarrow \pm \pi\rho_\downarrow \equiv \frac{2\pi}{L}\, \kappa_{(R,L);\downarrow} . \quad (3.30)$$

In the main body of the chapter we use $v_{\uparrow,\downarrow}$ and refer to them as to "velocities". At this point they have been introduced "by analogy" with the case of free fermions. In Appendices A,B,C we show that these velocities are indeed conjugated to the corresponding densities and explain their relations to the true hydrodynamic velocities. In fact, in the most interesting case to us, namely the CO regime (see below) these velocities coincide with the true hydrodynamic velocities defined in Appendix B. The total momentum (3.28) of the system in terms of (3.29,3.30) is

$$P = \int \mathrm{d}x \big(\rho_\uparrow v_\uparrow + \rho_\downarrow v_\downarrow \big) . \quad (3.31)$$

One can also express the energy (3.20) in terms of these hydrodynamic variables. Because of the non-analyticity (presence of an absolute value) in formula (3.20) it is convenient to consider different physical regimes. These regimes are defined by the mutual arrangement of the supports of the distribution functions (3.25,3.26). There are six different regimes, that reduce to three physically non-equivalent ones using the permutation $\uparrow \leftrightarrow \downarrow$. The distributions corresponding to different regimes are shown in Fig. 3.1:

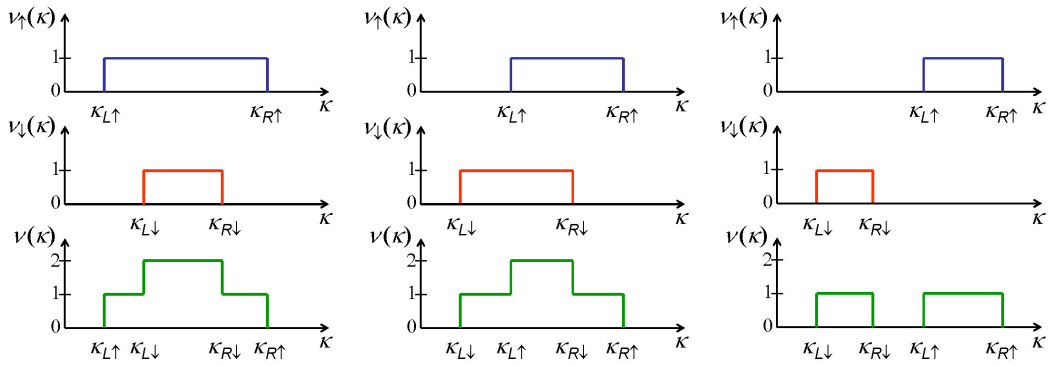

Figure 3.1: Distribution functions are shown for the three nonequivalent regimes: *Complete Overlap* in (a), *Partial Overlap* in (b) and *No Overlap* in (c). Three additional regimes exist, but are physically equivalent to the ones considered in these pictures and can be obtained by exchanging $\uparrow \leftrightarrow \downarrow$.

- *Complete Overlap (CO) regime.* The support of $\nu_\downarrow$ is completely contained in $\nu_\uparrow$ (or vice versa). This is the regime considered in Ref. [41], where its exact solution was given.

- *Partial Overlap (PO) regime.* The supports of $\nu_\uparrow$ and of $\nu_\downarrow$ only partially overlap.

- *No Overlap (NO) regime.* The supports of $\nu_\uparrow$ and of $\nu_\downarrow$ do not overlap at all.

Notice that the small fluctuations around the singlet ground state (with $\rho_s = 0$) belong to the first two regimes.

In terms of the hydrodynamic variables the three regimes are summarized in Fig. 3.2 and are defined by the following inequalities:

$$\text{Complete Overlap} \;\rightarrow\; |v_s| < \frac{\pi}{2}\,|\rho_s|\,, \tag{3.32}$$

$$\text{Partial Overlap} \;\rightarrow\; \frac{\pi}{2}\,|\rho_s| < |v_s| < \frac{\pi}{2}\,\rho_c\,, \tag{3.33}$$

$$\text{No Overlap} \;\rightarrow\; \frac{\pi}{2}\,\rho_c < |v_s|\,, \tag{3.34}$$

where we switched to the spin and charge degrees of freedom defined by (3.12). To simplify the presentation we give here formulas only for the CO regime

$$-\frac{\pi\rho_s}{2} < v_s < \frac{\pi\rho_s}{2}\,, \tag{3.35}$$

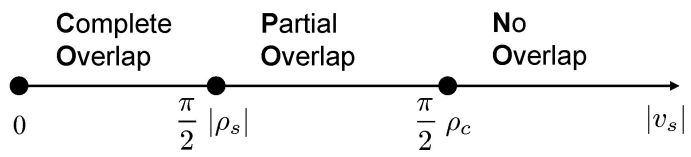

Figure 3.2: Diagram capturing all cases

where we also assumed that $\rho_s > 0$. The opposite case $\rho_s < 0$ can be obtained exchanging up and down variables. The other regimes and formulae valid for all regimes are considered in detail in Appendix C.

In the CO regime (3.35), the Hamiltonian can be written as

$$H_{\rm CO} = \int {\rm d}x \left\{ \frac{1}{2}\rho_\uparrow v_\uparrow^2 + \frac{1}{2}\rho_\downarrow v_\downarrow^2 + \frac{\lambda}{2}\rho_\downarrow \big(v_\uparrow - v_\downarrow\big)^2 + \frac{\pi^2\lambda^2}{6}\rho_c^3 + \frac{\pi^2}{6}\big(\rho_\uparrow^3 + \rho_\downarrow^3\big) + \frac{\lambda\pi^2}{6}\big(2\rho_\uparrow^3 + 3\rho_\uparrow^2\rho_\downarrow + 3\rho_\downarrow^3\big) \right\} \quad (3.36)$$

It is obtained by expressing (3.20,3.21) in terms of the hydrodynamic variables (3.29,3.30) using (3.35). As in the case of free fermions (see Sec. 3.2) we now consider $\rho_{\uparrow,\downarrow}(x,t)$ and $v_{\uparrow,\downarrow}(x,t)$ as space and time dependent classical hydrodynamic fields with Poisson brackets (3.16). Of course, going from the energy of the uniform state (3.25,3.26) to the nonuniform hydrodynamic state we neglected gradients of density and velocity fields. We refer to this approximation as to *gradientless hydrodynamics*. The equations of motion generated by the Hamiltonian (3.36) with Poisson brackets (3.16) can be used only when gradients can be neglected compared to the gradientless terms. This means that one can use this gradientless hydrodynamics only at relatively small times (compared to the time of the gradient catastrophe, see the discussion below).

Before analyzing the more general case let us consider some special limits of (3.36).

3.4.1 Spinless limit

In the fully polarized state $\rho_\downarrow = 0$ we obtain from (3.36) the gradientless Hamiltonian for the spinless Calogero-Sutherland model

$$H^{\text{spinless}} = \int_{-\infty}^{+\infty} dx \left\{ \frac{1}{2}\rho v^2 + \frac{\pi^2}{6}(\lambda+1)^2 \rho^3 \right\}, \tag{3.37}$$

where we dropped the subscript $\uparrow$. The hydrodynamics (3.37) was used in [65] to calculate the leading term of an asymptotics of a particular correlation function (Emptiness Formation Probability) for the Calogero-Sutherland model. It can, of course be, obtained by dropping gradient terms in the exact hydrodynamics derived using collective field theory [16, 51, 52].

3.4.2 $\lambda = 0$ – free fermions with spin

At the particular value $\lambda = 0$ the sCM reduces to free fermions with spin and the Hamiltonian (3.36) becomes the collective Hamiltonian for free fermions (3.15).

3.4.3 $\lambda \to \infty$ limit.

In the limit of a large coupling constant $\lambda \to \infty$ the particles form a rigid lattice and charge degrees of freedom essentially get frozen [57]. We expect to arrive at an effective spin dynamics equivalent to the Haldane-Shastry model [66, 67] (see Appendix D). This reduction to the Haldane-Shastry model is usually referred to as *freezing trick* [57]. We analyze this reduction in more detail in Sec. 3.6.

3.5 Equations of motion and separation of variables

3.5.1 Equations of motion

The classical gradientless hydrodynamics for the sCM is given by the Hamiltonian (3.36) with canonical Poisson's brackets (3.16). The classical evolution

equations generated by this Hamiltonian are

$$\begin{aligned}
\dot{\rho}_\uparrow &= -\partial_x \left\{\rho_\uparrow v_\uparrow + \lambda\rho_\downarrow (v_\uparrow - v_\downarrow)\right\}, \\
\dot{\rho}_\downarrow &= -\partial_x \left\{\rho_\downarrow v_\downarrow - \lambda\rho_\downarrow (v_\uparrow - v_\downarrow)\right\}, \\
\dot{v}_\uparrow &= -\partial_x \left\{ \frac{v_\uparrow^2}{2} + \frac{\pi^2\lambda^2}{2}(\rho_\uparrow + \rho_\downarrow)^2 + \lambda\pi^2\left(\rho_\uparrow^2 + \rho_\uparrow\rho_\downarrow\right) + \frac{\pi^2}{2}\rho_\uparrow^2 \right\}, \qquad (3.38) \\
\dot{v}_\downarrow &= -\partial_x \left\{ \frac{v_\downarrow^2}{2} + \frac{\lambda}{2}(v_\uparrow - v_\downarrow)^2 + \frac{\pi^2\lambda^2}{2}(\rho_\uparrow + \rho_\downarrow)^2 + \frac{\lambda\pi^2}{2}\left(\rho_\uparrow^2 + 3\rho_\downarrow^2\right) + \frac{\pi^2}{2}\rho_\downarrow^2 \right\}.
\end{aligned}$$

This is the system of continuity and Euler's equations for two coupled fluids (with spin up and spin down). We can also rewrite it in terms of spin and charge variables (3.12)

$$\begin{aligned}
\dot{\rho}_c &= -\partial_x \left\{\rho_c v_c + \rho_s v_s\right\}, \\
\dot{\rho}_s &= -\partial_x \left\{\rho_s(v_c - 2\lambda v_s) + (2\lambda+1)\rho_c v_s\right\}, \\
\dot{v}_c &= -\partial_x \left\{ \frac{v_c^2}{2} + (2\lambda+1)\frac{v_s^2}{2} + \frac{\pi^2}{8}\left[(2\lambda+1)^2\rho_c^2 + (2\lambda+1)\rho_s^2\right] \right\}, \qquad (3.39) \\
\dot{v}_s &= -\partial_x \left\{ v_c v_s - \lambda v_s^2 + \frac{\pi^2}{4}\rho_s\left[(2\lambda+1)\rho_c - \lambda\rho_s\right] \right\}.
\end{aligned}$$

One can see that spin and charge are not decoupled. It turns out, however, that the variables nevertheless separate and the system of four coupled equations (3.38) can be written as four decoupled Riemann-Hopf equations (similar to (3.9)) for a special linear combinations of density and velocity fields. In the following we study the interaction of spin and charge governed by the above equations.

3.5.2 Free fermions ($\lambda = 0$) and Riemann-Hopf equation

At $\lambda = 0$ equations (3.38) become the hydrodynamic equations for free fermions. Fluids corresponding to up and down spin are completely decoupled

$$\begin{aligned}
\dot{\rho}_{\uparrow,\downarrow} &= -\partial_x \left\{\rho_{\uparrow,\downarrow} v_{\uparrow,\downarrow}\right\}, \qquad (3.40) \\
\dot{v}_{\uparrow,\downarrow} &= -\partial_x \left\{ \frac{1}{2} v_{\uparrow,\downarrow}^2 + \frac{\pi^2}{2}\rho_{\uparrow,\downarrow}^2 \right\}. \qquad (3.41)
\end{aligned}$$

Let us introduce the following linear combinations of densities and velocities

$$\begin{aligned} k_{R\uparrow,L\uparrow} &= v_\uparrow \pm \pi\rho_\uparrow, \\ k_{R\downarrow,L\downarrow} &= v_\downarrow \pm \pi\rho_\downarrow. \end{aligned} \tag{3.42}$$

These combinations are nothing else but right and left Fermi momenta of free fermions. All of them satisfy the so-called Riemann-Hopf equation

$$u_t + uu_x = 0. \tag{3.43}$$

The equation is the same for all four combinations $u = k_{R,L;\uparrow,\downarrow}$ and the system (3.40,3.41) is equivalent to four decoupled Riemann-Hopf equations.

The Riemann-Hopf equation (3.43) is easily solvable with the general solution given implicitly by

$$u = u_0(x - ut). \tag{3.44}$$

Here $u_0(x)$ is an initial profile of $u(x,t)$ at $t = 0$. One should solve (3.44) with respect to u and find $u(x,t)$ - the solution of (3.43) with $u(x, t = 0) = u_0(x)$. The solution (3.44) can also be written in a parametric form

$$\begin{aligned} x &= y + t\, u_0(y), \\ u(x,t) &= u_0(y). \end{aligned} \tag{3.45}$$

This solution corresponds to the "Lagrangian picture" of fluid dynamics and states that points in the $x - u$ plane are just translated along x with velocity u, i.e., $(x, u_0) \to (x + t\, u_0, u_0)$. This picture is especially useful to solve (3.43) numerically.

We notice here that the nonlinear dynamics (3.43) without dispersive (higher gradient) terms is ill defined at large times. For any initial profile $u_0(x)$, at large times $t > t_c$ infinite gradients u_x will develop - *gradient catastrophe* - and solutions of (3.44) will become multi-valued. The classical equation (3.43) will not have a meaning for $t > t_c$. We refer to the time t_c (function of the initial profile) as to the gradient catastrophe time. The gradientless hydrodynamics is applicable only for times smaller that t_c. [3] We will discuss in more detail

[3] We notice here that for a free fermion system it is possible to assign the meaning even to the multi-valued solution of (3.44) for $t > t_c$. It is the boundary of the support of the

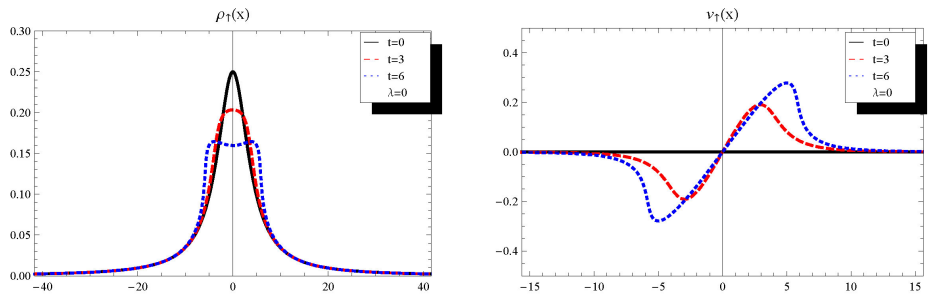

Figure 3.3: Dynamics of density field $\rho_\uparrow(x)$ (left panel) and of velocity field $v_\uparrow(x)$ (right panel) for free a fermion case ($\lambda = 0$). The initial density profile at $t = 0$ is a Lorentzian (3.46) of height $h = 0.25$ and half-width $a = 4$. The initial velocity is zero.

about validity of gradientless hydrodynamics in Sec. 3.7.

We present a simple illustration of the density and velocity dynamics for free fermion system in Fig. 3.3. It is sufficient to consider only up-spin as the evolution of up and down spins is decoupled. We chose the initial profile of the density as Lorentzian with the half-width a and height h

$$\rho_{0\uparrow}(x) = \frac{h}{1 + (x/a)^2} \tag{3.46}$$

and an initial velocity zero. We find the initial profiles of $k_{\uparrow;R,L}$ using (3.42). Then we solve the Riemann-Hopf equations (3.43) using (3.45) and find the density and velocity at any time inverting (3.42). We remark that for an arbitrary smooth bump of height h and width a the gradient catastrophe time can be estimated as $t_c \approx \frac{a}{h}$. For the evolution given by (3.43) with an initial Lorentzian profile ($u_0(x)$ given by (3.46)) one can compute the gradient catastrophe time exactly. An infinite gradient $\partial_x u \to \infty$ develops at the time

$$t_c = \frac{8}{3\sqrt{3}} \frac{a}{h}. \tag{3.47}$$

For arbitrary initial conditions we compute the gradient catastrophe time numerically.

Wigner distribution in the one-particle phase space. In this chapter we restrict ourselves to times less than the time of gradient catastrophe and assume that (3.43) has a well-defined single-valued solution.

3.5.3 Riemann-Hopf Equations for the sCM

Although the system of equations (3.38) is a system of four coupled nonlinear equations, it allows for a separation of variables. Introducing the linear combinations of fields

$$k_{R\uparrow,L\uparrow} = v_\uparrow \pm \pi\left[(\lambda+1)\rho_\uparrow + \lambda\rho_\downarrow\right] = (v_\uparrow \pm \pi\rho_\uparrow) \pm \lambda\pi\rho_c, \tag{3.48}$$

$$\begin{aligned} k_{R\downarrow,L\downarrow} &= (\lambda+1)v_\downarrow - \lambda v_\uparrow \pm \pi(2\lambda+1)\rho_\downarrow = (v_\downarrow \pm \pi\rho_\downarrow) \\ &+ \lambda(-2v_s \pm 2\pi\rho_\downarrow) \end{aligned} \tag{3.49}$$

we obtain the Riemann-Hopf equation (3.43) separately for all four $u = k_{L,R,\uparrow,\downarrow}$.

This property of variable separation is shared with the free fermion case Sec.3.5.2. We notice, however, that in the case of the sCM, variables separate only in gradientless approximation. The gradient terms neglected in this chapter will couple the hydrodynamic equations in an essentially non-separable[4] way.

The separation of variables in terms of (3.48,3.49) is not so surprising. One can recognize (3.48,3.49) as dressed (physical) "Fermi" momenta of (an asymptotic) Bethe Ansatz. The integrals of motion of sCM are separated in terms of these Fermi momenta and the same is true for the equations of motion. We do not interrupt the presentation with this connection with the Bethe Ansatz solution of the sCM but devote the Appendix A to this purpose.

It is convenient to summarize the gradientless hydrodynamics of sCM by the picture in a "single-particle" phase space showing space-dependent Fermi momenta. [5] We plot the space-dependent Fermi momenta in an $x-k$ plane as four smooth lines. In the CO regime considered here (see Appendix C for other regimes) the Fermi momenta are ordered as

$$k_{L\uparrow}(x) < k_{L\downarrow}(x) < k_{R\downarrow}(x) < k_{R\uparrow}(x). \tag{3.50}$$

We fill the space between those lines with particles obeying the following rules of particles with fractional exclusion statistics [48] (see Appendix A) (i) each

[4] At least one will not be able to separate variables considering simple linear combinations of fields. To the best of our knowledge variables in sCM do not separate or, at least, an appropriate change of variables has not been found yet.

[5] We would like to thank A. Polychronakos who encouraged us to present this picture.

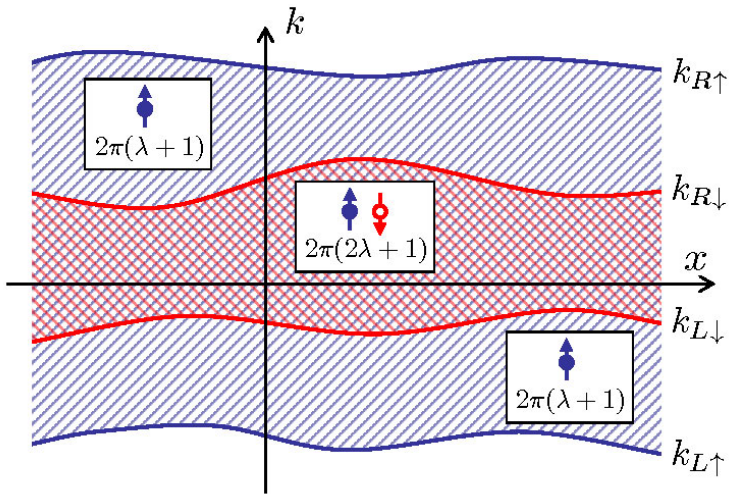

Figure 3.4: Phase-space diagram of a hydrodynamic state characterized by four space-dependent Fermi momenta.

particle occupies a phase space volume $2\pi(\lambda+1)$ if there are no particles of the other species in this volume, (ii) two particles with opposite spins occupy a phase space volume $2\pi(2\lambda+1)$ (or $2\pi(\lambda+1/2)$ per particle). The velocity $v_\uparrow(x)$ is visualized as a center of a spin-up stripe on Figure 3.4 (see (B.5)). The interpretation of $v_\downarrow(x)$ is a bit less straightforward. It should be thought of as a weighted average of positions of centers of both stripes (B.5).

3.6 Freezing trick and hydrodynamics of the Haldane-Shastry model

Here we consider the limit of large coupling constant $\lambda \to \infty$. In this limit we expect that particles form a one-dimensional lattice and only spin dynamics is important at low energies. We refer to this limit as to a freezing of the charge. We are interested in fluctuations around the uniform state with a given charge density. It can be seen from Fig. 3.4 that particles occupy the volume $2\pi(\lambda+1/2)$ of the phase space when both species are present. Therefore, the natural expansion parameter is $\mu = \lambda+1/2$ instead of λ.[6] We will see that the leading in μ term of the dynamics results in charge freezing, while the next to

[6] Of course, first orders of the expansion are not sensitive to this shift.

leading term gives the non-trivial spin dynamics of the lattice model known as the Haldane-Shastry model [66, 67]

$$H_{\rm HSM} = 2\sum_{j<l} \frac{S_j \cdot S_l}{(j-l)^2}. \tag{3.51}$$

This model is known to be integrable.[43] The freezing procedure described is referred to as "freezing trick" and was introduced by Polychronakos [57]. Our goal is to implement the procedure in a hydrodynamic description.

Before proceeding to a regular expansion of the equations of motion we start with a heuristic argument. We rewrite the hydrodynamic Hamiltonian (3.36) in terms of spin and charge variables (3.12) and consider first the two leading terms in a $1/\mu$ expansion

$$\begin{aligned} H &= \int {\rm d}x \left\{ \frac{1}{2}\rho_c v_c^2 + \rho_s v_c v_s + \mu \rho_c v_s^2 - \left(\mu - \frac{1}{2}\right)\rho_s v_s^2 + \frac{\pi^2\mu^2}{6}\rho_c^3 \right. \\ &+ \left. \frac{\pi^2}{4}\mu\rho_c\rho_s^2 - \frac{\pi^2}{12}\left(\mu - \frac{1}{2}\right)\rho_s^3 \right\} \qquad (3.52) \\ &= \int {\rm d}x \left\{ \frac{\pi^2}{6}\mu^2\rho_c^3 + \mu\left[\rho_c v_s^2 - \rho_s v_s^2 + \frac{\pi^2\rho_c\rho_s^2}{4} - \frac{\pi^2\rho_s^3}{12}\right] + O(1) \right\} \qquad (3.53) \end{aligned}$$

The first term proportional to μ^2 comes from the energy of a static lattice while the second term proportional to μ gives the Hamiltonian of the Haldane-Shastry model in the hydrodynamic formulation (see Appendix D), i.e., describes the spin dynamics. Note that ρ_c here should be considered as a constant equal to the inverse lattice spacing of the charge lattice.

To build a systematic expansion in $1/\mu$ we go to the hydrodynamic evolution equations given in (3.39). We introduce the following series in $1/\mu = 1/(\lambda + 1/2)$ for the space-time dependent fields.

$$\begin{aligned} u &= u^{(0)} + \frac{1}{\mu}u^{(1)} + \frac{1}{\mu^2}u^{(2)} + ... \\ u &\to \rho_c, v_c, \rho_s, v_s \end{aligned}$$

and re-scale time $t = \tau/\mu$ (or $\partial_t = \mu\partial_\tau$). We substitute these expansions into (3.39) and compare order by order in μ. Let us consider few leading orders

explicitly.

3.6.1 $O(\mu)$

In this order the only non-trivial equation gives

$$0 = -\partial_x \left[\rho_c^{(0)^2}\right] \tag{3.54}$$

and implies that $\rho_c^{(0)}$ is constant in space.

3.6.2 $O(1)$

At this order we have

$$\begin{aligned}
\dot{\rho}_c^{(0)} &= 0, && (3.55)\\
\dot{\rho}_s^{(0)} &= -\partial_x \left\{2\rho_c^{(0)} v_s^{(0)} - 2\rho_s^{(0)} v_s^{(0)}\right\}, && (3.56)\\
\dot{v}_c^{(0)} &= -\partial_x \left\{v_s^{(0)^2} + \pi^2 \rho_c^{(0)} \rho_c^{(1)} + \frac{\pi^2}{4}\rho_s^{(0)^2}\right\}, && (3.57)\\
\dot{v}_s^{(0)} &= -\partial_x \left\{-v_s^{(0)^2} + \frac{\pi^2}{2}\rho_c^{(0)}\rho_s^{(0)} - \frac{\pi^2}{4}\rho_s^{(0)^2}\right\}. && (3.58)
\end{aligned}$$

Combining (3.54) and (3.55) we see that $\rho_c^{(0)}$ is a constant independent of space-time. The evolution equations (3.56) for spin density, $\dot{\rho}_s^{(0)}$ and (3.58) for the spin velocity $\dot{v}_s^{(0)}$ do not depend on the dynamics of the charge and are precisely the ones obtained for the Haldane-Shastry model (compare to (D.17)). We refer the reader to the Appendix D for more details on the hydrodynamics of the Haldane-Shastry model.

Equation (3.57) is important in resolving a well-known "paradox". In the original spin-Calogero model the momentum of the system is identical to the total charge current since all particles in the model have the same charge. On the other hand in the Haldane-Shastry model the momentum is carried by spin excitations and superficially no charge motion is involved. One can ask how this is compatible with getting the Haldane-Shastry model in the limit $\lambda \to \infty$ from the spin Calogero model. Equation (3.57) is necessary to make sure that the the current density $j(x) = \rho_c v_c + \rho_s v_s$ is globally conserved at a given order in $1/\mu$. Since $\rho_c^{(0)}$ is a constant in space-time we expect from

(3.56) and (3.58) that $v_c^{(0)}$ evolves according to (3.57) to ensure that the current density is conserved. As a result, there is a charge motion associated with the momentum but in the large λ limit this "recoil" momentum is absorbed by the whole charge lattice.

3.6.3 $O(1/\mu)$

For the sake of brevity we do not write down the equations at this order but make some comments instead. In the previous order, $O(1)$ we noticed (see eqs. (3.56) and (3.58) that spin degrees of freedom evolve as the charge is essentially frozen and at that order there is no feedback of the charge degrees of freedom on the spin. However, in the order $O(1/\mu)$ we have feedback terms in both evolution equations for ρ_s and v_s. As an example we have $\dot{\rho}_s^{(1)} = -\partial_x \left\{ ... + 2v_s^{(0)}\rho_c^{(1)} + v_c^{(0)}\rho_s^{(0)} + ... \right\}$ and $\dot{v}_s^{(1)} = -\partial_x \left\{ ... + v_c^{(0)}v_s^{(0)} + \frac{\pi^2}{2}\rho_c^{(1)}\rho_s^{(0)} + ... \right\}$ which clearly show that there is a charge feedback into the spin sector.

3.6.4 Evolution equations for the Haldane-Shastry model from the freezing trick

The shortest way to evolution equations for Haldane-Shastry model is to take the $\lambda \to \infty$ limit directly in the Riemann-Hopf equations (3.43). After rescaling the time $t = \tau/\mu$ we have

$$\tilde{k}_\tau + \tilde{k}\tilde{k}_x = 0, \tag{3.59}$$

where $\tilde{k} = k/\mu = k/(\lambda + 1/2)$. In the large λ limit we have using (3.48,3.49) $\tilde{k}_{R\uparrow,L\uparrow} \to \pm\pi\rho_c$ and $\tilde{k}_{R\downarrow,L\downarrow} = -2v_s \pm 2\pi\rho_\downarrow$. Then the equation (3.59) gives evolution equations for the Haldane-Shastry model with (D.12,D.15).

3.7 Illustrations

It is relatively simple to obtain the evolution of arbitrary (smooth) initial density and velocity profiles solving equations of the gradientless hydrodynamics (3.39) numerically. One can do it very effectively using the fact that the dynamics is separated into four Riemann-Hopf equations (3.43) and using their

general solutions (3.45). In this section we give numerical results for charge and spin dynamics corresponding to a relaxation of a (spin) polarized center. These results show that due to the nonlinearity of the equations spin can drag charge in the spin-Calogero model. We notice here that in the examples considered in this section the dynamics belong to the CO regime. [7]

3.7.1 Charge dynamics in a spin-singlet sector

As a first example we consider the initial conditions $\rho_s, v_s = 0$ and some arbitrary initial conditions for ρ_c and v_c. It is easy to see from (3.39) that the spin density and spin velocity remain zero at any time while the charge degrees of freedom satisfy

$$\begin{aligned} \dot{\rho}_c &= -\partial_x(\rho_c v_c), \\ \dot{v}_c &= -\partial_x \left\{ \frac{v_c^2}{2} + \frac{\pi^2 \left(\lambda + \frac{1}{2}\right)^2 \rho_c^2}{2} \right\}. \end{aligned} \tag{3.60}$$

The hydrodynamics (3.60) are identical to the one of the Calogero-Sutherland model with one species of particles (except for the change $\lambda + 1 \to \lambda + 1/2$). It can be written as a system of two Riemann-Hopf equations (3.43) for fields $v_c \pm \pi(\lambda + 1/2)\rho_c$.

We conclude that the charge dynamics do not affect spin in a spin-singlet state at least in the gradientless limit. It is interesting to see how spin dynamics affect the charge one.

3.7.2 Dynamics of a polarized center

To see how spin drags charge we start with an initial configuration with static and uniform charge background. We assume that initially there is no spin current but there is a non-zero polarization given by a Lorentzian profile:

$$t = 0: \qquad \rho_c = 1, \qquad v_c = 0, \qquad v_s = 0, \qquad \rho_s = \frac{h}{1 + (x/a)^2}, \tag{3.61}$$

[7] In exotic cases involving boundaries between CO and PO regimes one notices singularities developing at the boundary and we expect gradient corrections to correct these singularities.

i.e., there is an excess of particles with spin up over particles with spin down near the origin. The maximal polarization is h and a half-width of the polarized center is a. As an illustration of spin and charge dynamics we present a solution of (3.39) with initial conditions (3.61) corresponding to $h = 0.25$ and $a = 4$. Some important comments are in order.

3.7.2.1 Applicability of gradientless hydrodynamics

The hydrodynamic equations we use (3.39) neglect gradient corrections and, therefore, are approximate. They can be applied only under the condition that the neglected higher gradient terms are small compared to the terms taken into account in (3.39). Of course, the exact criteria can be written only when the form of the higher gradient terms are known explicitly. Here, we are going to use a much simpler criterion. We require that all fields change slowly at the scale of the inter-particle spacing. The uniform background $\rho_c = 1$ defines the inter-particle spacing and the characteristic scale for hydrodynamic fields to be 1 and we require $\partial_x f \ll 1$ for all fields at all x and t that we consider.

One can easily check that $\partial_x \rho_s(x, t = 0) \ll 0.1$ for all x with the initial profile (3.61) (in fact, the maximal derivative is approximately 0.041). Because of the gradient catastrophe this condition will be broken at some time and we can trust the results obtained from (3.39) only up to that time. To be well within this criterion all our fields satisfy $\partial_x f < 0.3$ at any given time.

Let us start with the solutions for the case of free fermions, i.e., $\lambda = 0$.

3.7.2.2 Free fermions with spin: $\lambda = 0$

We present the results for spin and charge dynamics of free fermions with polarized center initial conditions (3.61) on left panels of Figures 3.5,3.6. The profiles $\rho_s(x)$ and $\rho_c(x) - 1$ are shown as functions of x for times $\tau = 0, 1, 3.5, 7$ respectively. Here we use a rescaled time $\tau = (\lambda + 1/2)t = t/2$ for future convenience.

The dynamics is separated into four Riemann-Hopf equations for each Fermi momentum. The initial conditions (3.61) can be written as Lorentzian peaks for each of the four Fermi momenta of fermions and all four Fermi velocities are different. This results in a splitting of an initial Lorentzian peak into four peaks at larger times which can be easily seen on the left panel of

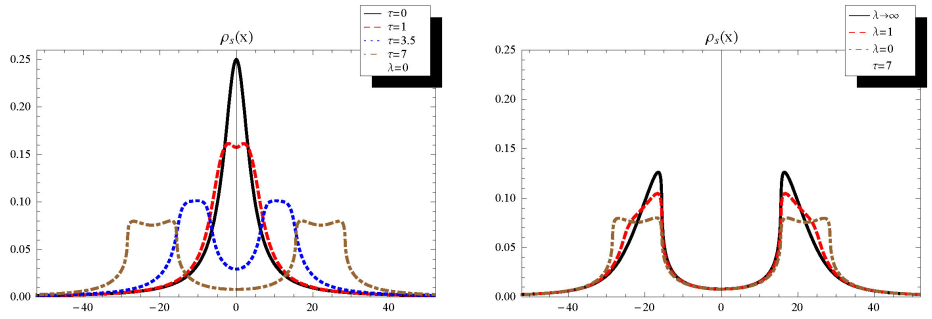

Figure 3.5: *Left panel*: Spin dynamics of polarized center for free fermions. The initial charge density profile is constant and the initial spin density profile is a Lorentzian (3.61) of a height $h = 0.25$ and a half-width $a = 4$. Profiles at times $\tau = t/2 = 0, 1, 3.5, 7$ are shown. *Right panel*: A snapshot of spin density at time $t = \tau/(\lambda + 1/2)$ for $\tau = 7$ for $\lambda = 0, 1, \infty$.

Fig. 3.5. In addition to this linear effect the nonlinear effects of steepening the wave front can also be seen. The latter will render gradientless hydrodynamics inapplicable at later times.

The drag of charge by spin clearly seen in Fig. 3.6 has an essentially nonlinear nature. There is an excess (deficit) of particles with spin up (down) at the origin at the initial moment. The particles with spin up will move away from the center while spin down particles will move towards the center. However, the average velocity of spin up particles is larger than the average velocity of spin down particles as it is proportional to the density of those particles. Therefore, the initial motion of particles away from and towards the origin creates a charge depletion in the center and charge density maxima away from that depletion. This gives a qualitative explanation of the picture of charge dragged by spin which is shown in the left panel of Fig. 3.6. Notice that in this explanation we used the dependence of propagation velocity on the amplitude of the wave – an essentially nonlinear effect.

3.7.2.3 λ-dependence of spin and charge dynamics

To see the effects of the interaction on spin and charge dynamics we show the spin and charge density profiles at a fixed time for different values of the coupling constant λ in the right panels of Figures 3.5,3.6 respectively. It is convenient to use the scaling dictated by the $\lambda \to \infty$ limit considered in detail

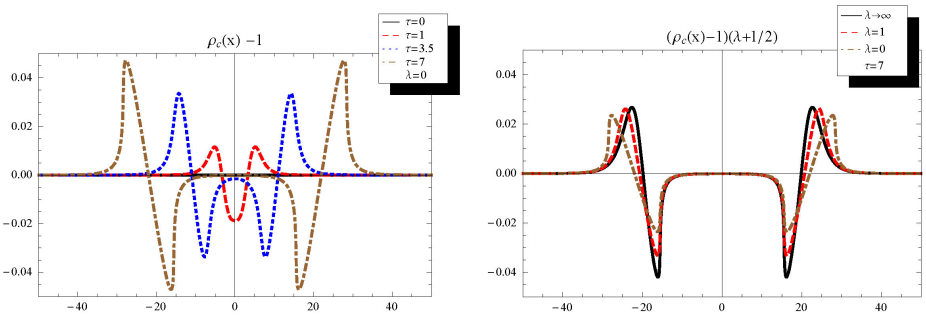

Figure 3.6: *Left panel*: Charge dynamics of polarized center for free fermions. The initial charge density profile is constant and the initial spin density profile is a Lorentzian (3.61) of a height $h = 0.25$ and a half-width $a = 4$. Profiles at times $\tau = t/2 = 0, 1, 3.5, 7$ are shown. *Right panel*: A snapshot of a rescaled charge density $(\lambda+1/2)(\rho_c-1)$ at time $t = \tau/(\lambda+1/2)$ for $\tau = 7$ for $\lambda = 0, 1, \infty$.

in Section 3.6. Namely, we use a rescaled time $\tau = (\lambda + 1/2)t$ and rescale the deviation of the charge density from the uniform by background plotting $(\lambda+1/2)(\rho_c-1)$ for the charge density. The charge and density profiles found at $\tau = 7$ are remarkably close for λ ranging from the free fermion case $\lambda = 0$ to the limit of the Haldane-Shastry model $\lambda \to \infty$.

The results confirm that the effect of spin dynamics on charge is suppressed by $1/\lambda$ for large λ. For a given initial spin density profile the maximal amplitude of charge deviation is of the order $1/(\lambda + 1/2)$.

3.8 Conclusions

In this chapter we considered a classical two-fluid hydrodynamics derived as a semiclassical limit of the quantum spin-Calogero model (sCM) defined in (5.1). The model (5.1) is essentially quantum as it involves identical particles and a particle permutation operator. There is an essential ambiguity in how one takes a "semiclassical" limit. Here we considered a limit which is obtained when the density of particles goes to infinity so that $\hbar\rho$ is kept finite in the limit $\hbar \to 0$. We have also neglected gradient corrections to hydrodynamic equations assuming that fields change very slowly on the scale of the inter-particle spacing. With all these assumptions, hydrodynamic equations are obtained from the Bethe ansatz solution of sCM. They have the simplest form when written in terms of fields corresponding to dressed Fermi momenta of

Bethe ansatz. In terms of these fields (3.48,3.49), the equations separate into four independent Riemann-Hopf equations (3.43) which are trivially integrable.

We presented some particular solutions of the hydrodynamic equations illustrating interactions between spin and charge. There is no true spin-charge separation in the sCM. However, in the limit of large coupling constant $\lambda \to \infty$ the spin degrees of freedom do not affect the dynamics of charge degrees of freedom. The spin dynamics then is described by the hydrodynamics of the Haldane-Shastry spin model. We considered explicitly both this limit ($\lambda \to \infty$) and the limit ($\lambda = 0$) of free fermions with spin.

The quantum scattering phase of particles interacting via $1/x^2$ potential is momentum independent. Moreover, it is the same for particles of the same species and for particles of different species because of the $SU(2)$ invariance of (5.1). It is well known that this allows one to describe the sCM as a model of free exclusons - i.e. , particles obeying an exclusion statistics [44–47]. We do not keep the $SU(2)$ invariance of the original quantum model (5.1) explicitly when taking the classical limit. However, this invariance is responsible for the variable separation that we observed in our hydrodynamics. We note here that the sCM can be generalized to the "multi-species Calogero model" [68]. Because of the absence of the $SU(2)$ invariance for a more general two-species Calogero model one does not have the separation of variables for the corresponding hydrodynamics.

The classical gradientless hydrodynamics derived in this chapter captures many of the features of sCM. It is straightforward to generalize our results to the case of the $SU(n)$ Calogero model and to use the gradientless hydrodynamic equations for problems where field gradients can be neglected. In Chapter 5 and a separate publication [69] we use these equations in instanton calculations for the computation of emptiness formation probability similar to what was done in Refs [65, 70].

However, some important features of the hydrodynamic description do require an account of gradient corrections. First of all, the exact hydrodynamic equations are expected not to have an exact separation of variables. The obtained Riemann-Hopf equations (3.43) acquire gradient corrections and four such equations written for (3.48,3.49) are expected to be coupled by those gradient corrections similarly to the case of the one-species Calogero-Sutherland

model [71]. Similarly, we expect that the equations with gradient corrections will have soliton solutions corresponding to quasi-particle excitations of the quantum model (5.1) [16, 43, 71].

The hydrodynamic description of quantum sCM has been addressed in Refs.[54, 55] using the collective field theory approach. The comparison of our results with results of those works is not straightforward. One should apply the collective formulation of Refs.[54, 55] to the states from an appropriate sector of coherent states and take a corresponding classical limit. It would be especially interesting to see how the three hydrodynamic regimes discussed here appear from Refs.[54, 55]. One can also recognize a lot of similar looking terms in quantum hydrodynamics of Refs. [55] and in our classical gradientless hydrodynamics. It would also be very important to understand the role of the degeneracy due to the Yangian symmetry in the sCM on its hydrodynamics. The latter degeneracy was neglected in the classical hydrodynamics in this chapter.

As mentioned in the thesis introduction (chapter 1), one speciality of the Calogero family is that it remains integrable even in the presence of an external harmonic trap. To the best of our knowledge this is the only example of this kind. The presence of an external harmonic trap is most often unavoidable in cold atomic experiments. In the next chapter we will study the spin-Calogero model in the presence of an external trap.

Chapter 4

Cold Fermi-gas with inverse square interaction in a harmonic trap

4.1 Introduction

The possibility of creating one and quasi-one-dimensional systems by confining cold atoms in cigar-shaped harmonic traps[8–12, 72] has raised interest in one-dimensional models of many body systems. Standard perturbative methods developed in many-body theory are often not applicable to one-dimensional models because the low dimensionality effectively makes any interaction strong. On the other hand there are some non-perturbative methods which work specifically for particular (integrable) models in one dimension. The Bethe Ansatz approach, for example, was successfully used in constructing the complete thermodynamics of quantum integrable systems. However, this approach is not very suitable for studying the dynamics and correlation functions, due to the complexity of Bethe Ansatz solutions. To address dynamic questions the method of collective field theory[58–60] was developed. It is essentially a hydrodynamic approach to many body systems. Many phenomena such as spin-charge dynamics[15], solitons[16], shock waves[73], spin density evolution [10, 11] and sound wave propagation[9] which have become of increasing experimental interest[8–11, 74, 75] can be studied via the collective field theory formalism. This formalism can be used both in combination with the Bethe Ansatz for integrable models where it can even produce some exact results for dynamical problems or as a phenomenological approach

where exact microscopic derivations are too difficult or even impossible. The hydrodynamic approach allows to study truly nonlinear and nonperturbative dynamic behavior[15] of many body systems. Linearized hydrodynamic equations are equivalent to the method of bosonization which was widely used for treating interacting systems in one dimension[38, 76]. The well-known phenomenon of spin-charge separation in the two-component fermions with contact interactions was studied by such a Luttinger Liquid description[77–79]. Similar studies of spin-charge separation and dynamics in two-component Fermi-Hubbard model have been adressed using techniques of time-dependent density matrix renormalization group[80] and time-dependent spin-density-functional theory[81, 82].

In Refs. [15, 69] the collective field theory approach was applied to the well-known spin-Calogero model [43, 83]to study the coupled nonlinear dynamics of spin and charge. The model has a long range $1/r^2$ interaction and is not the easiest one to realize experimentally. On the other hand, the potential $1/r^2$ should be considered as relatively short ranged in one dimension[1]. Indeed, we will see that, e.g. , density and spin denssity profiles for a model with $1/r^2$ interaction are qualitatively similar to the ones for the model with contact (short-ranged) interactions[2]. Therefore, although the interaction decays as a power law, it is very closely linked to short-ranged interactions due to one-dimensionality. The model has another advantage: it is integrable and the integrability is not destroyed by the presence of an external harmonic potential[84] $V(x) = \frac{m\omega^2}{2}x^2$. In contrast, for, say, the quantum integrable model of fermions with delta-interaction[85] the integrability is destroyed by an external harmonic potential.

In this chapter, we explore the effects of the harmonic trap on the collective behavior of the spin-Calogero model (sCM) at zero temperature. Its

[1]Notice that the solution to Laplace equation in 1D behaves as $\sim r$, ie, it grows with distance. Thus $1/r^2$ in 1D being three powers lower is definitely "shorter-ranged" than 1D Coulomb potential. Hence, although it is sometimes conventional to term power law interactions as "long ranged" one should see this terminology in a relative sense and also have specific quantities for comparison in mind. For instance the hydrodynamic quantities we computed suggest that this is very similar to the model of short-ranged interactions. Moreover, one of the conventional definitions of short-ranged models is one where force falls off quicker than r^{-d}, where d is the dimension which is certainly satisfied by the Calogero family.

Hamiltonian is given by[40, 43, 83]

$$H = -\frac{1}{2}\sum_{i=1}^{N}\frac{\partial^2}{\partial x_i^2} + \frac{1}{2}\sum_{i\neq j}\frac{\lambda(\lambda - P_{ij})}{(x_i - x_j)^2} + \frac{1}{2}\sum_{i=1}^{N} x_i^2. \tag{4.1}$$

Here and throughout the chapter we take the mass of particles as unity and measure distances in units of an oscillator length $l = \sqrt{\hbar/m\omega}$ and energy in units of $\hbar\omega$. The operator P_{ij} exchanges the positions of particles i and j[40]. The coupling parameter λ is positive and N is the total number of particles. The last term in (4.1) is the harmonic trap potential. It prevents particles from escaping to infinity and corresponds to effective optical potentials used in experiments to keep particles. The above model (4.1) was shown to be integrable[84]. The fully nonlinear hydrodynamics for the above model (4.1) without an external trap has been investigated in Ref. [15].

The chapter is organized as follows. In Sec. 4.2 we present the collective description of the microscopic model (4.1) in terms of collective fields and write equations of motion for these fields. Then we obtain static solutions: density and spin density profiles in Sec. 4.3. We consider the dependence of these equilibrium profiles on coupling and find it to be very similar to the recent predictions of Ma and Yang[2] for the model of fermions with contact interaction in a harmonic trap. In Sec. 4.4 we show how hydrodynamic fields evolve when the system is perturbed from the equilibrium configuration. We model an initial non-equilibrium profile as the one obtained by cooling the gas with an additional potential, i.e., keeping what is commonly referred to in literature[9] as a "knife" - in place (for examples of experiments involving "knife" see Refs [75] and [9]). In this section (4.4) we solve the hydrodynamic equations of motion exactly. These equations written for dressed Fermi momenta are reduced to forced Riemann-Hopf equations. The solutions of these equations have a very simple form. It turns out that in the phase-space picture solutions are given just by a rotation by an angle t (ωt in physical units) similar to a classical harmonic oscillator. We also study the density dynamics and see how an initial density perturbation evolves. The exact solution of the forced Riemann-Hopf equation is presented in Appendix E for the reader's convenience.

4.2 Collective Field theory

In this section we summarize the main results of the collective field theory for the sCM[15, 54, 55] following notations of Ref. [15]. We also include an external harmonic potential which is done in a straightforward way. The microscopic Hamiltonian (4.1) is rewritten in terms of hydrodynamic fields: the density of particles with spin up/down $\rho_{1,2}$ and their respective velocity fields $v_{1,2}$. Although, it is possible to study the exact quantum hydrodynamics of sCM[54, 55], in this chapter we neglect hydrodynamic terms with higher order of spatial gradients (gradientless approximation) and treat the equations of motion classically following Ref. [15]. This description is referred to as a gradientless hydrodynamics and is applicable for sufficiently smooth and slowly evolving field configurations, where terms with derivatives of fields can be neglected. A fully nonlinear gradientless hydrodynamics can describe nonlinear phenomena missed in conventional linear bosonization approach. In Ref. [15], this theory was used to study the non-linear coupling between the spin and charge degrees of freedom. [2] In Ref. [69] the Emptiness Formation probability (a particular n-point correlation function) was calculated using instanton approach to the collective field theory of sCM.

The collective field theory for sCM in the gradientless approximation is remarkably simple and allows for separation of variables in terms of dressed Fermi momenta[15]. Densities and velocities are expressed as linear combinations of dressed Fermi momenta.

The aim of this chapter is to extend this field theory by including an external potential, in particular, a harmonic potential. We find analytic solutions for both static profiles and dynamics of charge and spin densities of sCM in the presence of harmonic trap. The non-equilibrium initial configuration is realized by cooling the gas with an appropriate knife in place and then suddenly removing the knife as done in experiments (details are in Sec. 4.3 and Sec. 4.4). For simplicity, we focus here on a particular hydrodynamics sector of the model, i.e., we assume that the following inequality is valid at any time everywhere in space

$$|v_1 - v_2| < \pi(\rho_1 - \rho_2). \tag{4.2}$$

[2] The sCM is a very special model and it does not exhibit true spin-charge separation even in the linear approximation. In sCM the spin and charge velocities are the same.

In addition, we assume throughout this chapter that "1" labels the majority spin, i.e., $M_1 > M_2$, where $M_{1,2}$ is the total number of particles with spin 1 and spin 2 respectively, i.e.,

$$M_{1,2} = \int_{-\infty}^{+\infty} \rho_{1,2}\, dx. \tag{4.3}$$

We introduce particular linear combinations of these fields

$$k_{R1,L1} = v_1 \pm (\lambda+1)\pi\rho_1 \pm \lambda\pi\rho_2, \tag{4.4}$$

$$k_{R2,L2} = (\lambda+1)v_2 - \lambda v_1 \pm (2\lambda+1)\pi\rho_2, \tag{4.5}$$

referring to $k_{R,L;1,2}$ as to dressed Fermi momenta (see Ref. [15] for details). For future convenience we invert (4.4,5.12) to get

$$\rho_1 = \frac{(k_{R1}-k_{L1})}{2\pi(\lambda+1)} - \frac{\lambda(k_{R2}-k_{L2})}{2\pi(\lambda+1)(2\lambda+1)}, \tag{4.6}$$

$$v_1 = \frac{k_{L1}+k_{R1}}{2}, \tag{4.7}$$

$$\rho_2 = \frac{k_{R2}-k_{L2}}{2\pi(2\lambda+1)}, \tag{4.8}$$

$$v_2 = \frac{k_{L2}+k_{R2}+\lambda(k_{L1}+k_{R1})}{2(\lambda+1)}. \tag{4.9}$$

In terms of dressed momenta in the sector (4.2) the hydrodynamic Hamiltonian in harmonic trap in the gradientless approximation takes the form

$$\begin{aligned} H &= \frac{1}{12\pi\,(\lambda+1)} \int_{-\infty}^{+\infty} \left\{ k_{R1}^3 - k_{L1}^3 + \frac{1}{2\lambda+1}\left(k_{R2}^3 - k_{L2}^3\right) \right\} dx \\ &+ \frac{1}{2}\int_{-\infty}^{+\infty} x^2 \left(\frac{k_{R1}-k_{L1}}{2\pi(\lambda+1)} + \frac{k_{R2}-k_{L2}}{2\pi(\lambda+1)(2\lambda+1)} \right) dx. \end{aligned} \tag{4.10}$$

The first term in (4.10) was derived in Ref. [15] and the second term is due to the presence of the external harmonic trap. Notice, that the second term in (4.10) can be written as $\int_{-\infty}^{+\infty} \frac{x^2}{2}\rho_c\, dx$ where $\rho_c = \rho_1 + \rho_2$ (4.6,4.8) and represents the effect of the harmonic potential.

The Poisson brackets between hydrodynamic fields are given by

$$\{\rho_\sigma(x), v_{\sigma'}(y)\} = \delta_{\sigma\sigma'}\delta'(x-y), \tag{4.11}$$

where $\sigma, \sigma' = 1, 2$ are spin labels.

Then (4.11) along with (4.4,5.12) give the following brackets for $k's$, (here α, β take values $R1$, $L1$, $R2$, $L2$)

$$\{k_\alpha(x), k_\beta(y)\} = 2\pi s_\alpha \delta_{\alpha\beta} \delta'(x-y) \tag{4.12}$$

with

$$s_{R1} = -s_{L1} = \lambda + 1, \tag{4.13}$$

$$s_{R2} = -s_{L2} = (\lambda+1)(2\lambda+1). \tag{4.14}$$

The collective Hamiltonian (4.10) with Poisson brackets (4.12) generate equations of motion for fields $k_t = \{H, k\}$ which turn out to be the forced Riemann-Hopf equations. Namely, for any $k = k_{1R}$, k_{1L}, k_{2R}, k_{2L} we have

$$k_t + k k_x = -x. \tag{4.15}$$

For the case of a more general external potential $V(x)$ the right hand side of (4.15) should be replaced by $-\partial_x V$. One would expect to arrive at Riemann-Hopf equations [15] modified by a force term due to the external potential $V(x)$. It is remarkable, though, that the coupling constant λ does not enter (4.15) at all.

4.3 Static solutions

In this section we consider static density and velocity profiles of the sCM in a harmonic trap in the gradientless approximation. We give simple analytical expressions for these profiles for a system with an arbitrary spin polarization having a fixed number M_1 of spin-up and M_2 of spin-down particles. We describe static profiles in the form of phase-space diagrams. This description is very simple and gives a direct way to studying the dynamics of the sCM (see Sec. 4.4). Although these results are obtained for a particular 1D model with long range interaction (sCM) the static profiles look very similar to the ones recently obtained by Ma and Yang for a fermionic model with contact interaction in harmonic trap[2]. As mentioned earlier this similarity is, probably,

due to the fact that the potential $1/r^2$ can be considered in one dimension as relatively short ranged.

To obtain equilibrium (static) density and velocity profiles we assume no time dependence in (4.15) and obtain,

$$\partial_x(k^2 + x^2) = 0 \tag{4.16}$$

which is the equation of a "circle" in the phase space $(x - k)$ plane

$$k^2 + x^2 = \text{const.} \tag{4.17}$$

The constant in (4.17) depends on λ, M_1 and M_2 and can be easily determined using (4.6,4.8) along with (4.3). We find that the dressed-momenta for spin-up ($k_{R1,L1} \equiv k_1$) and spin-down ($k_{R2,L2} \equiv k_2$) particles satisfy the equations of two circles respectively.

$$k_1^2 + x^2 = 2(\lambda + 1)M_1 + 2\lambda M_2, \tag{4.18}$$

$$k_2^2 + x^2 = 2(2\lambda + 1)M_2. \tag{4.19}$$

The equation (4.18) defines a double-valued function $k_1(x)$. The positive value is identified with $k_{R1}(x)$ while the negative one gives $k_{L1}(x)$. The values of $k_{R2,L2}(x)$ are obtained in a similar manner from the second equation (4.19).

In order to write the expressions for charge-density ($\rho_c = \rho_1 + \rho_2$) and spin-density ($\rho_s = \rho_1 - \rho_2$) it is convenient to use a re-scaled coordinate η and re-scaled charge and spin densities $\tilde{\rho}_{c,s}$ given by

$$\eta = \frac{x}{\sqrt{(2\lambda + 1)\, N}}, \tag{4.20}$$

$$\tilde{\rho}_{c,s} = \sqrt{\frac{(2\lambda + 1)}{N}}\, \rho_{c,s}. \tag{4.21}$$

Here the total spin M, the total number of particles (charge) N and the

magnetization ν are defined respectively as

$$M = M_1 - M_2, \tag{4.22}$$

$$N = M_1 + M_2, \tag{4.23}$$

$$\nu = \frac{M}{N}. \tag{4.24}$$

From (4.22-C.24) we have

$$M_{1,2} = \frac{N}{2}(1 \pm \nu). \tag{4.25}$$

With these definitions we have from (4.18,4.19) and (4.6,4.8)

$$\tilde{\rho}_c = \frac{(2\lambda+1)}{\pi(\lambda+1)}\sqrt{1+\frac{\nu}{2\lambda+1}-\eta^2}+\frac{1}{\pi(\lambda+1)}\sqrt{1-\nu-\eta^2}, \tag{4.26}$$

$$\tilde{\rho}_s = \frac{(2\lambda+1)}{\pi(\lambda+1)}\left(\sqrt{1+\frac{\nu}{2\lambda+1}-\eta^2}-\sqrt{1-\nu-\eta^2}\right). \tag{4.27}$$

One could also notice as a cross-check that

$$\int_{-\infty}^{+\infty}\tilde{\rho}_c\,d\eta = \frac{1}{N}\int_{-\infty}^{+\infty}\rho_c\,dx = 1, \tag{4.28}$$

$$\int_{-\infty}^{+\infty}\tilde{\rho}_s\,d\eta = \frac{1}{N}\int_{-\infty}^{+\infty}\rho_s\,dx = \nu. \tag{4.29}$$

The analytical expressions for momenta (4.18,4.19) and the analytical expressions for the charge density (4.26) and the spin density (4.27) are the main results of this section. We see that in terms of phase space (Fig. 4.1) the system can be described by two circles of different radii. The radii depend on the coupling strength λ and the numbers of particles M_1 and M_2 as can be seen from (4.18,4.19). This is consistent with an exclusion statistics picture[15] so that the particle with spin up occupies the area $2\pi(\lambda+1)$ in the phase space while in the domain where both spin up and spin down particles are present the area is $2\pi(2\lambda+1)$ per 2 particles. In the limit $\lambda = 0$ (free fermions) the inner circle in Fig. 4.1 is filled with double density compared to the annulus region between the inner and outer circles. This is reflected as a bump feature for the charge density (see Fig. 4.2). In the limit of a very strong repulsion $\lambda \to +\infty$ the particles are mutually exclusive with the phase-space area ap-

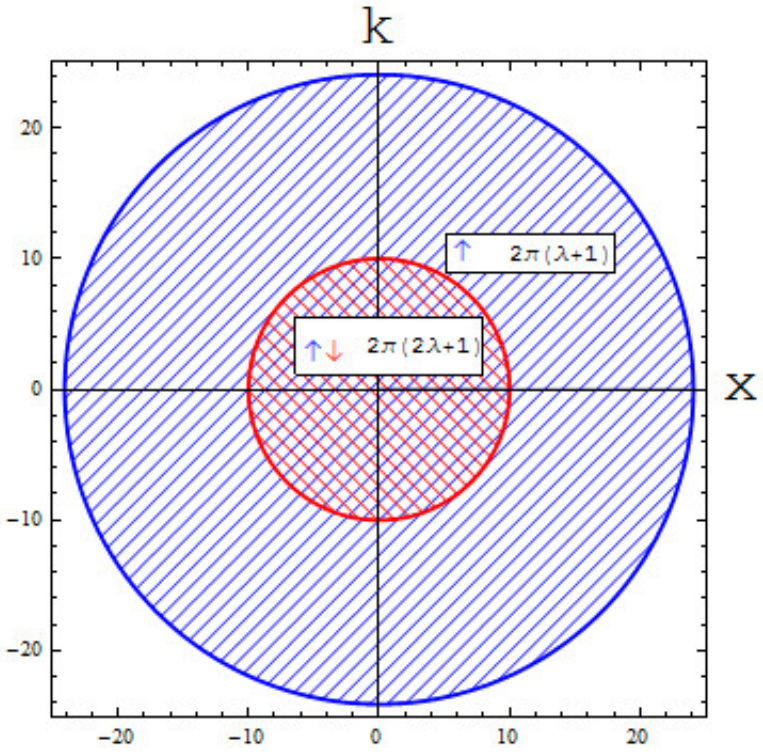

Figure 4.1: Phase-space picture for sCM with $\lambda = 2$ in equilibrium with an overall magnetization $\nu = 0.8$. The radii of circles are given by $\sqrt{N(2\lambda+1)(1-\nu)}$ and $\sqrt{N(2\lambda+1+\nu)}$ for inner and outer circles respectively. Particles fill the phase space uniformly with the density of two particles (up and down) per the area $2\pi(2\lambda+1)$ in the inner circle and of one particle (up) per the area $2\pi(\lambda+1)$ in the annulus area between inner and outer circles.

proximately $2\pi\lambda$ per particle and the charge density does not show any bump (see Fig. 4.2). For an arbitrary λ the bump feature interpolates between these two limits as shown in Fig. 4.2 with an explicit formula for the static charge density profile given in Eq. (4.26). We notice here that the size of the cloud $L_{cigar} = 2\sqrt{N(2\lambda + 1 + \nu)}$ given by the support of (4.26) grows with λ (1D gas expands when λ increases). We have taken this main dependence into account by plotting the density as a function of the re-scaled coordinate η.

It is interesting to note that although the bump in the charge density profile disappears in the limit of a very strong repulsion, the analogous feature in the spin-density profile is present for any λ. It is practically intact when plotted in terms of re-scaled variables (see Fig. 4.3) and is given explicitly by (4.27).

One should expect qualitatively similar profiles for the fermions with short range repulsion in a harmonic trap. Indeed, the physical origin of the bump feature is transparent for noninteracting fermions. It comes just from a superposition of densities of clouds of different size. We expect that the repulsive interaction smears out the bump feature making sure that the particles of different species avoid each other similarly to the Pauli exclusion of particles of the same species. Indeed, recent calculations of charge and spin density profiles for fermions with contact interactions by Ma and Yang [2] give results very similar (qualitatively) to the ones shown in Fig. 4.2 and Fig. 4.3.

The following comment is in order. As the origin of the bump feature in the equilibrium charge density profile can be traced to the model of non-interacting fermions, this feature is generic and should be observed also in three-dimensional harmonic traps which are widely used in cold atom experiments. Indeed, the superposition of two ellipsoid-like clouds of spin-up and spin-down particles will give the bump in the overall number density of atoms. The repulsive interaction will smear out the feature while the attractive one will amplify it.

To manipulate cold atom systems experimentally, additional external potentials are often used. The gas is cooled in the presence of a harmonic trap and an additional external potential. The latter is usually created by optical means and referred to as "knife". It is possible to create an external potential different for different particle species (spin up and spin down here). In the following we concentrate on the potential acting only on "charge" degrees of

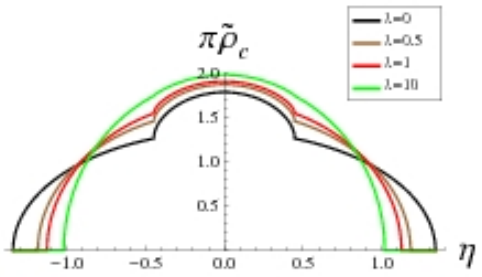

Figure 4.2: Equilibrium charge density profile for various values of coupling constant λ for fixed magnetization $\nu = 0.8$ is shown in re-scaled variables (4.20,4.21). $\lambda = 0$ corresponds to noninteracting fermions. Upon increasing the interaction strength λ the equilibrium profile eventually loses its bump feature. This prediction for the sCM is very similar to recent predictions of Ma and Yang for fermions with contact interaction[2].

freedom.

We choose a knife potential of the form $V_{knife} = -V_0 e^{-x^2/a^2}$. Then the static equation (4.16) is modified as

$$\partial_x \left(\frac{k^2}{2} + \frac{x^2}{2} + V_{knife} \right) = 0. \tag{4.30}$$

Due to the inclusion of the knife (4.30) the circles in phase-space acquire peaks (attractive knife $V_0 > 0$) or dips (repulsive knife $V_0 < 0$). There is also a peak or dip in the corresponding charge density profile. The knife shape, the corresponding phase-space and the charge density profiles are shown in Fig. 4.4. After using the knife to create an initial density profile with a peak (dip) one can remove the knife potential and study the evolution of density (or velocity) profiles as a function of time. The initial configuration is a non-equilibrium configuration. Its dynamics is governed by (4.15,4.4,5.12). We study the corresponding evolution in the next section Sec. 4.4.

4.4 Dynamics

Once the knife potential (Fig. 4.4) is suddenly removed we expect the system to evolve. In this section we study this dynamical behavior. Usually, the hydrodynamic equations are coupled partial differential equations. For the sCM in the gradientless approximation, it is possible to separate variables using

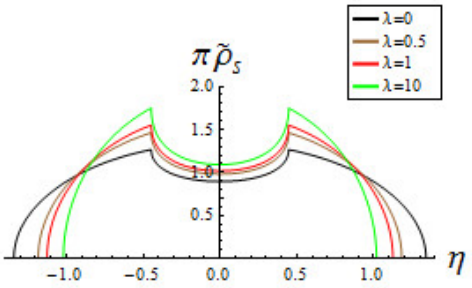

Figure 4.3: Equilibrium spin density profile for various values of coupling constant λ for the fixed magnetization $\nu = 0.8$. In re-scaled variables the dip in the spin density profile depends weakly on the interaction strength λ. Compare with the charge density profile of Fig. 4.2.

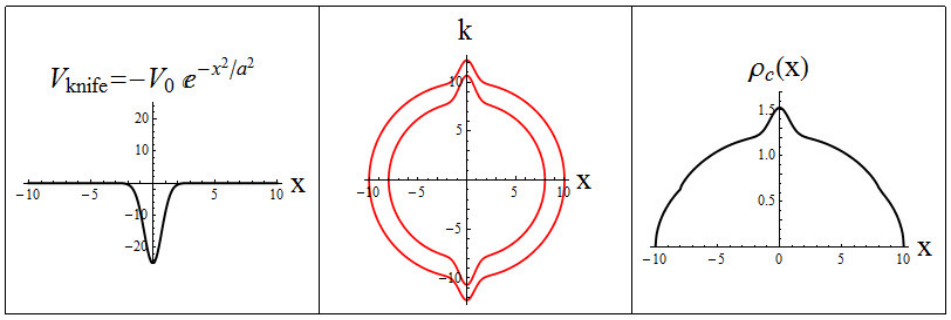

Figure 4.4: (left to right) a) Attractive knife potential in the presence of which the fermi gas is cooled. b) The distortion of phase space circles due to the knife. c) The corresponding charge density profile. The values of ν and λ are $\nu = 0.5$ and $\lambda = 2$.

dressed Fermi momenta instead of charge and spin densities and velocities [15]. The dressed momenta are related to hydrodynamic densities and velocities by (4.4,5.12) and satisfy the simple forced Riemann-Hopf equation (4.15). We reproduce it in this section for the reader's convenience.

$$k_t + kk_x = -x, \tag{4.31}$$

where $k = k_{1R}$, k_{1L}, k_{2R}, k_{2L}.

It is remarkable that the force term (right hand side) is the same for all dressed momenta. This is just another manifestation of the noninteracting nature of Calogero-type models (free particles with exclusion statistics). Of course, physical quantities of interest such as densities and velocities are some λ-dependent linear combinations of $k's$ (4.6,4.7,4.8,4.9) and hence do depend on the coupling strength λ.

As explained in Appendix E the forced Riemann-Hopf equation (4.31) can be easily solved in parametric form. Given an initial profile $k_0(x) = k(x, t = 0)$ (specifying the curve in a phase space picture) we can write a profile $k(x, t)$ at time t in a parametric form

$$x(s;t) = R(s)\sin\left[t + \alpha(s)\right], \tag{4.32}$$

$$k(s;t) = R(s)\cos\left[t + \alpha(s)\right]. \tag{4.33}$$

Here the parameter is s and the functions $R(s)$ and $\alpha(s)$ are determined by an initial profile $k_0(x)$ as

$$\alpha(s) = \tan^{-1}\left(\frac{s}{k_0(s)}\right), \tag{4.34}$$

$$R(s) = \sqrt{s^2 + k_0(s)^2} \tag{4.35}$$

consistent with (4.32,4.33) at $t = 0$.

We immediately notice that the evolution (4.32,4.33) is just a rotation of the curve $k(x)$ in the $x - k$ phase space with constant angular velocity 1 (ω in dimensionfull variables).

In this section we take the initial profile $k_0(x)$ as the one obtained as an equilibrium profile in phase space in the presence of the knife potential (Fig. 4.4b). When the knife is removed suddenly this profile serves as an

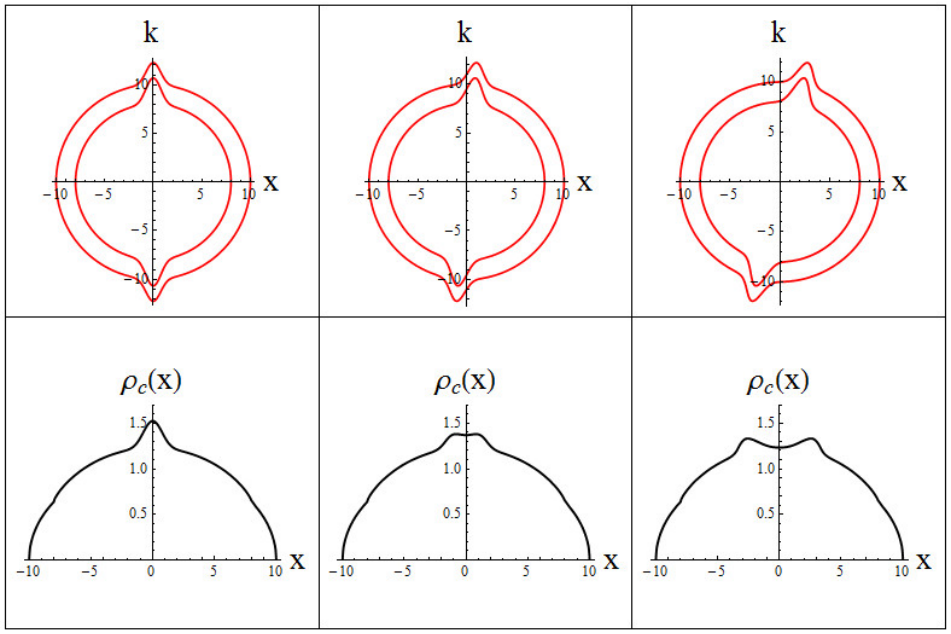

Figure 4.5: Top Row: (left to right) Evolution of phase space for time t=0,0.08 and 0.23 respectively. We see that this is merely a rotation by angle t. Bottow Row: Corresponding charge density evolution for times t=0,0.08,0.23. The additional peak created by the attractive knife flattens and eventually splits into two peaks. The values of ν and λ are $\nu = 0.5$ and $\lambda = 2$.

initial non-equilibrium profile. The time evolution in the phase-space is just a rotation of an initial profile by an angle $\theta = t$ as shown in Fig. 4.5. From the phase space picture at time t obtained by this rotation of an initial profile it is straightforward to compute the charge density evolution using (4.6-4.9) (and similarly for spin and velocities evolutions).

The top row of Fig. 4.5 shows the phase space rotation at various times. The bottom row is the extracted charge density. Since we are dealing with a gradientless theory, we can study the profile evolution only at times for which the field profiles are smooth. This gradientless approximation is commonly employed in studying nonlinear equations [56] and allows to study the evolution for a finite time when the nonlinear terms dominate over the terms with higher order in spatial gradients (dispersive terms). Of course, this is possible only if an initial profile is sufficiently smooth. For longer times, the solution inevitably evolves towards configurations with large field gradients (such as shock waves[73, 74]) and the gradientless approximation becomes inapplica-

ble. Choosing a sufficiently broad profile of the knife potential we make sure that during the initial stage of the evolution, corrections due to gradient terms in equations of motion are small. We emphasize that this evolution obtained in the gradientless approximation already shows some interesting features.

We see that the central peak (created by cooling with attractive knife) in the charge density profile slowly flattens and eventually splits into two peaks (see the bottom row of Fig. 4.5). Due to nonlinear effects these two split peaks start to steepen and we expect that at that point, gradient corrections will play a role and the profile would develop dispersive shock waves.

Although the solution of (4.31) is not well defined beyond some time (gradient catastrophe time) the parametric solution (4.32,4.33) can be formally extended beyond that time and produces multiply-valued solutions. These multiply-valued solutions should not be used as the equation (4.31) has corrections with higher power of gradients which will significantly change the solution beyond the gradient catastrophe time. It is interesting however that in time $t = 2\pi$ the solution should reproduce an initial profile and this is an exact feature of the spin-Calogero model. Of course, any corrections to the sCM model destroying integrability will lead to equilibration of the system and the time-periodicity will be lost. Probing the charge dynamics in Fermi gases at large times is indeed possible experimentally[9] and it would be interesting to see this equilibration experimentally.

Another interesting perturbation is the sudden shift of the minimum of an external harmonic potential. This is a standard technique for determining trap frequencies in cold atom experiments. The dynamics of the system after this sudden shift can be easily understood within the present formalism. Indeed the dynamics is just a rotation of the curve $k(x)$ in the $x - k$ phase space with constant angular velocity. Thus, we obtain the centre-of-mass oscillation with oscillation frequency ω. Notice that such a study is not trivial without the phase-space picture, thereby, highlighting the use of the phase-space description.

While our analytical expressions (4.32-4.33) are correct for free fermions and the sCM (long ranged interactions) we expect qualitatively similar dynamics at small times for systems with short range interaction. The corresponding dynamics studies for fermions with contact interaction (short ranged) could

be an interesting extension to the recent work of Ma and Yang[2]. To the best of our knowledge there are no such nonlinear dynamic studies for fermions with contact interaction in external harmonic trap. However, recently very similar qualitative features of nonlinearity have been observed in the spin and charge density dynamics of the Fermi-Hubbard model[82]. We would also like to remark that although our predictions for dynamics are for pure 1D systems we do expect a qualitatively similar behavior for the more familiar quasi 1D (cigars) experimental setups[9–11]. Indeed, using nonlinear hydrodynamic approach we found quantitative agreement with recent experiments on quasi 1D unitary Fermi-gas[1].

4.5 Conclusions

In this chapter we addressed statics and dynamics of a model of one-dimensional spin 1/2 fermions interacting through a long range inverse square interaction in an external harmonic trap (4.1). While one-dimensional systems with long range interactions are yet to be realized there has been a great progress in experimental studies[9–11] of quasi-one-dimensional fermionic models with contact-like interactions in an external harmonic trap.

Inclusion of an external harmonic trap potential is known to break the integrability of most models (for example models of bosons or fermions with delta interaction). On the contrary, the sCM (4.1) remains integrable even in the presence of an external harmonic potential [84]. Similarly, the collective field theory of sCM with harmonic trap retains a rather simple structure with dynamics analogous to the one of non-interacting fermions in a harmonic potential. In this chapter we used the spin-Calogero model as a toy model of more realistic systems of cold Fermi atoms in quasi-one-dimensional harmonic traps.

Using the collective field theory reviewed in Sec. 4.2 we studied static density profiles in Sec. 4.3 as well as dynamics of the model (see Sec. 4.4).

The obtained static solutions are found to be qualitatively similar to the static solutions for fermions with contact interaction in harmonic trap[2]. This similarity with short range interactions, probably, can be attributed to low-dimensionality where $1/r^2$ can be considered as relatively short ranged. The

obtained density profiles are given in (4.26,4.27) and are shown in Figures 4.1, 4.2 and 4.3. The solution of a similar problem for fermions with contact interactions requires numerical solution of Bethe Ansatz equations in combination with the Thomas-Fermi approximation[2]. An interesting feature of an equilibrium solution is the "bump" in the charge density profile present for a system with non-zero polarization. The reason for this feature is relatively straightforward as it is already present in the system of non-interacting fermions. It is interesting, however, that the smearing of this bump with an increase of the interaction is qualitatively very similar for both fermions with contact interaction[2] and for sCM model (Fig. 4.2). We also notice that while the bump feature in charge density (Fig. 4.2) eventually disappears at strong coupling the spin density profile remains robust (Fig. 4.3). This spin density profile is qualitatively similar to that for the contact interaction model considered in Ref. [2].

To study the dynamics of the cold gas in harmonic trap we create an initial non-equilibrium density profile by "cooling" the gas in an additional attractive potential ("knife"). We choose the form of the attractive knife potential $V_{knife} = -V_0 e^{-x^2/a^2}$ similar to the one used in experiments[9]. When the knife is suddenly removed the density profile shown in Fig. 4.4 serves as an initial non-equilibrium profile which is expected to evolve in time. We show in Sec. 4.4 that the central peak in the charge density profile (created by the knife) slowly flattens/broadens and eventually splits into two peaks (see the bottom row of Fig. 4.5). Due to nonlinear effects these two split peaks start to steepen and we expect that at that point, gradient corrections will play a role and the profile would develop dispersive shock waves[73, 74].

In conclusion, we studied equilibrium configurations as well as dynamics of the spin-Calogero model in a harmonic trap. We argued that the model can serve as a toy model for cold Fermi atoms in one dimensional traps due to the relatively short range nature of an inverse square potential in one dimension. The integrability of spin-Calogero model is not destroyed by the presence of harmonic potential and simple analytic solutions of hydrodynamic equations of motion for this model in the gradientless approximation are readily available.

In this chapter and in chapter 3 we studied collective field theory and investigated several aspects of nonlinear hydrodynamics of this very special

integrable model. A hydrodynamic description also helps in computing certain correlation functions, such as the Emptiness Formation Probability (EFP) that measures the probability $P(R)$ that a region of length $2R$ is completely void of particles. In Chapter 5 we study the EFP in the spin-Calogero Model and Haldane-Shastry Model using their hydrodynamic description.

Chapter 5

Emptiness and Depletion Formation Probability in spin models with inverse square interaction

5.1 Introduction

One-dimensional integrable models have an important role in the study of strongly correlated systems. When the reduced dimensionality makes interaction unavoidable, perturbative techniques can quickly loose applicability and over the years more sophisticated tools have been developed to tackle these problems. These tools clearly involve certain approximations and the existence of an exact solution for some models can allow to check their validity.

The conventional approach in solving quantum integrable model is known as the Bethe Ansatz (and its generalization). It is very successful in constructing the thermodynamics of a system, but not very suitable to study its dynamics and the correlation functions, due to the increasing complexity of its solutions. However, a very elegant formalism was developed using the Quantum Inverse Scattering Method (QISM) [86] to express correlation functions as determinants of certain integral operators (Fredholm determinants). In this formalism, the simplest correlation function one can write is known as the *Emptiness Formation Probability* (EFP) and measures the probability

$P(R)$ that a region of length $2R$ is completely void of particles. For lattice models, one is interested in $P(n)$, the probability that n consecutive lattice sites are empty. In a spin chain, taking advantage of the Jordan-Wigner mapping between particles and spins, the same quantity can be thought of as the *Probability of Formation of Ferromagnetic Strings* (PFFS), i.e. the probability that n consecutive spins are aligned in the same direction.

One should notice that the EFP is an n-point correlator and is, therefore, a much more complicated object compared to the usual two-point correlation functions one normally studies in condensed matter physics. However, due to the strongly interacting nature of the 1-D model, the QISM tells us that it is in fact no worse than other correlators between two points a length n apart and even somewhat simpler and more natural. Moreover, the EFP is one of those extended objects like the Von Neumann Entropy, or the Renyi Entropy, that in recent years have attracted a lot of interest because of their ability to capture global properties that were not observed before from the study of 2-point correlation functions. The latter quantities are of course motivated by studies of entanglement and quantum computation, while the EFP arises naturally in the contest of integrable theories.

Despite the claimed simplicity, the calculation of the EFP is by no means an easy task. For some models, the specific structure of the solution has allowed to find the asymptotic behavior of the EFP as $n \to \infty$. For instance, the EFP in the whole of the phase-diagram of the XY model was calculated in [65, 87–89] using the theory of Toeplitz determinants, while for the critical phase of the XXZ spin chain the solution was found in [90–92] using a multiple-integral representation. The EFP has been considered also for the 6-vertex model [93–95], for higher spins XXZ [96] and for dimer models [97]. We also remark that high temperature expansions of the EFP for Heisenberg chains have been studied in [98–100]. A recent review of the EFP can be found in [88] or [65].

Field theory approaches are normally most suited for the calculation of large distance asymptotics of correlation functions, but conventional techniques like those inspired by the Luttinger Liquid paradigm (i.e. bosonization) are not appropriate for extended objects like the EFP and only capture its qualitative behavior, while being quantitatively unreliable, as it was shown in [101]. The reason for this failure is that Luttinger Liquid theory is applica-

ble only to low-energy excitations around the Fermi points, where the linear spectrum approximation is valid, while correlators like the EFP involve degrees of freedom very deep in the Fermi sea, where the whole spectrum with its curvature is important.

For this reason, the field theory calculation of the EFP requires a non-linear generalization of conventional bosonization, i.e. a true hydrodynamic description of the system. In [65] it was shown that, with such a non-linear collective description available, the calculation of the EFP is possible by employing, for instance, an instanton approach.

In this chapter, we will extend the machinery developed in [65] and apply it to the spin-Calogero Model (sCM), for which a (gradientless) hydrodynamic description was recently constructed from its Bethe Ansatz solution [15]. The sCM is the spin$-1/2$ generalization [40–42] of the well-known Calogero-Sutherland model [43] and is defined by the Hamiltonian

$$H = -\frac{\hbar^2}{2}\sum_{j=1}^{N}\frac{\partial^2}{\partial x_j^2} + \frac{\hbar^2}{2}\left(\frac{\pi}{L}\right)^2\sum_{j\neq l}\frac{\lambda(\lambda-\mathbf{P}_{jl})}{\sin^2\frac{\pi}{L}(x_j-x_l)}\,, \tag{5.1}$$

where $\mathbf{P}_{jl}$ is the operator that exchanges the positions of particles j and l. We chose to analyze this Hamiltonian assuming it acts on fermionic particles, which means that the exchange term selects an anti-ferromagnetic ground state [15]. The coupling parameter λ is taken to be positive and N is the total number of particles.

In Ref. [15], a collective description of the model was derived using four hydrodynamic fields: the density of particles with spin up/down $\rho_{\uparrow,\downarrow}$ and their velocities $v_{\uparrow,\downarrow}$. The Hamiltonian in terms of these fields is valid only for slowly evolving configurations, where terms with derivatives of the density fields can be neglected. This description is referred to as a *gradientless hydrodynamics*. In Ref. [15], this theory was used to show the non-linear coupling between the spin and charge degrees of freedom beyond the Luttinger Liquid paradigm and it was shown that, while a charge excitation can evolve without affecting the spin sector (for instance for a spin singlet configuration), a spin excitation carries also some charge with it, in a non-trivial way.

The EFP for the sCM has not been considered in the literature yet. For the splinless case of the Calogero-Sutherland interaction, the asymptotic behavior

of the EFP was obtained using the form of the ground state wavefunction and thermodynamical arguments [102] (see [65, 88] for details). It should be noted that for certain special values of the coupling parameter λ, the splinless theory is tightly linked with Random Matrix Theory (RMT) and the EFP is the probability of having no energy eigenvalues in a given interval. For these values of λ the EFP can be calculated with much greater accuracy due to the additional structure provided by RMT [103, 104].

If we write the ground state of the system as $\Psi_G(x_1, x_2, \ldots, x_N)$, the Emptiness Formation Probability is defined as

$$P(R) \equiv \frac{1}{\langle \Psi_G | \Psi_G \rangle} \int_{|x_j|>R} \mathrm{d}x_1 \ldots \mathrm{d}x_N \, |\Psi_G(x_1, \ldots, x_N)|^2 \ , \tag{5.2}$$

or, following [86]

$$P(R) = \lim_{\alpha \to \infty} \langle \Psi_G | \mathrm{e}^{-\alpha \int_{-R}^{R} \rho_c(x) \mathrm{d}x} | \Psi_G \rangle \ , \tag{5.3}$$

where $\rho_c(x)$ is the total particle density operator

$$\rho_c(x) \equiv \sum_{j=1}^{N} \delta(x - x_j) \ . \tag{5.4}$$

For a model like the sCM, we can also introduce the EFPs for particles with spin up or down separately

$$P_{\uparrow,\downarrow}(R) = \lim_{\alpha \to \infty} \langle \Psi_G | \mathrm{e}^{-\alpha \int_{-R}^{R} \rho_{\uparrow,\downarrow}(x) \mathrm{d}x} | \Psi_G \rangle \ , \tag{5.5}$$

which will allow us to discuss the EFP as well as the PFFS.

The approach we use to calculate the EFPs (5.5) in this work is similar to what was explained in [65]. The idea is to consider the system as a quantum fluid evolving in imaginary time (Euclidean space). Then the EFP can be considered as the probability of a rare fluctuation that will deplete the region $-R < x < R$ of particle at a given imaginary time (say $\tau = 0$). With exponential accuracy, the leading contribution to this probability comes from the action calculated on the saddle point solution (instanton) satisfying the EFP boundary condition.

In section 5.2 we will first review the results of [15] and transform them into

an intriguing form where the dynamics can be decoupled into two independent fluids of splinless Calogero-Sutherland particles. This two-fluid description is one of the interesting observations of this chapter. In section 5.3 we will explain the instanton approach and formulate the problem in this language. In section 5.4 we will concentrate on a generalization of the EFP, the Depletion Formation Probability (DFP) which was introduced in [101]. This correlator will allow us to calculate the different EFPs very efficiently by taking its different limits in section 5.5. Most noticeably, we will derive the PFFS for the Haldane-Shastry model as the freezing limit of the sCM. In section 5.6 and 5.7 we will consider two additional DFP problems. Instead of specifying boundary conditions for both the spin and charge sectors of the fluid as we did in the previous sections, we will now relax these conditions and constrain only one component at a time: this analysis suggests that an effective spin-charge separation can be conjectured for the EFP/DFP of the sCM. In section 5.8 we combine all these results and suggest a physical interpretation of them. The final section contains some concluding remarks. To avoid interruptions in the exposition, certain technical formalities are moved to the appendices and are organized as follows. In appendix F we will revise and adapt the calculation of [65] to calculate the instanton action for our cases. In appendix G we will repeat this calculation in the linearized hydrodynamics approximation or bosonization, to aid the discussions in section 5.8.

5.2 Two-fluid description

In [15] the gradientless hydrodynamic description for the sCM (5.1) was derived in terms of densities and velocities of spin up and down particles: $\rho_{\uparrow,\downarrow}(t,x)$, $v_{\uparrow,\downarrow}(t,x)$. Here, we prefer to use densities and velocities of the *majority* and *minority* spin: $\rho_{1,2}(t,x), v_{1,2}(t,x)$, i.e. the subscript 1 (2) takes the value $\uparrow$ or $\downarrow$ which ever is most (least) abundant species:

$$\rho_1 \equiv \frac{\rho_\uparrow + \rho_\downarrow + |\rho_\uparrow - \rho_\downarrow|}{2} = \frac{\rho_c + \rho_s}{2} , \tag{5.6}$$

$$\rho_2 \equiv \frac{\rho_\uparrow + \rho_\downarrow - |\rho_\uparrow - \rho_\downarrow|}{2} = \frac{\rho_c - \rho_s}{2} , \tag{5.7}$$

where we introduced the charge and spin density

$$\begin{aligned} \rho_c(t,x) &= \rho_\uparrow + \rho_\downarrow = \rho_1 + \rho_2 \ , & (5.8) \\ \rho_s(t,x) &= |\rho_\uparrow - \rho_\downarrow| = \rho_1 - \rho_2 \ . & (5.9) \end{aligned}$$

Please note that whatever species is majority or minority is decided dynamically in each point in space and time.

Under the condition [15]

$$|v_1 - v_2| < \pi\rho_s \ , \tag{5.10}$$

the Hamiltonian is

$$H = \frac{1}{12\pi\,(\lambda+1)} \int_{-\infty}^{+\infty} \mathrm{d}x \left\{ k_{R1}^3 - k_{L1}^3 + \frac{1}{2\lambda+1} \left(k_{R2}^3 - k_{L2}^3 \right) \right\} \ , \tag{5.11}$$

where

$$\begin{aligned} k_{R1,L1} &\equiv v_1 \pm (\lambda+1)\pi\rho_1 \pm \lambda\pi\rho_2 \ , \\ k_{R2,L2} &= (\lambda+1)v_2 - \lambda v_1 \pm (2\lambda+1)\pi\rho_2 & (5.12) \end{aligned}$$

are the four *dressed Fermi momenta*.

It turns out that an auxiliary set of hydrodynamic variables decouples the Hamiltonian (5.11) into the sum of two independent splinless Calogero-Sutherland fluids a and b:

$$H = H_a + H_b = \sum_{\alpha=a,b} \int \mathrm{d}x \left[\frac{1}{2}\rho_\alpha v_\alpha^2 + \frac{\pi^2\lambda_\alpha^2}{6}\rho_\alpha^3 \right] \ , \tag{5.13}$$

where

$$\rho_a \equiv \frac{k_{R1}-k_{L1}}{2\pi\lambda_a} = \rho_1 + \frac{\lambda}{\lambda+1}\rho_2 \ , \tag{5.14}$$

$$\rho_b \equiv \frac{k_{R2}-k_{L2}}{2\pi\lambda_b} = \frac{1}{\lambda+1}\rho_2 \ , \tag{5.15}$$

$$v_a \equiv \frac{k_{R1}+k_{L1}}{2} = v_1 \ , \tag{5.16}$$

$$v_b \equiv \frac{k_{R2}+k_{L2}}{2} = (\lambda+1)\, v_2 - \lambda v_1 \ , \tag{5.17}$$

$$\lambda_a \equiv \lambda + 1 \ , \tag{5.18}$$

$$\lambda_b \equiv (\lambda+1)\,(2\lambda+1) \ . \tag{5.19}$$

We remark that both the auxiliary variables and the real variables satisfy the canonical commutation relations, i.e.

$$[\rho_\alpha(x), v_\beta(y)] = -\mathrm{i}\hbar\delta_{\alpha,\beta}\delta'(x-y) \ , \qquad \alpha,\beta = \{1,2\};\{a,b\} \ . \tag{5.20}$$

The form of the Hamiltonian (5.13) is one of the interesting observations of this chapter, since it allows us to reduce the spin Calogero-Sutherland model into a sum of two splinless theories. Each of the terms in square brackets in (5.13) is the gradientless Hamiltonian of a splinless CS system with coupling constants $\lambda_{a,b}$ given by (5.18, 5.19). In [65] the gradientless hydrodynamics of splinless particles, like the ones in (5.13) was used to calculate the EFP from the asymptotics of an instanton solution. In the next section we review this approach and we leave the mathematical details to appendix F.

5.3 The instantonic action

Let us perform a Wick's rotation to work in imaginary time $\tau \equiv \mathrm{i}t$. Note that this makes the velocities in (5.12) imaginary ($v \to \mathrm{i}v$) and the k's complex numbers. The $x-t$ plane is mapped into the complex plane spanned by $z \equiv x + \mathrm{i}\tau$.

Following [65], we will calculate the EFP as an instanton configuration (i.e. a classical solution in Euclidean space) that satisfies the boundary condition

$$\rho_\alpha(\tau = 0; -R < x < R) = 0 \ , \qquad \alpha = 1,2,c \ , \tag{5.21}$$

in the limit $R \to \infty$, i.e. R much bigger than any other length scale in the system. This limit guarantees that the gradient-less hydrodynamics (5.13) is valid in the bulk of the space-time. Once we have the classical solution of the equation of motion $\phi_{\rm EFP}$ that satisfies (5.21), a saddle-point calculation gives the EFP with exponential accuracy as the action $\mathcal{S}$ calculated on this optimal configuration [65]:

$$P(R) \simeq \mathrm{e}^{-\mathcal{S}[\phi_{\rm EFP}]} \ . \tag{5.22}$$

Of course, to uniquely specify the problem, the boundary conditions at infinity have to be provided as well and we will take them to be those of an equilibrium configuration:

$$\begin{aligned} &\rho_1(\tau,x) \overset{x,\tau\to\infty}{\to} \rho_{01} \ , \qquad && v_1(\tau,x) \overset{x,\tau\to\infty}{\to} 0 \ , \\ &\rho_2(\tau,x) \overset{x,\tau\to\infty}{\to} \rho_{02} \ , \qquad && v_2(\tau,x) \overset{x,\tau\to\infty}{\to} 0 \ . \end{aligned} \tag{5.23}$$

When $\rho_{01} = \rho_{02}$ we have an asymptotic singlet state (the AFM in zero magnetic field). The condition $\rho_{01} \neq \rho_{02}$ can be achieved via a constant external magnetic field which would result in a finite equilibrium magnetization. It is easy to implement these boundary conditions in our two-fluid description using (5.14-5.17).

The key point for the calculation is that we can represent the hydrodynamic fields in terms of the dressed Fermi momenta k_{R1}, k_{R2} (which in Euclidean space become complex and complex conjugated to k_{L1}, k_{L2} respectively) through (5.12):

$$k_{R1} = \lambda_a \pi \rho_a + \mathrm{i} v_a \ , \qquad k_{R2} = \lambda_b \pi \rho_b + \mathrm{i} v_b \ . \tag{5.24}$$

In [15], it was shown that these k-fields propagate independently according to 4 decoupled Riemann-Hopf equations

$$\partial_\tau w - \mathrm{i} w \partial_x w = 0 \ , \qquad w = k_{R,L;1,2} \ . \tag{5.25}$$

These equations have the general (implicit) solution

$$w = F(x + \mathrm{i} w \tau) \tag{5.26}$$

where $F(z)$ is an analytic function to be chosen to satisfy the boundary conditions.

Guided by [65], the solution for an EFP problem is

$$k_{R1} = F_a(x + \mathrm{i}k_{R1}\tau) \,, \qquad\qquad k_{R2} = F_b(x + \mathrm{i}k_{R2}\tau) \,, \tag{5.27}$$

with

$$F_a(z) \equiv \lambda_a \pi \rho_{0a} + \lambda_a \pi \eta_a \left(\frac{z}{\sqrt{z^2 - R^2}} - 1 \right) \,, \tag{5.28}$$

$$F_b(z) \equiv \lambda_b \pi \rho_{0b} + \lambda_b \pi \eta_b \left(\frac{z}{\sqrt{z^2 - R^2}} - 1 \right) \,, \tag{5.29}$$

which automatically satisfy the conditions at infinity (5.23):

$$\begin{aligned} \rho_a(\tau, x \to \infty) &\to \rho_{01} + \frac{\lambda}{\lambda + 1} \rho_{02} \equiv \rho_{0a} \,, \\ \rho_b(\tau, x \to \infty) &\to \frac{1}{\lambda + 1} \rho_{02} \,, \equiv \rho_{0b} \,, \\ v_{a,b}(\tau, x \to \infty) &\to 0 \,, \end{aligned} \tag{5.30}$$

while $\eta_{a,b}$ are two, possibly complex, constants that allow to satisfy the EFP boundary conditions (5.21).

In appendix F we show that the instanton action can be expressed as a contour integral where only the behaviors of the solutions (5.27) at infinity and close to the depletion region are needed, saving us the complication of solving the implicit equations in generality. Using the two-fluid description, the action can be written as the sum of two splinless Calogero-Sutherland fluids: from (F.23) we have

$$\mathcal{S}_{\mathrm{EFP}} = \frac{1}{2} \pi^2 R^2 \sum_{\alpha = a,b} \lambda_\alpha \, \eta_\alpha \, \bar{\eta}_\alpha \,. \tag{5.31}$$

Before we proceed further, we should mention that the two-fluid description we employ is valid as long as the inequality (5.10) is satisfied. In fact, the solution (5.27) could violate the inequality in a small region around the points $(\tau, x) = (0, \pm R)$. However, close to these points the hydrodynamic description is expected to be somewhat pathological, because gradient corrections (which

we neglect) become important. As it was argued in [65, 101], the contributions that would come to the EFP from these small regions are subleading and negligible, in the asymptotic limit $R \to \infty$ we consider. Therefore, we do not need to worry about what happens near the points $(\tau, x) = (0, \pm R)$. However, a consequence of the "singular" nature of these points is that, in our solution, the species that constitutes the majority (minority) spin in the region of depletion $-R < x < R$ at $\tau = 0$, could switch and become minority (majority) at infinity. This could be important to keep in mind in interpreting our formulae, but our formalism already takes that into account naturally.

5.4 Depletion Formation Probability

It is more convenient to consider a generalization of the EFP problem, called Depletion Formation Probability (DFP) which was introduced in [101]. In hydrodynamic language the DFP boundary conditions for the *majority* and *minority* spins are

$$\begin{aligned} \rho_1(\tau = 0; -R < x < R) &= \tilde{\rho}_1 \ , \\ \rho_2(\tau = 0; -R < x < R) &= \tilde{\rho}_2 \ . \end{aligned} \tag{5.32}$$

The DFP is a natural generalization of the EFP (5.21) and it reduces to it for $\tilde{\rho}_{1,2} = 0$. Of course, there is some ambiguity on the microscopic definition of the DFP (see [65, 101]). One can, for instance, consider it as the macroscopic version of the s-EFP introduced in [105]. We will first calculate the DFP as the most general case and later take the appropriate interesting limits.

In terms of the auxiliary fields we introduced in (5.14-5.17) to achieve the two-fluids description (5.13), the DFP boundary conditions are

$$\begin{aligned} \rho_a(\tau = 0, -R < x < R) &= \tilde{\rho}_1 + \frac{\lambda}{\lambda + 1}\tilde{\rho}_2 \equiv \tilde{\rho}_a \ , \\ \rho_b(\tau = 0, -R < x < R) &= \frac{1}{\lambda + 1}\tilde{\rho}_2 \equiv \tilde{\rho}_b \ . \end{aligned} \tag{5.33}$$

We specify the parameters $\eta_{1,2}$ in (5.28,5.29) by expressing the boundary

conditions (5.33) in terms of the dressed momenta using

$$\begin{aligned}
\rho_1 &= \frac{1}{\pi(\lambda+1)}\left[\mathrm{Re}\ k_{R1} - \frac{\lambda}{2\lambda+1}\,\mathrm{Re}\ k_{R2}\right] , \\
\rho_2 &= \frac{1}{\pi(2\lambda+1)}\,\mathrm{Re}\ k_{R2} , \\
v_1 &= \mathrm{Im}\ k_{R1} , \\
v_2 &= \frac{1}{\lambda+1}\Big[\mathrm{Im}\ k_{R2} + \lambda\,\mathrm{Im}\ k_{R1}\Big] .
\end{aligned} \tag{5.34}$$

This leads to

$$\begin{aligned}
\lambda_a\eta_a &= \lambda_a\left(\rho_{0a} - \tilde{\rho}_a\right) \\
&= (\lambda+1)(\rho_{01} - \tilde{\rho}_1) + \lambda(\rho_{02} - \tilde{\rho}_2) , \\
\lambda_b\eta_b &= \lambda_b\left(\rho_{0b} - \tilde{\rho}_b\right) \\
&= (2\lambda+1)\left(\rho_{02} - \tilde{\rho}_2\right) .
\end{aligned} \tag{5.35}$$

It is now straightforward to obtain the DFP by substituting (5.35) into (5.31). After some simple algebra we get

$$\begin{aligned}
P_{DFP}(R) &= \exp\left\{-\frac{\pi^2}{2}\left[\lambda\left(\rho_{0c} - \tilde{\rho}_c\right)^2 + \left(\rho_{01} - \tilde{\rho}_1\right)^2 + \left(\rho_{02} - \tilde{\rho}_2\right)^2\right] R^2\right\} \\
&= \exp\left\{-\frac{\pi^2}{2}\left[\left(\lambda + \frac{1}{2}\right)\left(\rho_{0c} - \tilde{\rho}_c\right)^2 + \frac{1}{2}\left(\rho_{0s} - \tilde{\rho}_s\right)^2\right] R^2\right\} ,
\end{aligned} \tag{5.36}$$

where we introduced a notation in terms of the charge field ($\rho_{0c} = \rho_{01} + \rho_{02}$, $\tilde{\rho}_c = \tilde{\rho}_1 + \tilde{\rho}_2$) and of the spin field ($\rho_{0s} = \rho_{01} - \rho_{02}$, $\tilde{\rho}_s = \tilde{\rho}_1 - \tilde{\rho}_2$). Equation (5.36) is the main result of this work. To understand it better, we will consider several interesting limits.

5.4.1 Asymptotic singlet state

If no external magnetic field is applied, the equilibrium configuration of an antiferromagnetic system like the one we consider is in a singlet state. This means that in the boundary conditions at infinity (5.23) we should set $\rho_{01} = \rho_{02} = \rho_0$.

In this limit (5.36) reduces to

$$\begin{aligned} P_{DFP}^{\text{singlet}}(R) &= \exp\left\{-\frac{\pi^2}{2}\left[\lambda\left(2\rho_0-\tilde{\rho}_c\right)^2+\left(\rho_0-\tilde{\rho}_1\right)^2+\left(\rho_0-\tilde{\rho}_2\right)^2\right]R^2\right\} \\ &= \exp\left\{-\frac{\pi^2}{2}\left[(\lambda+\frac{1}{2})\left(2\rho_0-\tilde{\rho}_c\right)^2+\frac{1}{2}\tilde{\rho}_s^2\right]R^2\right\}. \end{aligned} \tag{5.37}$$

5.5 Emptiness Formation Probability

By taking the limit $\tilde{\rho}_{1,2}=0$ we can use (5.36) to calculate the different EFPs. The probability to find the region $-R<x<R$ at $\tau=0$ completely empty of particles is therefore

$$\begin{aligned} P_{EFP}(R) &= \exp\left\{-\frac{\pi^2}{2}\left[\lambda\left(\rho_{01}+\rho_{02}\right)^2+\rho_{01}^2+\rho_{02}^2\right]R^2\right\} \\ &= \exp\left\{-\frac{\pi^2}{2}\left[(\lambda+\frac{1}{2})\rho_{0c}^2+\frac{1}{2}\rho_{0s}^2\right]R^2\right\}, \end{aligned} \tag{5.38}$$

which becomes

$$P_{EFP}^{\text{singlet}}(R)=\exp\left\{-\frac{\pi^2}{2}(\lambda+\frac{1}{2})(2\rho_0)^2R^2\right\} \tag{5.39}$$

for the asymptotic singlet state. This is equivalent to the EFP of a splinless Calogero-Sutherland system with coupling constant $\lambda'=\lambda+1/2$, see (5.43). This is consistent with the phase-space picture provided in [15], in which it is explained that for a singlet state each particle occupies an area of $\pi(\lambda+1/2)$ due to the exclusion statistics, while it would occupy an area $\pi(\lambda+1)$ if it were alone. Therefore, in this context, the charge field can be thought of as describing a splinless Calogero system with coupling constant $\lambda'=\lambda+1/2$.

5.5.1 Free fermions with spin

Setting the coupling parameter $\lambda = 0$ corresponds to non-interacting (free) fermions with spins and this reduces (5.36) to

$$\begin{aligned} P_{DFP}^{\text{free fermions}}(R) &= \exp\left\{ -\frac{1}{4}\left[\pi\left(\rho_{0c}-\tilde{\rho}_c\right)R\right]^2 - \frac{1}{4}\left[\pi\left(\rho_{0s}-\tilde{\rho}_s\right)R\right]^2 \right\} \\ &= \exp\left\{ -\frac{1}{2}\left[\pi\left(\rho_{01}-\tilde{\rho}_1\right)R\right]^2 - \frac{1}{2}\left[\pi\left(\rho_{02}-\tilde{\rho}_2\right)R\right]^2 \right\}. \end{aligned} \tag{5.40}$$

This result is the same as the one obtained in [65]. The EFP is then

$$P_{EFP}^{\text{free fermions}}(R) = \exp\left\{ -\frac{1}{2}\left(\pi\rho_{01}R\right)^2 - \frac{1}{2}\left(\pi\rho_{02}R\right)^2 \right\}, \tag{5.41}$$

which agrees with the results obtained in the context of Random Matrix Theory [102–104], where the subleading corrections were also found.

5.5.2 Splinless Calogero-Sutherland model

Of course, the prime check to our formula for the DFP/EFP of the sCM is to take its splinless limit $\tilde{\rho}_2 = \rho_{02} = 0$, which gives

$$P_{DFP}^{\text{splinless}}(R) = \exp\left\{ -\frac{(\lambda+1)}{2}\pi^2\left(\rho_{01}-\tilde{\rho}_1\right)^2 R^2 \right\}, \tag{5.42}$$

$$P_{EFP}^{\text{splinless}}(R) = \exp\left\{ -\frac{(\lambda+1)}{2}\pi^2\rho_{01}^2 R^2 \right\}, \tag{5.43}$$

in perfect agreement with [65, 102] for a splinless Calogero-Sutherland system with coupling $\lambda' = \lambda + 1$.

5.5.3 Probability of Formation of Ferromagnetic Strings

If we require the minority spin particles to completely empty the region $-R < x < R$ at $\tau = 0$, we are left only with the majority spin and we created a (partially) polarized state. We can refer to this case as the Probability

of Formation of Partially Ferromagnetic Strings (PFPFS) [65, 101]. Setting $\tilde{\rho}_2 = 0$ in (5.36) and leaving $\tilde{\rho}_1$ finite we have

$$P_{PFPFS}(R) = \exp\left\{ -\frac{\pi^2}{2} \left[\lambda \left(\rho_{01} - \tilde{\rho}_1 + \rho_{02} \right)^2 + \left(\rho_{01} - \tilde{\rho}_1 \right)^2 + \rho_{02}^2 \right] R^2 \right\} . \tag{5.44}$$

The above is the probability of formation of ferromagnetic strings accompanied by a partial depletion of particles, since in the region of depletion we have $\tilde{\rho}_c = \tilde{\rho}_1$. We can impose that the average density of particles is constant everywhere by setting $\tilde{\rho}_1 = \rho_{01} + \rho_{02} = \rho_{0c}$, while still requiring all particles in the region $-R < x < R$ at $\tau = 0$ to be completely polarized (maximal magnetization: PFFS)

$$P_{PFFS}(R) = \exp\left\{ - \left[\pi \rho_{02} R \right]^2 \right\} . \tag{5.45}$$

Note that (5.45) is independent of λ and exactly corresponds to the Emptiness Formation Probability of a $\lambda' = \lambda + 1 = 2$ splinless Calogero model with background density given by ρ_{02} (5.43). Interestingly the same result (5.52) will be derived in the next sections as the EFP of minority spins, i.e. $\tilde{\rho}_2 = 0$, in the Haldane-Shastry model (5.46). This is just another aspect of the well-known relation between spin-Calogero, Haldane-Shastry and $\lambda' = 2$ splinless Calogero models [15, 66] as it will be shown in the next section.

5.5.4 The freezing limit

If we take the $\lambda \to \infty$ limit in the spin-Calogero model (5.1), the charge dynamics freezes (the particles become pinned to a lattice) and only the spin dynamics survives. This *freezing limit* was shown by Polychronakos [57] to be equivalent to the Haldane-Shastry model (HSM) [66, 67]:

$$H_{\text{HSM}} = 2 \frac{\pi^2}{N^2} \sum_{j<l} \frac{S_j \cdot S_l}{\sin^2 \frac{\pi}{N} (j-l)} , \tag{5.46}$$

an integrable Heisenberg chain with long range interaction. In [15] the freezing limit was studied through a systematic expansion of the hydrodynamic fields

in inverse powers of $\mu \equiv \lambda + 1/2$:

$$\Omega = \Omega^{(0)} + \frac{1}{\mu}\Omega^{(1)} + \frac{1}{\mu^2}\Omega^{(2)} + \dots \ , \qquad \rho_c, v_c, \rho_s, v_s \to \Omega \ . \tag{5.47}$$

With an additional rescaling of time $t \to \mu t$, the equations of motion were separated order by order in powers of μ.

It was shown that the charge sector is frozen, in that charge dynamics appears only at orders $\mathrm{O}(\mu^{-1})$ and higher, while the spin sector already has non-trivial dynamics at order $\mathrm{O}(1)$. This dynamics is the same as the one derived independently for the HSM, over a background density of particles $\rho_{0c} = N/L$. As a consequence of charge freezing, this background density is kept fixed and constant up to order $\mathrm{O}(1)$ and fluctuations are suppressed as $1/\mu$. Therefore, as $\mu = \lambda + 1/2 \to \infty$, charge conservation is imposed dynamically everywhere, including in the region of depletion:

$$\tilde{\rho}_c^{(0)} = \tilde{\rho}_1^{(0)} + \tilde{\rho}_2^{(0)} = \rho_{01} + \rho_{02} = \rho_{0c} \ . \tag{5.48}$$

The above (5.48) along with the usual depletion boundary conditions (5.32) reduces (5.36) to

$$\begin{aligned} P_{DFP}^{\mu\to\infty}(R) &= \exp\left\{-\frac{\pi^2}{2}\left[\frac{1}{2}\left(\rho_{0s} - \tilde{\rho}_s^{(0)}\right)^2 + \frac{1}{\mu}\tilde{\rho}_c^{(1)} + \mathrm{O}(\mu^{-2})\right] R^2\right\} \qquad (5.49) \\ &\simeq \exp\left\{-\left[\pi\left(\rho_{01} - \tilde{\rho}_1^{(0)}\right) R\right]^2\right\} = \exp\left\{-\left[\pi\left(\rho_{02} - \tilde{\rho}_2^{(0)}\right) R\right]^2\right\} , \end{aligned}$$

where corrections for a finite λ are of the order $1/\mu$. Eq. (5.49) coincides with (5.45), where condition (5.48) was imposed as a boundary condition, and not dynamically from the equations of motion.

5.5.5 Haldane-Shastry model

The hydrodynamic description of the HSM (5.46) was constructed in [15], resulting in the following Hamiltonian for the minority spins (remember that the HSM is a lattice model and therefore there is no charge dynamics)

$$H_{\mathrm{HSM}} = \int \mathrm{d}x \left[\frac{1}{2}\,\rho_2\, v_2^2 + \frac{2}{3}\,\pi^2\,\rho_2^3\right] , \tag{5.50}$$

which is the hydrodynamic Hamiltonian for a splinless Calogero system with coupling constant $\lambda' = 2$, see (5.13). It is in fact known that the spectrum of the HSM is equivalent to that of a splinless Calogero-Sutherland model with exclusion parameter $\lambda' = 2$, but with a high degeneracy due to the underlying Yangian symmetry [66].

The connection between the HSM (D.13) and the sCM in the freezing limit is to express the minority spin fields in (D.13) in terms of spin fields [15]:

$$\rho_2 = \frac{\rho_{0c} - \rho_s}{2}\,, \qquad\qquad v_2 = -2v_s\,. \tag{5.51}$$

It is straightforward, using (5.42) with $\lambda' = 2$, to see that the PFPFS for the HSM model is exactly (5.49):

$$P^{HSM}_{PFPFS}(R) = \exp\Big\{ -\left[\pi\left(\rho_{02} - \tilde{\rho}_2\right) R\right]^2 \Big\}\,. \tag{5.52}$$

The equivalence between (5.45), (5.49) and (5.52) is a strong check of the consistency of our methods and shows from a novel perspective the well-known relations between the sCM in the large λ limit, the HSM and the splinless Calogero-Sutherland model with $\lambda' = 2$.

5.6 Spin Depletion Probability

So far, we considered a DFP problem specified by the boundary conditions (5.32), i.e. by fixing the density of both species of particles on the segment $\tau = 0$, $-R < x < R$. However, our formalism allows for a more general and natural question. We can, for instance, demand a given magnetization (i.e. spin density) on the segment, without constraining the charge sector, i.e. imposing the boundary condition:

$$\rho_s(\tau = 0; -R < x < R) = \tilde{\rho}_s\,, \tag{5.53}$$

instead of (5.32).

From (5.34) we have

$$\rho_s = \frac{1}{\pi(\lambda+1)} \mathrm{Re}\,\left[k_{R1} - k_{R2}\right]\,, \tag{5.54}$$

substituting in (5.27,5.28,5.29) we find that (5.53) is satisfied if

$$\lambda_a \eta_a - \lambda_b \eta_b = \lambda_a \rho_{0a} - \lambda_b \rho_{0b} - (\lambda + 1)\tilde{\rho}_s \ . \tag{5.55}$$

This equation leaves undetermined a complex constant $\xi = \xi_1 + \mathrm{i}\xi_2$: for later convenience we parametrize the solution as

$$\begin{aligned} \lambda_a \eta_a &= \lambda_a \rho_{0a} - \frac{1}{2}\tilde{\rho}_s - \left(\lambda + \frac{1}{2}\right)\xi \\ &= \left(\lambda + \frac{1}{2}\right)(\rho_{0c} - \xi) + \frac{1}{2}(\rho_{0s} - \tilde{\rho}_s) \ , \\ \lambda_b \eta_b &= \lambda_b \rho_{0b} + \left(\lambda + \frac{1}{2}\right)(\tilde{\rho}_s - \xi) \\ &= \left(\lambda + \frac{1}{2}\right)(\rho_{0c} - \xi - \rho_{0s} + \tilde{\rho}_s) \ . \end{aligned} \tag{5.56}$$

We have constructed the solution that realizes a constant spin density in the depletion region, while leaving the densities for the individual species free to vary. Please note that a finite imaginary part of ξ is necessary to have $\partial_x \rho_{1,2}(\tau = 0; -R < x < R) \neq 0$.

We can now substitute (5.56) in (5.31) to find:

$$P_{SDP}(R;\xi) = \exp\left\{-\frac{\pi^2}{2}\left[\left(\lambda + \frac{1}{2}\right)\left[(\rho_{0c} - \xi_1)^2 + \xi_2^2\right] + \frac{1}{2}(\rho_{0s} - \tilde{\rho}_s)^2\right] R^2\right\} . \tag{5.57}$$

This probability depends on two, yet undetermined, parameters: $\xi_{1,2}$. If we choose $\xi_1 = \tilde{\rho}_c$ and $\xi_2 = 0$ we recover exactly (5.36), as we expected. This would correspond to forcing a given charge density at the depletion region, together with (5.53).

We also note that the configuration that maximizes the probability (5.57) is given by $\xi = \rho_{0c}$:

$$P_{SDP}^{\mathrm{Max}}(R) = P_{SDP}(R; \xi = \rho_{0c}) = \exp\left\{-\frac{\pi^2}{4}(\rho_{0s} - \tilde{\rho}_s)^2 R^2\right\} . \tag{5.58}$$

One cannot help but noticing the similarity between (5.58) and (5.49) or (5.52).

Since the parametrization we choose in (5.56) allowed us to express the probability (5.57) as a Gaussian for $\xi_{1,2}$, we would get the same result by

performing an integral over the free parameters:

$$P_{SDP}^{\rm opt}(R) = \int_{-\infty}^{\infty} {\rm d}\xi_1 \int_{-\infty}^{\infty} {\rm d}\xi_2 \, P_{SDP}(R;\xi) = P_{SDP}^{\rm Max}(R). \tag{5.59}$$

where the prefactor coming from the Gaussian integration is beyond our accuracy anyway (note, however, that it does not depend on the charge density). The integration over ξ corresponds to summing over all configurations of the form (5.27, 5.28, 5.29).

The probability of realizing the magnetization set by (5.53) is given by a sum over all configurations that satisfy the given boundary conditions. To perform this sum correctly, we would need to consider all possible charge density profiles $\tilde{\rho}_c(x)$ at the depletion region and therefore consider more general solutions than (5.28, 5.29). These general solutions are of the form

$$\begin{aligned} F_a(z) &\equiv \pi \left[\lambda_a \rho_{0a} - \frac{1}{2}\tilde{\rho}_s\right] \frac{z}{\sqrt{z^2 - R^2}} + \frac{\pi}{2}\tilde{\rho}_s + \pi\left(\lambda + \frac{1}{2}\right)\xi(z) \, , \\ F_b(z) &\equiv \pi \left[\lambda_b \rho_{0b} + \left(\lambda + \frac{1}{2}\right)\tilde{\rho}_s\right] \frac{z}{\sqrt{z^2 - R^2}} + \pi\left(\lambda + \frac{1}{2}\right)\left[-\tilde{\rho}_s + \xi(z)\right] \, , \end{aligned} \tag{5.60}$$

where $\xi(z)$ is an analytic function such that ${\rm Re}\,\xi(x) = \tilde{\rho}_c(x)$ and $\xi(z \to \infty) \to 0$. The sum over all configurations satisfying (5.53) can be formulated as a functional integral over all functions $\xi(z)$. However, it is easy to convince oneself that the configurations that minimize the action are of the form (5.28, 5.29), with $\xi = \rho_{0c}$.

5.7 Charge Depletion Probability

The last problem we will address is conjugated to the one considered in the previous section, i.e. the probability of realizing a given depletion of the charge

$$\rho_c(\tau = 0; -R < x < R) = \tilde{\rho}_c \, , \tag{5.61}$$

without constraining the spin density. Using (5.34) we have

$$\rho_c = {\rm Re}\left[\frac{k_{R1}}{\pi\lambda_a} + \frac{k_{R2}}{\pi\lambda_b}\right] \, , \tag{5.62}$$

which means that (5.27,5.28,5.29) fulfill (5.61) if

$$\eta_a + \eta_b = \rho_{0a} + \rho_{0b} - \tilde{\rho}_c \ . \tag{5.63}$$

Once again, we are left with the freedom of introducing a complex number $\xi = \xi_1 + \mathrm{i}\xi_2$ to parametrize the solution:

$$\begin{aligned} \eta_a &= \rho_{0a} - \frac{2\lambda+1}{2(\lambda+1)}\tilde{\rho}_c - \frac{1}{2(\lambda+1)}\xi \\ &= \frac{2\lambda+1}{2(\lambda+1)}\left(\rho_{0c} - \tilde{\rho}_c\right) + \frac{1}{2(\lambda+1)}\left(\rho_{0s} - \xi\right) \ , \\ \eta_b &= \rho_{0b} - \frac{1}{2(\lambda+1)}\tilde{\rho}_c + \frac{1}{2(\lambda+1)}\xi \\ &= \frac{1}{2(\lambda+1)}\left(\rho_{0c} - \tilde{\rho}_c - \rho_{0s} + \xi\right) \ . \end{aligned} \tag{5.64}$$

Inserting this into (5.31) we obtain:

$$P_{CDP}(R;\xi) = \exp\left\{-\frac{\pi^2}{2}\left[\left(\lambda+\frac{1}{2}\right)\left(\rho_{0c} - \tilde{\rho}_c\right)^2 + \frac{1}{2}\left[\left(\rho_{0s} - \xi_1\right)^2 + \xi_2^2\right]\right]R^2\right\} . \tag{5.65}$$

Setting $\xi_1 = \tilde{\rho}_s$ and $\xi_2 = 0$ correctly reproduces (5.36), while the maximal probability is achieved for $\xi = \rho_{0s}$:

$$P^{\mathrm{Max}}_{CDP}(R) = P_{CDP}(R;\xi=\rho_{0s}) = \exp\left\{-\frac{\pi^2}{2}\left[\left(\lambda+\frac{1}{2}\right)\left(\rho_{0c} - \tilde{\rho}_c\right)^2\right]R^2\right\} . \tag{5.66}$$

As before, since (5.65) is Gaussian in $\xi_{1,2}$, we would obtain the same result by integrating over these variables

$$P^{\mathrm{opt}}_{CDP}(R) = \int_{-\infty}^{\infty}\mathrm{d}\xi_1\int_{-\infty}^{\infty}\mathrm{d}\xi_2\, P_{CDP}(R;\xi) = P^{\mathrm{Max}}_{CDP}(R) \ , \tag{5.67}$$

where we neglected the coefficient coming from the Gaussian integration because its beyond the accuracy of our methodology. This integration corresponds to summing over all configurations given by (5.28, 5.29). Again, we notice a striking similarity between (5.66, 5.67) and (5.36). We will comment in the next section on how to interpret these results.

5.8 Discussion of the results

Eq. (5.36) looks like the product of the two independent depletion probabilities for the spin and charge sector. This interpretation is supported by the results of the two previous sections, see (5.58) and (5.66), but it is quite surprising in a sense. In fact, it would indicate a sort of an effective spin-charge separation, as if the spin and charge degrees of freedom could be depleted independently. This is contrary to intuition, since spin-charge separation is realized only for low-energy excitations close to the Fermi points, while the EFP involves degrees of freedom deep within the Fermi sea (and requires a full non-linear hydrodynamic description beyond the usual bosonization approach). However, it seems that from a EFP perspective spin-charge separation survives beyond the linearization of the spectrum, at least at leading order for the sCM.

In fact, quite surprisingly, for the Calogero-type interaction (as well as for free fermions), the DFP result obtained for small depletions using a linearized hydrodynamics (conventional bosonization) can be extended up to a complete emptiness and remain quantitatively correct [65]. This is due to the fact that the gradientless hydrodynamic for this interaction is purely cubic, see (5.11). This fact has two important consequences: the first one is that the equations of motion can be written as Riemann-Hopf equations (5.25), which are trivially integrable with the implicit solution given by (5.26). This is important to connect the boundary conditions at infinity with those due to the DFP. The second fact is connected to the form of the parameters u and κ of the linearized theory, which in Hamiltonian formalism can be written in general as

$$H = \int \mathrm{d}x \left[\frac{u}{2\kappa} \Pi^2 + \frac{u\,\kappa}{2} \left(\nabla \phi \right)^2 \right] , \tag{5.68}$$

where $\Pi(x)$ and $\phi(x)$ are conjugated fields. In terms of hydrodynamic variables (5.20) they are

$$v(x) \equiv \Pi(x) , \qquad \rho(x) \equiv \rho_0 + \nabla \phi(x) , \tag{5.69}$$

where ρ_0 is the background value over which we are linearizing the theory. Note that $\kappa = \frac{1}{\pi K}$, where K is the conventional Luttinger parameter [106].

For Calogero-type models, the sound velocity u depends linearly on the

density, while the interaction parameter κ does not depend on the point around which we are linearizing. In appendix G we show that the sound velocity can be rescaled out of the DFP calculation (at zero temperature) and κ is the relevant factor encoding the interaction, which determines the coefficient of the Gaussian behavior of the DFP. All these peculiarities of the Calogero interaction conspire in a way that extending the small depletion result to higher depletion is "trivial" and, in fact, gives the correct result. Let us remark in this respect, that any non-linear theory can be seen as the integration of successive linear approximation, where the coefficients are adjusted at each point. In this light and from what we pointed out above, it is clear that the simplicity of the Calogero interaction allows a simple integration of successive linear theories for the DFP calculation and this is the reason for which the linearized result can be trivially extended from a small DFP to a complete EFP.

In appendix G we calculate the DFP in the linearized approximation (guided by [65]). The result is (G.9)

$$S_{DFP}^{\text{linear}} = \frac{\pi}{2}\,\kappa\,(\rho_0 - \tilde{\rho})^2\,R^2\ , \tag{5.70}$$

where we used $\eta = \bar{\eta} = \rho_0 - \tilde{\rho}$.

If we substitute (5.12) in (5.11) we can write the hydrodynamic Hamiltonian in terms of spin and charge fields as

$$\begin{aligned} H \;=\; & \int \mathrm{d}x \left\{ \frac{1}{2}\rho_c v_c^2 + \frac{\pi^2}{6}\left(\lambda+\frac{1}{2}\right)^2 \rho_c^3 + \rho_s v_c v_s \right. \\ & \left. + \left[\left(\lambda+\frac{1}{2}\right)\rho_c - \lambda\rho_s\right] v_s^2 + \frac{\pi^2}{4}\left(\lambda+\frac{1}{2}\right)\rho_c\rho_s^2 - \frac{\pi^2}{12}\,\lambda\,\rho_s^3 \right\}\ . \end{aligned} \tag{5.71}$$

By linearizing this Hamiltonian, i.e. by expanding the fields as $\rho_{c,s} = \rho_{0;c,s} + \delta\rho_{c,s}$ and looking at the coefficients in front of the quadratic part, we find the following parameters:

$$u_c(\rho_{0c}) = \pi\left(\lambda+\frac{1}{2}\right)\rho_{0c}\ , \qquad \kappa_c(\rho_{0c}) = \pi\left(\lambda+\frac{1}{2}\right)\ , \tag{5.72}$$

$$u_s(\rho_{0s}) = \pi\left(\lambda+\frac{1}{2}\right)\rho_{0c} - \pi\lambda\rho_{0s}\ , \qquad \kappa_s(\rho_{0s}) = \frac{\pi}{2}\ . \tag{5.73}$$

We see that substituting these values in (5.70) correctly reproduce (5.58, 5.66)

and therefore (5.36) as well. This means that not only the linearized theory is sufficient to calculate the correct coefficients of the EFP, but also that the spin-charge separation survives as if the linear theory was valid for high depletions as well.

To conclude, we can suggest a simple physical interpretation of (5.70). In a Calogero-Sutherland system, the interaction parameter $\kappa = \pi\lambda'$ has a simple semiclassical interpretation in terms of the phase-space area occupied by a single particle, see [48] and [15]. We can then see that (5.70) represent a volume in the $x - \tau - k$ space: the phase-space area at a given τ is of the order of $\kappa(\rho_0 - \tilde{\rho})R$, see, for instance, (5.24). This has to be multiplied by the number of particles involved in the depletion over time, which is of the order $(\rho_0 - \tilde{\rho})R$.

5.9 Conclusions

We calculated the Emptiness and Depletion Formation Probability for the spin Calogero-Model (5.1) and for the Haldane-Shastry Model (5.46). The EFP is one of the fundamental correlators in the theory of integrable models and, despite its being non-local, is considered to be one of the simplest. Nonetheless its asymptotic behavior is known only for a few systems and in this chapter we calculated it for the sCM and the HSM for the first time, at the leading order.

The DFP is a natural generalization of the EFP in the hydrodynamics formalism we employ. By calculating the DFP in its most generality (5.36), we can achieve the different EFPs by taking its appropriate limit. The calculation is done in an instanton picture, where the DFP is viewed as the probability of formation of a rare fluctuation in imaginary time that realizes the required depletion at a given moment.

The long distance asymptotics in 1-D models are normally calculated in a field theory approach using bosonization. However, as this approach is valid only for low-energy excitations close to the Fermi points where the linearization of the spectrum is a reasonable approximation, it is not sufficient for the EFP, which involves degrees of freedom deep in the Fermi sea. For this reason we used a non-linear version of bosonization, i.e. the hydrodynamic description

developed in [15].

All our formulae show a characteristic Gaussian behavior as a function of the depletion radius R. This is to be expected for a gapless one-dimensional system, as it was first argued in [101]. This is because in the asymptotic limit we consider, R is the biggest length scale in the system and therefore the instanton configuration will have a characteristic area of R^2, where the second power comes from the dimensionality of the space-time. In [65, 101] it was also shown that for small depletion, the linearized bosonization approach is sufficient to calculate the DFP, while in general it deviates from the correct results for progressively bigger depletion and, eventually, emptiness.

However, the Calogero-Sutherland kind of models (as well as non-interacting fermions) are special and the linearized result happen to coincide with the correct, non-linear one. We argued on the origin of this observation in the previous section. Moreover, we noticed that (5.36) and the analysis of section 5.6 and 5.7 indicates that, from a EFP perspective, spin-charge separation seems to survive beyond the linear approximation, in disagreement with what one naïvely would expect. This resurgence of linear results in a non-linear problem is a very surprising result, peculiar of the sCM.

The coefficients in front of R^2 are novel of this work. In section 5.8 we interpreted them from a bosonization point of view and via a simple semi-classical argument and throughout the chapter we have checked them against known results in certain limits where possible. In particular, we showed agreement with the free fermionic limit (5.40) and the splinless Calogero-Sutherland model (5.42). For both of these models, the EFP has a particular interest coming from Random Matrix Theory, as it is known that for certain rational values of the coupling parameter λ the CSM describes the RMT ensembles. It would be interesting if the sCM would also have an interpretation in terms of some generalized random matrix model, but we are not aware of such connection yet.

In section 5.5.4 we used the fact that the Haldane-Shastry model can be achieved as the freezing limit ($\lambda \to \infty$) of the sCM to calculate the Probability of Formation of (Partially) Ferromagnetic Strings in the HSM. In section 5.5.5, the same quantity was derived independently from the hydrodynamic description of the HSM. Section 5.5.4 and 5.5.5 highlight the correspondence

between large-λ sCM, HSM and $\lambda' = \lambda + 1 = 2$ splinless Calogero model from a EFP/DFP perspective.

In Chapters 3 ,4 and 5, we have studied the field theory aspects of the very special Calogero integrable family. This integrable system facilitates a more formal way of obtaining collective physics compared to those systems of Fermi gases studied in Chapter 2.

Chapter 6

The RKKY Interaction and the Nature of the Ground State of Double Dots in Parallel

6.1 Introduction

In the following two chapters of the thesis we study electron transport and correlations in a system of two quantum dots arranged in parallel. The main techniques used in this chapter are Slave Boson Mean Field Theory (SBMFT) and the Bethe Ansatz (BA). Quantum dots provide a means to realize strongly correlated physics in a controlled setting. Because of the ability to adjust gate voltages which control both the tunnelling amplitudes between the dots and the connecting leads and the dots' chemical potential, quantum dots can be tuned to particular physical regimes. One celebrated example of said tuning was the first realization of Kondo physics in a single quantum dot [107–110] obtained by adjusting the chemical potential of the dot such that the dot was occupied by one electron.

More generally, engineered multi-dot systems offer the ability to realize more exotic forms of Kondo physics. This was seen, for example, in the realization of the unstable fixed point of two-channel overscreened Kondo physics in a multi-dot system[111]. There has thus been considerable theoretical interest in double dots systems in different geometries, both in series (for example Refs. [112–117]) and in parallel (for example Refs. [3, 118–130]). In this chap-

ter we focus on the strongly correlated physics present on the latter geometry, in particular when there is no direct tunneling between the dots and the dots are not capacitively coupled. Such dot systems have been experimentally realized in numerous instances [131–133] (for other realizations of double dots in parallel see Refs. [134, 135]). Although the dots are not directly coupled, they are coupled through an effective Ruderman-Kittel-Kasuya-Yosida (RKKY) interaction. It is aim of this work to explore the nature of the RKKY interaction in parallel double quantum dots.

A straightforward application of the RKKY interaction as typically understood would lead one to believe that in a closely spaced double quantum dot with two electrons present, one on each dot, the RKKY interaction should lead to an effective ferromagnetic coupling between the dots. How should this coupling reveal itself in a transport experiment, the typical probe of a quantum dot system? If a ferromagnetic coupling is present, one expects the electrons on the two dots to bind into a spin-1 impurity. If the dots are coupled to a single effective lead, we obtain, in effect, an underscreened Kondo effect. As the temperature is lowered, the single effective lead will partially screen the spin-1 impurity to an effectively uncoupled spin-1/2 impurity. The ground state of the system will then be a non-Fermi liquid doublet. In particular at small temperatures and voltages, the conductance through the dot will be characterized by logarithms[136]. This scenario has been put forth in a number of NRG studies [119, 120, 122, 123] and is implicit in a number slave boson studies [124–126] of double dots in parallel.

We present contrary evidence here that this scenario is not in fact applicable at least for temperatures below the Kondo temperature. We argue that the ground state of closely spaced double dots is instead a Fermi liquid singlet. These findings are consistent with those of Ref. [113]. We do so using both the Bethe ansatz and slave boson mean field theory. It has been shown [3, 118] that under certain conditions double dots in parallel admit an exact solution using the Bethe ansatz. This exact solution, following the approach introduced in Ref. [137], can be exploited to compute transport properties. In particular, the zero temperature linear response conductance can be computed exactly. Double quantum dots, however, only admit an exact solution provided their parameters satisfy certain constraints. To ensure that our finding of Fermi

liquid behaviour is not an artifact of these constraints, we also study the parallel dot system using slave boson mean field theory. This allows one to study the sensitivity of our results to adding a second weakly coupled channel and to compute such quantities as the spin-spin correlation function, an object not directly computable in the Bethe ansatz.

The chapter is organized as follows. In Section 6.2 we detail the double dot model that we are interested in studying together with the approaches (Bethe ansatz and slave boson mean field theory) that we employ in studying this system. In Section 6.3 we present results on the linear response conductance through the dots both at zero temperature and finite temperature. We show the zero temperature conductance obeys the Friedel sum rule, a hall mark of Fermi liquid physics. We also study the impurity entropy at finite temperature showing that it vanishes in the zero temperature limit indicating the presence of a singlet. Finally in this section, we present results (using slave boson mean field theory alone) of the spin-spin correlation function. Lastly, in Section 6.4, we discuss the implications of our results [1] and suggest a way they can be reconciled with the conflicting NRG studies.

6.2 Model Studied

We study a set of two dots arranged in parallel with two leads. The Hamiltonian for this system is given by

$$\begin{aligned}\mathcal{H} &= -i\sum_{l\sigma}\int_{-\infty}^{\infty} dx c_{l\sigma}^{\dagger}\partial_x c_{l\sigma} + \sum_{\sigma\alpha} V_{l\alpha}(c_{l\sigma\alpha}^{\dagger} d_{\sigma\alpha} + \text{h.c}) \\ &\quad + \sum_{\sigma\alpha}\epsilon_{d\alpha} n_{\sigma\alpha} + \sum_{\alpha} U_{\alpha} n_{\uparrow\alpha} n_{\downarrow\alpha}. \end{aligned} \tag{6.1}$$

The $c_{l\sigma}$ specify electrons with spin σ living on the two leads, $l = 1, 2$. The $d_{\alpha\sigma}$ specify electrons found on the two dots $\alpha = 1, 2$. Electrons can hop from the leads to dots with tunneling strength $V_{l\alpha}$. The strength of the Coulomb repulsion on the two dots is given by U_{α}. We suppose that there is no interdot Coulomb repulsion and that tunneling between the two dots is negligible. A

[1] We also investigate questions of this nature via the 1/N expansion method (See Chapter 7).

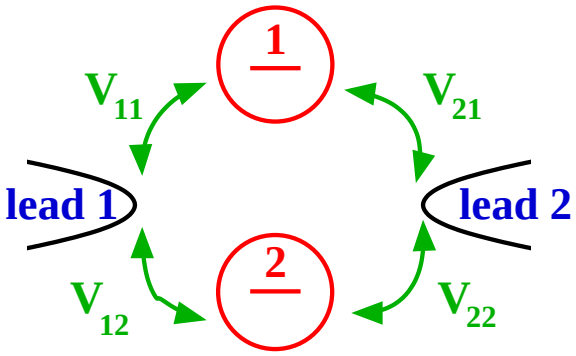

Figure 6.1: A schematic of the double dot system.

schematic of this Hamiltonian for the two dots is given in Fig. 6.1.

6.2.1 Bethe Ansatz

The above Hamiltonian can be solved exactly via Bethe ansatz under certain conditions. The set of constraints that we will be particularly interested in are as follows:

$$V_{1\alpha}/V_{2\alpha} = V_{1\alpha'}/V_{2\alpha'};$$

$$U_\alpha \Gamma_\alpha = U_{\alpha'} \Gamma_{\alpha'};$$

$$U_\alpha + 2\epsilon_{d\alpha} = U_{\alpha'} + 2\epsilon_{d\alpha'}. \tag{6.2}$$

The first of these conditions results in only a single effective channel coupling to the two leads. This occurs automatically when the dot hoppings are chosen to be symmetric and so is commonly found in the literature[119, 120, 124, 126–128, 138]. The second condition tells us that with $U_{1,2}$ fixed, $\epsilon_{d1} - \epsilon_{d2}$, is also fixed. We thus must move $\epsilon_{d1,2}$ in unison in order to maintain integrability. The final condition tells us that $\sqrt{U_i\Gamma_i}$, the bare scale governing charge fluctuations on the dots must be the same on both dots.

To solve this Hamiltonian we implement a map to even and odd channels, $c_{e/o} = (V_{1/2,\alpha}c_1 \pm V_{2/1,\alpha}c_2)/\sqrt{2\Gamma_\alpha}$ where $\Gamma_\alpha = (V_{1\alpha}^2 + V_{2\alpha}^2)/2$. Under the map, the Hamiltonian factorizes into even and odd sectors:

$$\begin{aligned}
\mathcal{H}_e &= -i\sum_{l\sigma}\int_{-\infty}^{\infty} dx\ c_{e\sigma}^\dagger \partial_x c_{e\sigma} + \sum_{\sigma\alpha}\sqrt{2\Gamma_\alpha}(c_{e\sigma\alpha}^\dagger d_{\sigma\alpha} + \text{h.c}) \\
&\quad + \sum_{\sigma\alpha}\epsilon_{d\alpha}n_{\sigma\alpha} + \sum_\alpha U_\alpha n_{\uparrow\alpha}n_{\downarrow\alpha}; \\
\mathcal{H}_o &= -i\sum_{l\sigma}\int_{-\infty}^{\infty} dx\ c_{o\sigma}^\dagger \partial_x c_{o\sigma},
\end{aligned} \tag{6.3}$$

where, as can be seen, the odd sector decouples from the double dot. Using the Bethe ansatz [3, 118] one can construct N-particle wave functions in the non-trivial even sector. These wavefunctions are characterized by N-momenta $\{q_i\}_{i=1}^N$ and M quantum numbers $\{\lambda_\alpha\}_{\alpha=1}^M$. The number of λ_α's mark the spin quantum number of the wave function: $S_z = N - 2M$. Together the λ_α's and q_i's satisfy the following set of constraints:

$$\begin{aligned}
e^{iq_jL + i\delta(q_j)} &= \prod_{\alpha=1}^M \frac{g(q_j) - \lambda_\alpha + i/2}{g(q_j) - \lambda_\alpha - i/2}; \\
\prod_{j=1}^N \frac{\lambda_\alpha - g(q_j) + i/2}{\lambda_\alpha - g(q_j) - i/2} &= -\prod_{\beta=1}^M \frac{\lambda_\alpha - \lambda_\beta + i}{\lambda_\alpha - \lambda_\beta - i},
\end{aligned} \tag{6.4}$$

where $g(q) = \frac{(p - \epsilon_{d\alpha} - U_\alpha/2)^2}{2\Gamma_\alpha U_\alpha}$. These equations are identical to the set of constraints for a single dot [139, 140] but for the form of the scattering phase

$\delta(q)$:

$$\delta(q) = -2\tan^{-1}(\sum_{\alpha} \frac{\Gamma_\alpha}{q - \epsilon_{d\alpha}}). \tag{6.5}$$

We will focus in this chapter on computing transport properties in linear response. At zero temperature we can use the Bethe ansatz to access such transport quantities exactly[3, 137]. We will also use the Bethe ansatz to obtain an excellent quantitatively accurate prediction (in comparison with NRG) for the finite temperature linear response conductance (see Refs. [3, 137] for the Bethe ansatz computation of the finite temperature linear response conductance for a single dot and for the comparable NRG, Ref. [141]).

The Bethe ansatz can be exploited to develop certain approximations that allow one to compute certain non-equilibrium quantities, in particular, the out-of-equilibrium conductance [137] and the noise [142] in the presence of a magnetic field. In order to obtain at least qualitatively accuracy, the presence of a magnetic field is a necessity. With a magnetic field the Bethe ansatz for a single dot correctly predicts such features as the positioning of the peak in the differential magnetoconductance [142] as say measured in carbon nanotube quantum dots[143]. In the absence of a magnetic field, the Bethe ansatz inspired approximation breaks down however[142]. We will, again, not consider the double dots out-of-equilibrium in this work.

6.2.2 Slave Boson Mean Field Theory

We also study the Hamiltonian (6.1) using a slave-boson mean field theory, a well-known technique, applicable at sufficiently low temperatures[144]. The starting point is the same Hamiltonian (6.1) and we will study here the $U_\alpha = \infty$ case. The constraint of preventing double-occupancy on the dots is fulfilled by introducing two Lagrange multipliers λ_1 and λ_2. The slave boson formalism consists of writing the impurity fermionic operator on each dot as a combination of a pseudofermion and a boson operator: $d_{\sigma\alpha} = b_\alpha^\dagger f_{\sigma\alpha}$. Here $f_{\sigma\alpha}$ is the pseudofermion which annihilates one "occupied state" on dot α and $b_\alpha^\dagger$ is a bosonic operator which creates an empty state on dot α. The mean field approximation consists of replacing the bosonic operator by its expectation value: $b_\alpha^\dagger \to \left\langle b_\alpha^\dagger \right\rangle = r_\alpha$. Thus r_α and λ_α together form four parameters which need to be determined using mean field equations. Under the slave boson

formalism combined with the mean field approximation, Eq. (6.1) reads

$$\begin{aligned} H_{SBMFT} &= -i\sum_{l\sigma}\int_{-\infty}^{+\infty} dx c^{\dagger}_{l\sigma}\partial_x c_{l\sigma} + \sum_{l\alpha\sigma}\tilde{V}_{l\alpha}\left(c^{\dagger}_{l\sigma}f_{\sigma\alpha} + \text{h.c}\right) \\ &+ \sum_{\sigma\alpha}\tilde{\epsilon}_{d\alpha}f^{\dagger}_{\sigma m}f_{\sigma m} + i\sum_{\alpha}\lambda_{\alpha}(r^2_{\alpha}-1) \end{aligned} \tag{6.6}$$

with $\tilde{V}_{l\alpha} = r_{\alpha}V_{l\alpha}$ and $\tilde{\epsilon}_{d\alpha} = \epsilon_{d\alpha} + i\lambda_{\alpha}$. The mean field equations are the constraints for the dot $\alpha = 1, 2$,

$$\sum_{\sigma} < f^{\dagger}_{\alpha\sigma}(t)f_{\alpha\sigma}(t) > + r^2_{\alpha} = 1, \tag{6.7}$$

and the equation of motion (EOM) of the boson fields,

$$\text{Re}\left[\sum_{l,k,\sigma}\tilde{V}^{*}_{l\alpha}\left\langle c^{\dagger}_{kl\sigma}(t)f_{\sigma\alpha}(t)\right\rangle\right] + i\lambda_{\alpha}r^2_{\alpha} = 0. \tag{6.8}$$

The above equations can be understood as arising from the conditions

$$\begin{aligned} \frac{\partial\left\langle H_{SBMFT}\right\rangle}{\partial\lambda_{\alpha}} &= 0; \\ \frac{\partial\left\langle H_{SBMFT}\right\rangle}{\partial r_{\alpha}} &= 0. \end{aligned} \tag{6.9}$$

Thus the reality condition on Eqn. 2.8 arises from the reality of the hopping term in the Hamiltonian[145]. For any given set of bare parameters $(\epsilon_{d\alpha\sigma}, V_{l\alpha})$ we can compute the renormalized energy $(\tilde{\epsilon}_{d\alpha\sigma})$ and renormalized hybridization $(\tilde{V}_{l\alpha})$ by solving the four equations, Eqns. 6.7 and 6.8. While these results are mean field, they allow one to span a wide parameter space not constrained by the requirements of integrability. For instance, we study asymmetrically coupled dots where two channels couple to the dot, a case not solvable by the Bethe Ansatz. SBMFT allows one also, unlike the Bethe ansatz, to readily study such quantities as the spin-spin correlation function.

6.3 Results

In this section we present a number of measures as computed using both the Bethe ansatz and slave boson mean field theory that are indicative of the ground state of the double dot plus lead system. We will argue that these are consistent with the ground state of the dot being a singlet state, not a doublet.

6.3.1 Zero Temperature Conductance

The first measure we examine is the zero temperature linear response conductance, G. For the BA, G is computed as is discussed in great detail in Refs. [137] and [3]. For the SBMFT, G is computed by first solving for the variational parameters, r_α, and $\tilde{\epsilon}_{d\alpha}$, $\alpha = 1, 2$, and then determining the corresponding transmission amplitude via solving a one-particle Schrödinger equation. This procedure is detailed in Appendix B.

If the double dot is in a singlet state, we expect G to vanish as $\epsilon_{d1,2}$ are lowered, moving the dot into the Kondo regime. This is consistent with understanding the singlet state as a Fermi liquid state. If a Fermi liquid, G will obey the Friedel sum rule:[146]

$$G = \sum_{\sigma=\uparrow,\downarrow} \frac{e^2}{h} \sin^2(\pi n_{d\sigma}), \tag{6.10}$$

where $n_{d\sigma}$ is the number of electrons of spin species σ displaced by the dot. Deep in the Kondo regime, there will be two electrons sitting on the two dots, one of each spin species, i.e. $n_{d\sigma} = 1$, and so G correspondingly vanishes.

Plotted in Fig. 6.2 is the zero temperature conductance as computed with BA and SBMFT as a function of ϵ_{d1} and with $\epsilon_{d1} - \epsilon_{d2}$ fixed. For each computational methodology we present results for both $\epsilon_{d1} - \epsilon_{d2} \gg \Gamma_{1,2}$ and $\epsilon_{d1} - \epsilon_{d2} \ll \Gamma_{1,2}$. We see that in all cases that as $\epsilon_{d1,2}$ is lowered, the conductance vanishes. We do note however that the overall structure of the conductance differs as computed between the BA and SBMFT, that is to say, the SBMFT fails in general to describe the correct behaviour. In particular it fails to describe the intermediate valence regime when the distance separating the chemical potential of the two dots is large, i.e $\epsilon_{d1} - \epsilon_{d2} \gg \Gamma_{1,2}$. In the intermediate valence regime the conductance of the double dot as computed

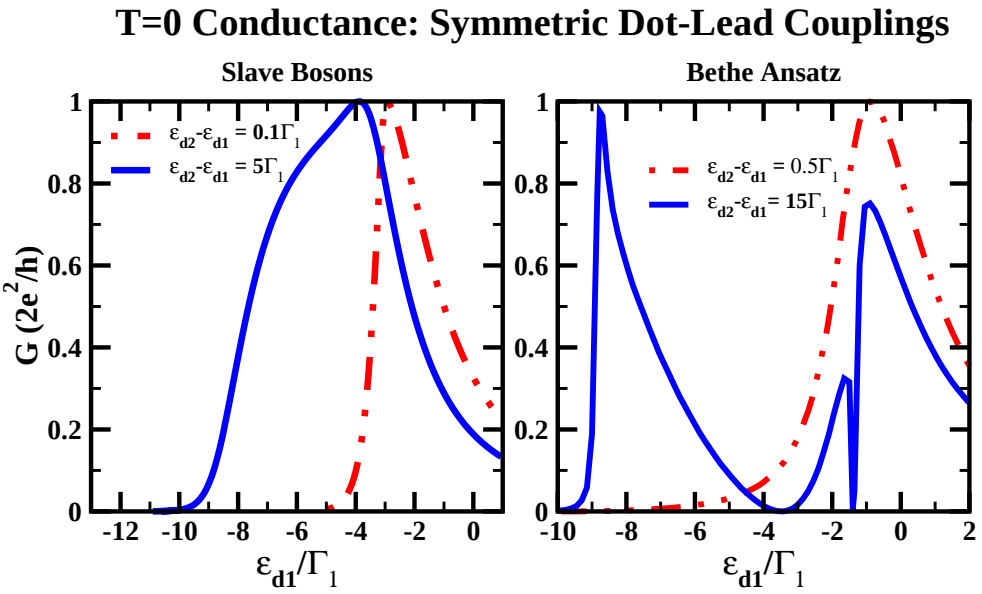

Figure 6.2: The zero temperature conductance of a symmetrically coupled double dot computed using slave boson mean field theory and the Bethe ansatz. For slave bosons we assume the symmetric case $V_{ij} = 1$.

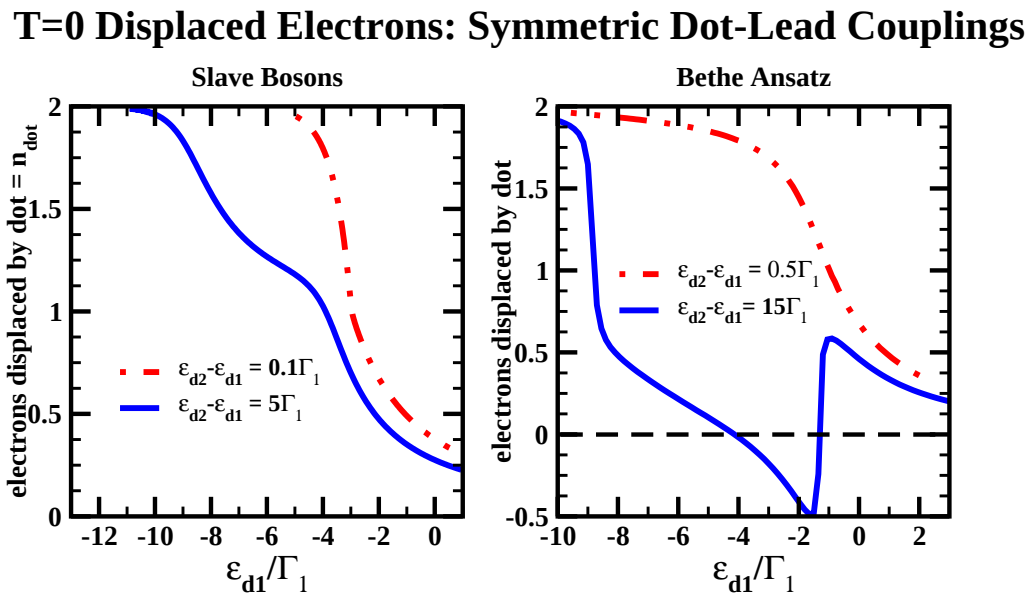

Figure 6.3: The number of electrons displaced by the dots, n_d of a symmetrically coupled double dot computed both using SBMFT and the Bethe ansatz. In the case of SBMFT, n_d is simply the dot occupation, $n_{dot} = \sum_{i\sigma}\langle d^\dagger_{i\sigma} d_{i\sigma}\rangle$. In the case of the Bethe ansatz, the quantity plotted is equal to the dot occupation *plus* the $1/L$ correction to the electron density in the leads induced by coupling the dots to the leads. For slave bosons we assume the symmetric case $V_{ij} = 1$.

with the BA undergoes rapid changes, a consequence of interference between electrons tunneling off and on the dot (see Ref. [3]). This is not mirrored in the SBMFT computations which remain comparatively structureless.

The failure of SBMFT to accurately capture the physics in the intermediate valence regime is seen in a related quantity, the number of electrons displaced by the dot. n_d is the sum of two terms:

$$n_d = \sum_{\sigma i} \langle d^\dagger_{\sigma i} d_{\sigma i} \rangle + \sum_{\sigma l} \int dx \Big[\langle c^\dagger_{\sigma l} c_{\sigma l} \rangle - \rho_{\sigma_{\text{bulk}}} \Big]. \tag{6.11}$$

The first term is simply the occupancy of the double dots while the second term measures the deviation of electron density in the leads due to coupling the dots and the leads. In SBMFT this term is zero due to the mean field nature of its approximation. However in BA this term is non-zero. While we cannot compute it directly, the BA gives us the ability to compute n_d. And as plotted on the r.h.s. of Fig. 6.3, we see that n_d can be negative. As $\sum_{\sigma i} \langle d^\dagger_{\sigma i} d_{\sigma i} \rangle$ is manifestly a positive quantity, we know that as computed by the BA, the second term in Eq.(6.11) is non-zero and in fact is negative (at least in the case $\epsilon_{d1} - \epsilon_{d2} \gg \Gamma_{1,2}$). From Fig. 6.3 we see however that n_d for both SBMFT and BA tends to two as the system enters the Kondo regime (where two electrons sit on the two dots).

One advantage the SBMFT does offer over the BA is that it allows us to compute transport quantities beyond the integrable parameter regime delineated in Eq. (6.2). It was argued in Ref.[3] that small deviations away from this parameter space should not qualitatively change transport properties. In Fig. 6.4 we test this in the Kondo regime (where we expect SBMFT to be at its most accurate) computing the conductance while adjusting the dot-lead hopping parameters in such a way that we move from a case where only one effective channel couples to the quantum dot (i.e. $V_{ij} = 1$) to a case where two channels couple to the dot ($V_{11} > 1$ and $V_{12} = V_{21} = V_{22} = 1$). We see when the second channel is only weakly coupled to the dot, the conductance remains near its one-channel value, i.e. $G = 0e^2/h$. Only once V_{11} appreciably deviates from 1 do we see a corresponding deviation in G. We note that this continuous behaviour is also consistent with the one-channel dot-lead ground state being a singlet. If it were instead a doublet, coupling a second channel

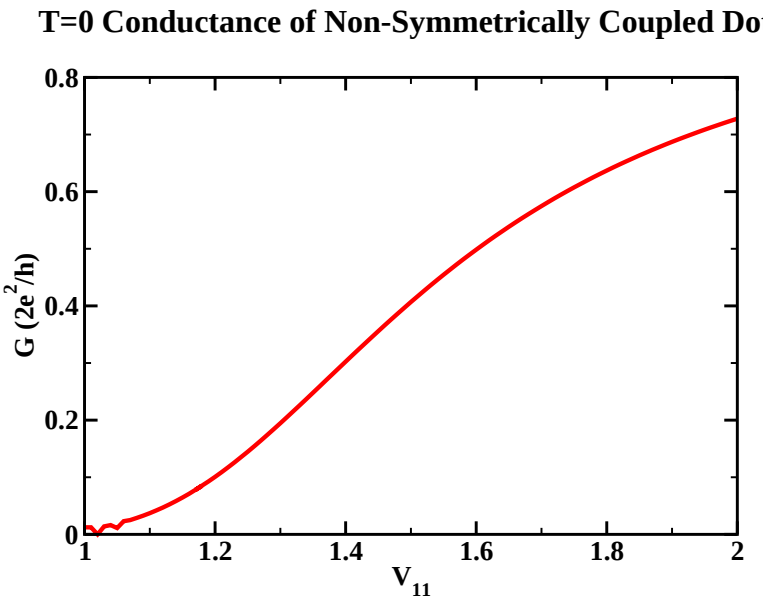

Figure 6.4: The zero temperature conductance of asymmetrically coupled double dot computed using slave boson mean field theory. The conductance is plotted as a function of V_{11}. The remaining dot-lead hopping strengths are all set to 1 while $\epsilon_{d1} = -4.7$ and $\epsilon_{d2} = -4.6$. The system is in the Kondo regime.

into the system would lead to a discontinuous change as the second channel, no matter how weakly coupled, would immediately screen the free effective spin-1/2.

Finally in this section we consider the behaviour of the conductance and displaced electrons when $\epsilon_{d1} = \epsilon_{d2}$. We see from Fig. 6.5 that the same qualitative behaviour in both quantities is found using the Bethe ansatz and using SBMFT. Namely, the displaced electron number n_d tends to 2 while the conductance G tends to zero as $\epsilon_{d1} = \epsilon_{d2}$ goes to zero. While these measures are the same in the two computational methods, there is a quantity that sharply distinguishes the two (and so shows a failure of SBMFT even in the Kondo regime at zero temperature). This quantity is the low lying density of states on the dots, $\rho_d(\omega)$. For the case of $\epsilon_{d1} = \epsilon_{d2}$, the BA shows that $\rho_d(\omega)$ for ω on the order of the Kondo temperature, T_K vanishes.[3] However the SBMFT shows that at this energy scale there exists non-negligible spectral weight. In Fig. 6.6, we plot $\rho_d(\omega)$ as defined by

$$\rho_d(\omega) = \sum_{i\sigma} \mathrm{Im}\langle d^\dagger_{i\sigma} d_{i\sigma}\rangle_{retarded}.$$

The agreement on the qualitative features of n_d and G between the two methodologies is then a coincidence (to a degree). In both cases the ground state is Fermi liquid like and so G follows the Friedel sum rule which necessarily mandates that the conductance vanish with two electrons on the two dots. But the nature of the Fermi liquid in each case as predicted by the methodologies is much different. SBMFT predicts the scale of the low lying excitations is T_K while the BA finds that for the special case of $\epsilon_{d1} = \epsilon_{d2}$ (and only for this case[3]) that the fundamental energy scale corresponds to the bare energies scales in the problem, i.e. U and Γ.

6.3.2 Finite Temperature Conductance

We now consider the finite temperature conductance. Plotted in Fig. 6.7 are traces for $G(T)$ for double dots with both $|\epsilon_{d1} - \epsilon_{d2}| \gg \Gamma_{1,2}$ and $|\epsilon_{d1} - \epsilon_{d2}| \ll \Gamma_{1,2}$ as computed with both the Bethe ansatz as well as SBMFT. For a Fermi liquid ground state we expect that at low temperatures the conductance deviate from its zero temperature value by T^2 and we see that behaviour in both

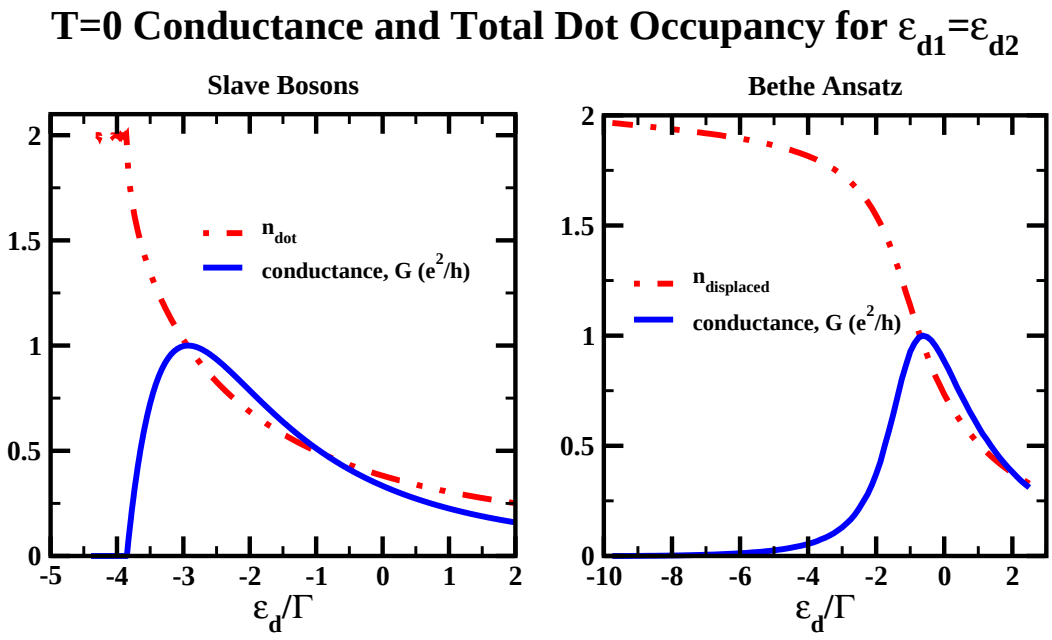

Figure 6.5: The conductance and the number of displaced electrons as a function of $\epsilon_{d1}(=\epsilon_{d2})$ as computed using SBMFT and the Bethe ansatz. For slave bosons we assume the symmetric case $V_{ij} = 1$.

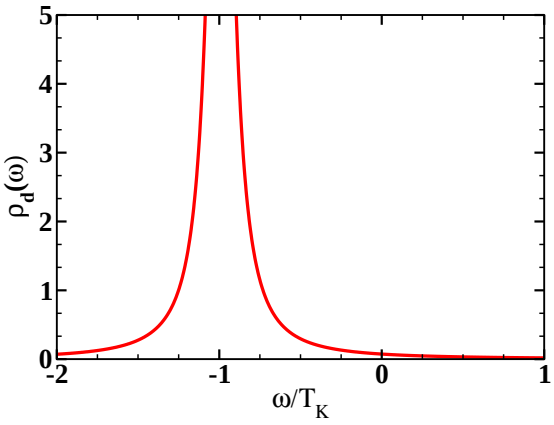

Figure 6.6: A plot of the low energy density of states, $\rho(\omega)$ for $\epsilon_{d1} = \epsilon_{d2} = -4.45\Gamma_{1,2}$ in the Kondo regime as computed using SBMFT. As we are argue in the text, this is an artifact of SBMFT (the BA shows that in this case $\rho_d(\omega)$ vanishes[3]).

cases. From Fig. 6.7 we see that in both treatments, the finite temperature conductance for the double dots initially rises with increasing temperature to an appreciable fraction of the unitary maximum and thereafter decreases in an uniform manner (regardless of the bare level separation). (For SBMFT we have defined the Kondo temperature as where this peak in $G(T)$ occurs while for the BA the Kondo temperature we employ the analytic expression for T_K of the double dots derived in Ref. [3].) We however also see that there are qualitative differences between SBMFT and the Bethe ansatz. The peak in the conductance computed using SBMFT peaks at a value far closer to the unitary maximum than does the Bethe ansatz. And we also see that the conductance as computed in the SBMFT drops off far more rapidly than it does in the BA (particularly at large level separation). We however believe this is unphysical and akin to the pathologies that SBMFT is known to exhibit at higher temperatures and energy scales.[145, 147–152]

As was demonstrated in Ref. [3], the conductance at finite but small T is quadratic in T while at large T the conductance is logarithmic (going as $1/\log^2(T/T_K)$). The peak in conductance at finite T is then a result of the conductance vanishing in the low and high temperature limits. These conduc-

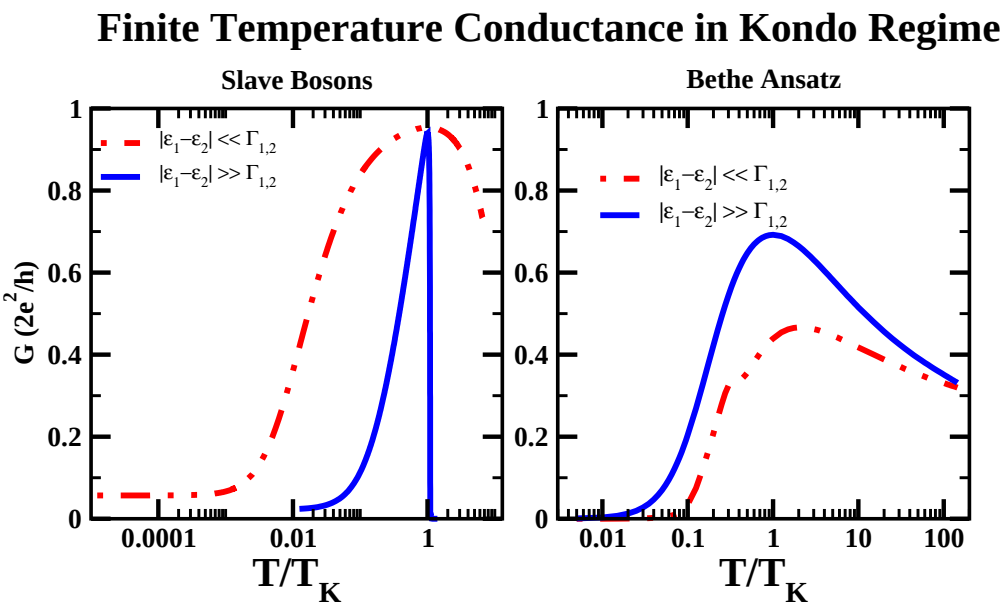

Figure 6.7: The linear response conductance as a function of temperature of a symmetrically coupled double dot computed using both slave boson mean field theory and the Bethe ansatz. For small separation in slave boson approach we had $\epsilon_1 - \epsilon_2 = 0.05\Gamma_{1,2}$ and $\epsilon_1 = -4.1\Gamma_{1,2}$. For large separation in slave boson approach we had $\epsilon_1 - \epsilon_2 = 5\Gamma_{1,2}$ and $\epsilon_1 = -9.4\Gamma_{1,2}$. In slave bosons we consider the symmetric case $V_{ij} = 1$.

tance profiles are similar to the those predicted in Ref. [153] for multi-dots coupled to *two* electron channels. However the physics there is much different: the non-monotonicity in $G(T)$ predicted in Ref. [153] is due to the presence of the two channels and because they couple to the dots with different strengths, they screen a $S > 1/2$ state in stages.

6.3.3 Spin-Spin Correlation Function

We present the static spin-spin correlation function as a function of ϵ_{d1} and as computed using SBMFT in Fig. 6.8. With two electrons on the dot the value of $\langle S_1 \cdot S_2 \rangle$ can vary between $-3/4$ (if these two electrons are bound in a singlet state) to $1/4$ (if the two electrons find themselves in a triplet state). We see in Fig. 6.8 that generically the value of the correlation function in the Kondo regime (for the relevant values of ϵ_{d1} see Fig. 6.2) that $\langle S_1 \cdot S_2 \rangle$ tends to 0. This however should not necessarily be interpreted as the dots being closer to a triplet state than a singlet state. In determining the overall state of the system, $\langle S_1 \cdot S_2 \rangle$, is not necessarily a good measure. We can see this by considering a simple toy example.

Imagine a system of four spins, two associated with the dots, $|\uparrow\rangle_{d1}$ and $|\uparrow\rangle_{d2}$, and two associated with leads $|\uparrow\rangle_{l1}$ and $|\uparrow\rangle_{l2}$. And first suppose the system is in a singlet state. Two ways that this singlet state can be formed are

$$\begin{aligned} |\text{singlet 1}\rangle &= \frac{1}{2}(|\uparrow\rangle_{d1}|\downarrow\rangle_{d2} - |\downarrow\rangle_{d1}|\uparrow\rangle_{d2}) \otimes (|\uparrow\rangle_{l1}|\downarrow\rangle_{l2} - |\downarrow\rangle_{l1}|\uparrow\rangle_{l2}); \\ |\text{singlet 2}\rangle &= \frac{1}{2}(|\uparrow\rangle_{l1}|\downarrow\rangle_{d1} - |\downarrow\rangle_{l1}|\uparrow\rangle_{d1}) \otimes (|\uparrow\rangle_{l2}|\downarrow\rangle_{d2} - |\downarrow\rangle_{l2}|\uparrow\rangle_{d2}) \end{aligned} \tag{6.12}$$

We see that the expectation value, $\langle S_1 \cdot S_2 \rangle$, of these two states is considerably different:

$$\begin{aligned} \langle \text{singlet 1}|S_1 \cdot S_2|\text{singlet 1}\rangle &= -3/4 \\ \langle \text{singlet 2}|S_1 \cdot S_2|\text{singlet 2}\rangle &= 0. \end{aligned} \tag{6.13}$$

Now suppose the system is in a triplet state and suppose its S_z projection

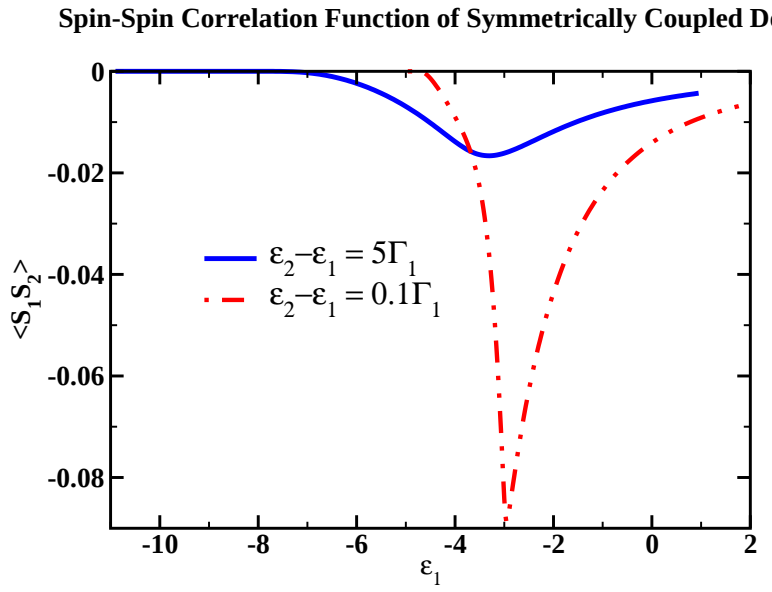

Figure 6.8: The spin-spin correlation function of symmetrically coupled double dot computed using slave boson mean field theory. We consider the symmetric case $V_{ij} = 1$.

is 1. Again there are two inequivalent ways this state can be formed:

$$\begin{aligned} |\text{triplet } 1\rangle &= \frac{1}{\sqrt{2}}|\uparrow\rangle_{d1}|\uparrow\rangle_{d2} \otimes (|\uparrow\rangle_{l1}|\downarrow\rangle_{l2} - |\downarrow\rangle_{l1}|\uparrow\rangle_{l2}); \\ |\text{triplet } 2\rangle &= \frac{1}{\sqrt{2}}|\uparrow\rangle_{l1}|\uparrow\rangle_{d1} \otimes (|\uparrow\rangle_{l2}|\downarrow\rangle_{d2} - |\downarrow\rangle_{l2}|\uparrow\rangle_{d2}). \end{aligned} \tag{6.14}$$

The expectation of these two values is

$$\begin{aligned} \langle\text{triplet } 1|S_1 \cdot S_2|\text{triplet } 1\rangle &= 1/4 \\ \langle\text{triplet } 2|S_1 \cdot S_2|\text{triplet } 2\rangle &= 0. \end{aligned} \tag{6.15}$$

We thus see that when the system's state is such that $\langle S_1 \cdot S_2 \rangle = 0$, it can be either a singlet or a triplet equally. We thus end with a more reliable measure of the dot's internal degrees of freedom: the impurity entropy.

6.3.4 Impurity Entropy

The final set of computations we present in this section are of the impurity entropy of the double dots. In Fig. 6.9 we plot results coming from SBMFT and the BA for both large and small level separation. (The derivation of the impurity entropy in the context of the BA is found in Appendix H.) We see that in all cases the impurity entropy vanishes as $T \to 0$. This then implies the ground state of the double dot system is a singlet. If it were a triplet state, the $T \to 0$ limit would lead to $S_{imp} = \log(2)$.

6.4 Discussion and Conclusions

We have presented a number of arguments that the ground state of a double dot near the particle-hole symmetric point (i.e. when there are nearly two electrons on the dots) is in a singlet Fermi liquid state. In particular we have shown that the conductance in this limit vanishes, in accordance with the Friedel sum rule and that the impurity entropy also vanishes, in agreement with the ground state being a singlet.

These conclusions however disagree with a number of NRG studies. In Refs.

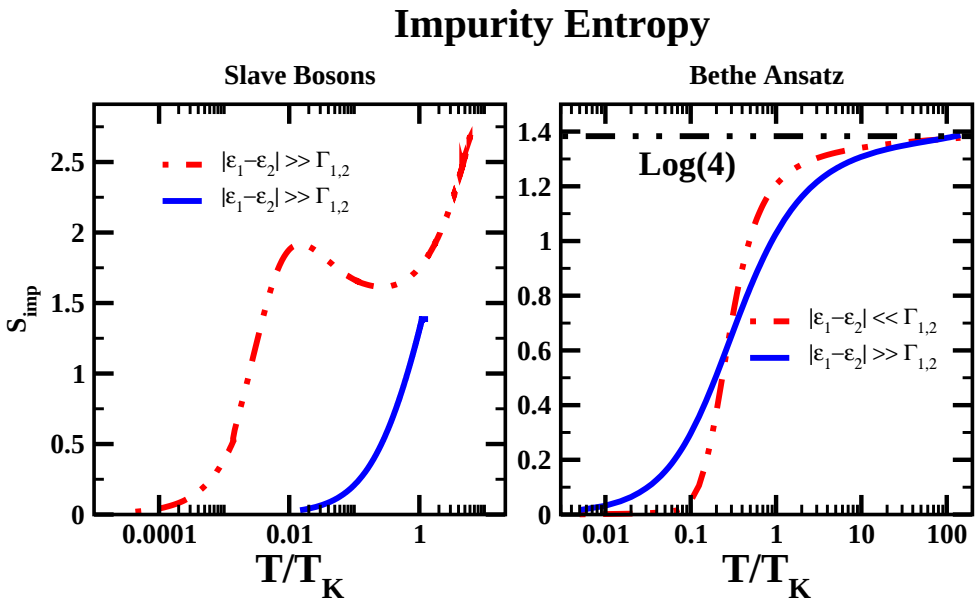

Figure 6.9: The impurity entropy as a function of temperature of a symmetrically coupled double dot computed using slave boson mean field theory and the Bethe ansatz. For small separation in slave boson approach we had $\epsilon_1 - \epsilon_2 = 0.05\Gamma_{1,2}$ and $\epsilon_1 = -4.1\Gamma_{1,2}$. . For large separation in slave boson approach we had $\epsilon_1 - \epsilon_2 = 5\Gamma_{1,2}$ and $\epsilon_1 = -9.4\Gamma_{1,2}$. In slave bosons we consider the symmetric case $V_{ij} = 1$.

[119] and [120] it is found that a double quantum dot (with the dots closely spaced) carrying two electrons is in a spin-triplet state, has a conductance corresponding to the unitary maximum, and is correspondingly a non-Fermi liquid. Similar conclusions are reached in Refs. [122, 123]. The basic rationale invoked for observing this physics is that with dots closely spaced, a ferromagnetic RKKY interaction is present which binds the two electrons on the dot into a spin triplet. Consequently the ground state of the double dot is that of an underscreened spin-1 Kondo impurity.

We offer a possible reason for the discrepancy that we find with these studies. The Anderson Hamiltonian typically considered in these studies is of the form:

$$\begin{aligned} H &= H_{lead} + H_{dot} + H_{lead-dot}; \\ H_{lead} &= D\int_{-1}^{1} k dk a^{\dagger}_{k\sigma} a_{k\sigma}; \\ H_{dot} &= \sum_{i=1,2;\sigma} \epsilon_{di} d^{\dagger}_{i\sigma} d_{i\sigma} + \sum_{i} U_i n_{i\uparrow} n_{i\downarrow}; \\ H_{dot-lead} &= D^{1/2} \sum_{i\sigma} \int_{-1}^{1} dk\ V_i (d^{\dagger}_{i\sigma} a_{k\sigma} + a^{\dagger}_{k\sigma} d_{i\sigma}) \end{aligned} \tag{6.16}$$

where we are using the conventions of Ref. [154] in writing down the NRG Hamiltonian. Before implementing the NRG algorithm, one adopts a logarithmic basis for the lead electrons,

$$a_{k\sigma} = \sum_{np} a_{np\sigma} \psi^{+}_{np}(k) + b_{np\sigma} \psi^{-}_{np}(k), \tag{6.17}$$

where

$$\psi^{\pm}_{np}(k) = \begin{cases} \frac{\Lambda^{n/2}}{(1-\Lambda^{-1})^{1/2}} e^{\pm i\omega_n pk} & \text{if } \Lambda^{-(n+1)} < \pm k < \Lambda^{-n}, \\ 0 & \text{if k is not within the above interval,} \end{cases} \tag{6.18}$$

and w_n is given by

$$w_n = \frac{2\pi\Lambda^n}{1-\Lambda^{-1}}. \tag{6.19}$$

Here Λ is a parameter less than one. This change of basis transforms H_{lead}

and $H_{lead-dot}$ into

$$\begin{aligned} H_{lead} &= \frac{D}{2}(1+\Lambda^{-1})\sum_{np}\Lambda^{-n}(a^\dagger_{np\sigma}a_{np\sigma}-b^\dagger_{np\sigma}b_{np\sigma}) \\ &\quad +\frac{D(1-\Lambda^{-1})}{2\pi i}\sum_{n}\sum_{p\neq p'}\exp(\frac{2\pi i(p'-p)}{1-\Lambda^{-1}})(a^\dagger_{np\sigma}a_{np'\sigma}-b^\dagger_{np\sigma}b_{np'\sigma})\frac{\Lambda^{-n}}{p'-p}; \\ H_{lead-dot} &= D^{1/2}(1-\Lambda^{-1})^{1/2}\sum_{in\sigma}\Lambda^{-n/2}V_i((a^\dagger_{n0\sigma}+b^\dagger_{n0\sigma})d_i+\text{h.c.}). \end{aligned} \tag{6.20}$$

Typically the approximation that is now made in most NRG treatments (and seems to have been made in the above references) is that the $p \neq 0$ modes of the logarithmic basis are dropped, not least because these modes do not directly couple to the dot. In the single dot case, where this approximation was first made,[154, 155] this was found to be a reasonable approximation. However in the double dot case it is not *a priori* obvious that this is the case. In particular if one finds an underscreened Kondo effect one might ask whether that additional modes ($p \neq 0$) might serve to provide additional screening channels.

Let us then consider the NRG Hamiltonian that would arise if both the $p = 0$ and $p = \pm 1$ modes were kept. H_{lead} can then be trivially diagonalized using the combination

$$\begin{aligned} r_{n0\sigma} &= \frac{1}{3}\left(2a_{n1\sigma}-e^{\theta}a_{n0\sigma}+2e^{2\theta}a_{n-1\sigma}\right); \\ r_{n\pm\sigma} &= \frac{1}{3\sqrt{10}}\left[5a_{n1\sigma}+(2\mp 6i)e^{\theta}a_{n0\sigma}-(4\pm 3i)e^{2\theta}a_{n-1\sigma}\right], \end{aligned}$$

with $\theta = -\frac{2\pi i}{1-\Lambda^{-1}}$. Note that the corresponding transformation $\{s \leftrightarrow b\}$ is omitted for brevity. This yields

$$\begin{aligned} H_{lead} &= D\sum_{n\sigma}\Lambda^{-n}\Bigg\{\frac{1+\Lambda^{-1}}{2}r^\dagger_{n0\sigma}r_{n0\sigma}+\frac{2\pi(1+\Lambda)+3(1-\Lambda)}{4\pi\Lambda}r^\dagger_{n+\sigma}r_{n+\sigma} \\ &\quad +\frac{2\pi(1+\Lambda)-3(1-\Lambda)}{4\pi\Lambda}r^\dagger_{n-\sigma}r_{n-\sigma}-\{r\to s\}\Bigg\} \end{aligned}$$

The corresponding transformation of the dot-lead Hamiltonian is

$$H_{dot-lead} = \sum_{in\sigma} V_{ni} \left[\sqrt{\frac{2}{5}} \left(\frac{1}{3} - i \right) r^{\dagger}_{n+\sigma} d_{i\sigma} + \sqrt{\frac{2}{5}} \left(\frac{1}{3} + i \right) r^{\dagger}_{n-\sigma} d_{i\sigma} - \frac{1}{3} r^{\dagger}_{n0\sigma} d_{i\sigma} + \{r \to s\} + h.c \right], \tag{6.21}$$

with $V_{ni} = D^{\frac{1}{2}}(1-\Lambda^{-1})^{\frac{1}{2}}\Lambda^{-\frac{n}{2}} e^{\theta} V_i$.

We see upon this diagonalization that three channels of electrons, $r_{n\{0,\pm\},\sigma}$ and $s_{n\{0,\pm\}\sigma}$, couple to the dot. And because of the nature of the logarithmic basis, we see that $+$, $-$ and 0 variables can be arbitrarily close to the Fermi surface (due to the presence of the Λ^{-n} factor) and so should all contribute to Kondo screening.

This analysis suggests that in a situation with two electrons on the double dots which are bound into a triplet by a putative RKKY coupling, there are nonetheless (at least) three available screening channels, at least in the NRG reduction of the Anderson Hamiltonian. And so the problem would seem to be not one of an underscreened Kondo effect but an exactly screened Kondo effect. We do however note that while viewing the double dot system with two dot electrons as an exactly screened Kondo effect is consistent with our Fermi liquid findings, it is not clear under what conditions it would be correct to think of the two electron on the dots as ever forming a triplet. While any perturbatively generated RKKY interaction will generically be larger than the exponentially small Kondo screening scale, there is a question of whether the zero temperature perturbation theory underlying any RKKY estimate is convergent because the system is gapless.[156]

While we have focused here on NRG treatments of double dots close to their particle-hole symmetric point, similar analyses of any multi-dot system might suggest that whenever the dot degrees of freedom exceed $S = 1/2$, it is not possible to ignore the $p \neq 0$ modes of the logarithmic basis.

In the next chapter we will show that a completely different technique known as the 1/N expansion also favors the prediction that the ground state of closely spaced double quantum dots are Fermi liquids.

Chapter 7

$1/N$ diagrammatic expansion for coupled parallel quantum dots

7.1 Introduction

Strong correlations in impurity problems have been of tremendous theoretical and experimental interest. The physics of strongly correlated systems can be systematically studied via a system of quantum dots. This mesoscopic setup of dots forms an ideal platform for studying and comparing various low-dimensional techinques. As mentioned in the previous chapter, the experimental ability to adjust the gate voltages which control both the tunneling amplitudes between the dots and the connecting leads and the dots' chemical potential makes this a very preferable system for probing strongly correlated physics (for example, see realization of Kondo physics in a single quantum dot in Refs. [107–110]).

With the ability to engineer multi-quantum dot systems one can now realize more exotic forms of Kondo physics and effects of the Ruderman-Kittel-Kasuya-Yosida (RKKY) interaction. There has been experimental and theoretical progress in studying quantum dots both in series and in parallel. Despite considerable literature on the subject much is left to be understood.

In this chapter we focus on the system of quantum dots in parallel without direct tunneling or interaction between the dots. Although the dots are not directly coupled, they are coupled through an effective RKKY interaction. Our calculations will help us explore the nature of the RKKY interaction in

parallel double quantum dots. We will argue that the RKKY interaction is non-ferromagnetic due to its non-perturbative nature. The method we are going to use is a systematic diagrammatic expanion in $1/N$ where N is the degeneracy of the dot level. When applicable we will compare it with a recent Bethe ansatz and a slave boson mean field analysis for the same geometry (also see chapter 6). The method of $1/N$ expansion helps us to compute quantities such as zero temperature conductance and dot-occupancy. We find that the conductance vanishes at the particle-hole symmetric point and we can argue that the ground state is a Fermi-liquid.

The chapter is organized as follows. In Secion 7.2 we describe the double-dot model we are interested in studying and we will briefly describe the method we used. In Section 7.3 we will write down our results for the Green's function matrix, partition function, dot occupancy and conductance. In this section we will also show that the Friedel Sum Rule holds perturbatively in $1/N$ and we will use this fact to compute the conductance from the dot-occupancy. Lastly, in Section 7.4 we will discuss the implications of our results and make a comparision with other low-dimensional techniques on the same geometry.

7.2 Model studied and method used

The model we are interested in is given in Fig. 6.1. The Hamiltonian for this system is given by

$$\begin{aligned} H &= -i\sum_{l\sigma}\int_{-\infty}^{+\infty} dx c^{\dagger}_{l\sigma}\partial_x c_{l\sigma} + \sum_{\sigma\alpha} V_{l\alpha}\left(c^{\dagger}_{l\sigma\alpha}d_{\sigma\alpha} + h.c\right) + \sum_{\sigma\alpha}\epsilon_{d\alpha}n_{\sigma\alpha} \\ &+ \sum_{\alpha} U_{\alpha} n_{\uparrow\alpha} n_{\downarrow\alpha} \end{aligned} \tag{7.1}$$

The $c_{l\sigma}$ specify electrons with spin σ living on the two leads, $l = 1, 2$. The $d_{\alpha\sigma}$ specify electrons found on the two dots $\alpha = 1, 2$. Electrons can hop from the leads to dots with tunneling strength $V_{l\alpha}$. The strength of the Coulomb repulsion on the two dots is given by U_{α}. We suppose that there is no interdot Coulomb repulsion and that tunneling between the two dots is negligible. The starting point is the Hamiltonian (7.1) and we will study here

the $U_\alpha = \infty$ case. The constraint of preventing double-occupancy on the dots is fulfilled by introducing two Lagrange multipliers λ_1 and λ_2. The slave boson formalism consists of writing the impurity fermionic operator on each dot as a combination of a pseudofermion and a boson operator: $d_{\sigma\alpha} = b^\dagger_\alpha f_{\sigma\alpha}$. Here $f_{\sigma\alpha}$ is the pseudofermion which annihilates one "occupied state" on dot α and $b^\dagger_\alpha$ is a bosonic operator which creates an empty state on dot α. Instead of doing a mean field approximation we will instead do a systematic diagrammatic expansion in $1/N$ where N is the degeneracy of each dot. Under the slave boson formalism the double dot Hamiltonian (7.1) reads,

$$H = -i\sum_{l\sigma}\int_{-\infty}^{+\infty} dx c^\dagger_{l\sigma}\partial_x c_{l\sigma} + \sum_{\sigma\alpha} V_{l\alpha}\left(c^\dagger_{l\sigma\alpha} b^\dagger_\alpha f_{\sigma\alpha} + h.c\right) + \sum_{\sigma\alpha}\epsilon_{d\alpha} n_{\sigma\alpha} + \sum_\alpha i\lambda_\alpha (b^\dagger_\alpha b_\alpha + \sum f^\dagger_{\sigma\alpha} f_{\sigma\alpha} - 1)$$

and we will introduce,

$$H_{mix} = \sum_{\sigma\alpha} V_{l\alpha}\left(c^\dagger_{l\sigma\alpha} b^\dagger_\alpha f_{\sigma\alpha} + h.c\right)$$

To make Feynman diagrams we use the most general definition for Green's function,

$$G_{\alpha,\beta} = \frac{< b^\dagger_\alpha(\tau) f_{\sigma\alpha}(\tau) f^\dagger_{\sigma\beta}(0) b_\beta(0) e^{-\int_0^\beta H_{mix}(\tau)d\tau} >_0}{< e^{-\int_0^\beta H_{mix}(\tau)d\tau} >_0} \tag{7.2}$$

From (7.2) we see that $G_{\alpha\beta}$ is a matrix in the dot-space. All the diagrams (connected and disconnected) are constructed by the basic principle and the constraint was imposed on numerator and denominator separately. The subscript 0 in (7.2) denotes the ground state of the non-interacting system.

In this chapter we deal with arbitrary couplings $V_{l\alpha}$ however respecting the following ratio condition,

$$\frac{V_{1\alpha}}{V_{2\alpha}} = \frac{V_{1\alpha'}}{V_{2\alpha'}} = \lambda \tag{7.3}$$

This ratio condition helps us to map this Hamiltonian to even and odd channels, $c_{e/o} = (V_{1/2,\alpha} c_1 \pm V_{2/1,\alpha} c_2)/\sqrt{2\Gamma_\alpha}$ where $\Gamma_\alpha = (V^2_{1\alpha} + V^2_{2\alpha})/2$. Under

the map, the Hamiltonian factorizes into even and odd sectors:

$$\begin{aligned}\mathcal{H}_e &= -i\sum_{l\sigma}\int_{-\infty}^{\infty} dx\ c^{\dagger}_{e\sigma}\partial_x c_{e\sigma} + \sum_{\sigma\alpha}\sqrt{2\Gamma_\alpha}(c^{\dagger}_{e\sigma\alpha}d_{\sigma\alpha} + \text{h.c}) \\ &\quad + \sum_{\sigma\alpha}\epsilon_{d\alpha}n_{\sigma\alpha} + \sum_{\alpha}U_\alpha n_{\uparrow\alpha}n_{\downarrow\alpha}; \\ \mathcal{H}_o &= -i\sum_{l\sigma}\int_{-\infty}^{\infty} dx\ c^{\dagger}_{o\sigma}\partial_x c_{o\sigma}, \end{aligned} \tag{7.4}$$

where, as can be seen, the odd sector decouples from the double dot. For convenience we will make the replacement $\sqrt{2\Gamma_{1,2}} \to \sqrt{\Gamma_{1,2}}$.

7.3 Results

7.3.1 Greens Function Matrix

In this section we first start with the results for the Green's function matrix. We are interested in those terms of the matrix that will be further used to show that Friedel Sum Rule holds perturbatively in 1/N.

The Green's function takes the form

$$G = \begin{bmatrix} G_{11}^{O(1)+O(\frac{1}{N})} & G_{12}^{O(\frac{1}{N})+O(\frac{1}{N^2})} \\ G_{21}^{O(\frac{1}{N})+O(\frac{1}{N^2})} & G_{22}^{O(1)+O(\frac{1}{N})} \end{bmatrix}$$

We will introduce the following notations.

$$\Sigma_{1,2}(z) = N\Gamma_{1,2}\sum_k \frac{f_k}{z+\epsilon_k-\epsilon_{d_{1,2}}} \tag{7.5}$$

$$Z_{1,2}[E_{01,02}] = \left[1 - \frac{\partial\Sigma_{1,2}}{\partial z}\right]^{-1}|_{z=E_{01,02}}$$

The entries of the matrix are then as follows.

$$G_{11}^{O(1)}(i\omega_n) = \frac{Z_1(E_{01})}{i\omega_n - T_{A_1}} \tag{7.6}$$

$$G_{12}^{0(\frac{1}{N})}(i\omega_n) = \frac{Z_1(E_{01})}{i\omega_n - T_{A_1}} \cdot \left[-i\left(V_{11}V_{12} + V_{21}V_{22}\right)\right] \cdot \frac{Z_2(E_{02})}{i\omega_n - T_{A_2}} \tag{7.7}$$

In Eq (7.6 and 7.7) one can swap the subscript $1 \leftrightarrow 2$ to get the corresponding expressions for $G_{22}^{O(1)}(i\omega_n)$ and $G_{21}^{O(\frac{1}{N})}(i\omega_n)$. Notice that Eq (7.6 and 7.7) are the lowest order diagrams in $1/N$ for the matrix entries.

Here ϵ_k denotes the energy of the conduction state and f_k denotes the fermi-function, ie, $f_k = \frac{1}{e^{\beta k}+1}$.One can easily notice from (7.5) that

$$Re\Sigma_{1,2}(\omega) = \frac{N\left(V_{11,12}^2 + V_{21,22}^2\right)}{\pi} Log\left|\frac{\epsilon_{d_{1,2}} - \omega}{D}\right|$$

and we can also easily see that, $Im\Sigma_{1,2}(\omega) = 0$ if $\omega < \epsilon_{d_{1,2}}$ and $Im\Sigma_{1,2}(\omega) = -N\left(V_{11,12}^2 + V_{21,22}^2\right)$ otherwise. It is to be noted that $E_{01,2}$ is the most negative solution of $\omega - Re\Sigma_{1,2}(\omega) = 0$ and,

$$T_{A_{1,2}} = \epsilon_{d_{1,2}} - E_{01,2}$$

We write down results for next-to-leading order here.

$$Im\left[G_{11}^{O(1/N)}\right] = -\frac{Z^2\Gamma_1}{\left(\omega - T_{A_1}\right)^2} - \pi\theta(-\omega - T_{A_1})R(\omega) - \pi\theta(\omega - T_{A_1})\left[S(\omega) + T(\omega)\right] \tag{7.8}$$

The definitions of $S(\omega)\,, R(\omega)$and $T(\omega)$ used in (7.8) are as follows

$$R(\omega) = \frac{Z_1(E_{01})}{N}\left[\frac{N\Gamma_1}{\pi}\right]^2 \int_{T_{A_1}}^{-\omega} \frac{dk}{\left(\omega + \epsilon_k - T_{A_1}\right)^2} \frac{1}{\left(\epsilon_k - \left(\frac{N\Gamma_1}{\pi}\right)\log(\frac{\epsilon_k}{T_{A_1}} - 1)\right)^2 + (N\Gamma)^2} \tag{7.9}$$

$$S(\omega) = \frac{Z_1(E_{01})}{N}\left[\frac{N\Gamma_1}{\pi}\right]^2 \frac{1}{\left(\omega - T_{A_1}\right)^2} \int_{T_{A_1}}^{\omega} \frac{dk}{\left(\epsilon_k - \left(\frac{N\Gamma_1}{\pi}\right)\log(\frac{\epsilon_k}{T_{A_1}} - 1)\right)^2 + (N\Gamma_1)^2} \tag{7.10}$$

$$T(\omega) = \frac{Z_1(E_{01})}{N}\left[\frac{N\Gamma_1}{\pi}\right]^2\left[\frac{1}{T_{A_1}} - \frac{1}{\omega}\right]\frac{1}{\left[\omega - T_{A_1} + \left(\frac{N\Gamma_1}{\pi}\right)\log(\frac{\omega}{T_{A_1}})\right]^2} \tag{7.11}$$

As has been pointed out before $G_{22}^{O(1/N)}$ is obtained by just interchanging the species index $1 \leftrightarrow 2$. It is important to notice for future that

$$Im\left[G_{11}^{O(1/N)}(\omega = 0)\right] = -\frac{Z_1(E_{01})^2\Gamma_1}{(\omega - T_{A_1})^2} \tag{7.12}$$

and we also have from Eq. (7.7) that

$$Im[G_{12}^{0(\frac{1}{N})}(\omega = 0)] = -\frac{Z_1(E_{01})}{\omega - T_{A_1}} \cdot [(V_{11}V_{12} + V_{21}V_{22})] \cdot \frac{Z_2(E_{02})}{\omega - T_{A_2}} \tag{7.13}$$

For the sake of brevity we donot presents expressions for those parts of the Green's function matrix that are extraneous to the main goal which is to provide strong evidence of a Fermi-Liquid by perturbatively showing that the Friedel Sum Rule holds.

7.3.2 Partition function and dot-occupancy

We present here results of the partition function from diagrams from which one can also extract the dot occupancy. The partition function and the dot occupancy obey the simple relation

$$n_{d1,2} = -\frac{1}{\beta}\frac{\partial \log Z}{\partial \epsilon_{d1,2}} \tag{7.14}$$

It turns out that the partition function is given by

$$Z = e^{-\beta E_{01}} \cdot e^{-\beta E_{02}} \tag{7.15}$$

From this its trivial to see that $n_{d1,2} = \frac{\partial E_{01,2}}{\partial \epsilon_{d1,2}}$. After some algebra one finds

$$n_{d1,2} = \frac{\mu_{1,2}}{1 + \mu_{1,2}} \tag{7.16}$$

where

$$\mu_{1,2} = \frac{N\Gamma_{1,2}}{\pi T_{A1,2}} \tag{7.17}$$

It should be again noted that while Greens function was computed upto O(1/N) it suffices (as far as proving FSR perturbatively is concerned) to compute dot occupancy upto O(1). Higher order corrections to the dot occupancy are extraneous to the main goal of the chapter.

7.3.3 Friedel Sum Rule (FSR) for double quantum dots

7.3.3.1 Friedel Sum Rule.

FSR states for N-fold degeneracy that

$$\delta(0) = \frac{\pi n_f}{N} \tag{7.18}$$

Another and more convenient way of writing the FSR is through linear conductance

$$\sigma(\omega = 0) = 2\frac{e^2}{h}\frac{4\lambda^2}{(1+\lambda^2)^2}\sin^2\left(\frac{\pi n_f}{N}\right) \tag{7.19}$$

Also following Meir and Wingreen [157]we have the most general expression for linear conductance as

$$\sigma(\omega = 0) = -2\frac{e^2}{h}\frac{2}{(1+\lambda^2)}\mathrm{Im}[\mathrm{Tr}\left\{\Gamma_L G^r\right\}] \tag{7.20}$$

where G^r is the full retarded Green's function matrix in dot-space and Γ_L is the bare hybridization matrix both defined as

$$G^r = \begin{bmatrix} G^r_{11} & G^r_{12} \\ G^r_{21} & G^r_{22} \end{bmatrix} \tag{7.21}$$

$$\Gamma_L = \begin{bmatrix} V_{11}^2 & V_{11}V_{12} \\ V_{11}V_{12} & V_{12}^2 \end{bmatrix} \tag{7.22}$$

Thus to show that FSR holds we need to show that a perturbative expansion in (7.19) is equal to a perturbative expansion in (7.20) ,ie, we have to show that perturbatively

$$2\frac{e^2}{h}\frac{4\lambda^2}{(1+\lambda^2)^2}\sin^2\left(\frac{\pi n_f}{N}\right) = -2\frac{e^2}{h}\frac{2}{(1+\lambda^2)}\mathrm{Im}[\mathrm{Tr}\left\{\Gamma_L G^r\right\}] \tag{7.23}$$

7.3.3.2 Proof that FSR is satisfied perturbatively for double quantum dots

The left hand side of (7.23) to $O(\frac{1}{N^2})$ is equal to

$$\begin{aligned}\frac{4\lambda^2}{(1+\lambda^2)^2}\sin^2\left(\frac{\pi n_f}{N}\right) &= \frac{4\lambda^2}{(1+\lambda^2)^2}\sin^2\left(\frac{\pi\left(n_{f1}+n_{f2}\right)}{N}\right)\\ &\approx \frac{4\lambda^2}{(1+\lambda^2)^2}\frac{\pi^2}{N^2}\Big\{n_{f1}^{2\mathrm{O}(1)} + n_{f2}^{2\mathrm{O}(1)}\\ &+ 2n_{f1}^{\mathrm{O}(1)}n_{f2}^{\mathrm{O}(1)}\Big\}\end{aligned} \tag{7.24}$$

The right hand side of (7.23) to the same order, ie , $O(\frac{1}{N^2})$ gives

$$\begin{aligned}\frac{2}{(1+\lambda^2)}\text{-}\mathrm{Im}[\mathrm{Tr}\left\{\Gamma_L G^r\right\}] &\approx -\frac{2}{(1+\lambda^2)}\mathrm{Im}\Big\{V_{11}^2 G_{11}^{\mathrm{O(1/N)}} + V_{11}V_{12}G_{21}^{\mathrm{O(1/N)}}\\ &+ V_{11}V_{12}G_{12}^{\mathrm{O(1/N)}} + V_{12}^2 G_{22}^{\mathrm{O(1/N)}}\Big\}\end{aligned} \tag{7.25}$$

where all the Greens's functions were evaluated by diagrammatic approach. We indeed find that the FSR (7.23) holds for double-dots perturbatively.

7.3.3.3 Evaluation of conductance using FSR and $1/N$ diagrams

Since we showed that FSR holds perturbatively in $1/N$ we will use Eq(7.19) to compute the linear conductance, ie,

$$\sigma(\omega=0) = 2\frac{e^2}{h}\frac{4\lambda^2}{(1+\lambda^2)^2}\sin^2\left(\frac{\pi\left[n_{d_1}+n_{d_2}\right]}{N}\right) \tag{7.26}$$

where n_{d_1} and n_{d_2} are calculated from diagrams of partition function z, ie,

$$n_{d_{1,2}} = -\frac{1}{\beta}\frac{\partial\log z}{\partial\epsilon_{f_{1,2}}} \tag{7.27}$$

7.4 Discussions and Conclusions

In this chapter we have studied a double-impurity model using the well-known technique of $1/N$ expansion where N is the degeneracy of each dot level. We computed the entries of the Green's function matrix. We also computed the dot occupancy after evaluating the diagrams of the partition function. With the knowledge that FSR is satisfied for this system of closely spaced dots we compute the linear conductance from the dot occupancy. We find that the conductance vanishes at the particle-hole symmetric point and the results are in agreement with a slave boson mean field theory of the same system. Thus we find evidence that the ground state of a system of double dots is a Fermi-liquid singlet. The RKKY interaction in this case is clearly non-ferromagnetic in nature and this is due to the non-perturbative nature of the problem. These findings are consistent with a Bethe-Ansatz and slave boson mean field analysis of the same system. However, we note that there are discrepancies between our results and the results stemming from the method of the Numerical Renormalization Group. Possible reasons for these discrepancies were mentioned in Chapter 6.

Bibliography

[1] J. Joseph, J. E. Thomas, M. Kulkarni, and A. G. Abanov, *Observation of shock waves in a strongly interacting fermi gas.*, *Phys. Rev. Lett.* **106** (2011) 150401.

[2] Z.-Q. Ma and C. N. Yang, *Spin 1/2 fermions in 1d harmonic trap with repulsive delta function interparticle interaction.*, *Chinese Physics Letters.* **27** (2010) 080501.

[3] R. M. Konik, *Transport properties of multiple quantum dots arranged in parallel: results from the bethe ansatz*, *New J. Phys.* **9** (2007) 257.

[4] Z. Dutton, M. Budde, C. Slowe, and L. V. Hau, *Observation of quantum shock waves created with ultra- compressed slow light pulses in a bose-einstein condensate.*, *Science* **293** (2001) 5530.

[5] L. Khaykovich, F. Schreck, G. Ferrari, T. Bourdel, J. Cubizolles, L. D. Carr, Y. Castin, and C. Salomon, *Formation of a matter-wave bright soliton.*, *Science* **298** (2002) 5571.

[6] T. P. Simula, P. Engels, I. Coddington, V. Schweikhard, E. A. Cornell, and R. J. Ballagh, *Observations on sound propagation in rapidly rotating bose-einstein condensates.*, *Phys. Rev. Lett.* **94** (2005) 080404.

[7] R. Meppelink, S. B. Koller, J. M. Vogels, P. van der Straten, E. D. van Ooijen, N. R. Heckenberg, H. Rubinsztein-Dunlop, S. A. Haine, and M. J. Davis *Phys. Rev. A.* **80** (2009) 043606.

[8] K. M. O'Hara, S. L. Hemmer, M. E. Gehm, S. R. Granade, and J. E. Thomas, *Observation of a strongly interacting degenerate fermi gas of atoms.*, *Science* **298** (2002) 2179.

[9] J. Joseph, B. Clancy, L. Luo, J. Kinast, A. Turlapov, and J. E. Thomas, *Measurement of sound velocity in a fermi gas near a feshbach resonance.*, *Phys. Rev. Lett.* **98** (2007) 170401.

[10] X. Du, L. Luo, B. Clancy, and J. E. Thomas, *Observation of anomalous spin segregation in a trapped fermi gas.*, *Phys. Rev. Lett.* **101** (2008) 150401.

[11] X. Du, Y. Zhang, J. Petricka, and J. E. Thomas, *Controlling spin current in a trapped fermi gas.*, *Phys. Rev. Lett.* **103** (2009) 010401.

[12] J. T. Stewart, J. P. Gaebler, T. E. Drake, and D. S. Jin, *Verification of universal relations in a strongly interacting fermi gas.*, *Phys. Rev. Lett.* **104** (2010) 235301.

[13] J. Monaghan *Computer Physics Communications* **48** (1988) 88.

[14] J. J. Monaghan, *Smoothed particle hydrodynamics*, *Annual review of astronomy and astrophysics* **30** (1992) 543.

[15] M. Kulkarni, F. Franchini, and A. G. Abanov, *Nonlinear dynamics of spin and charge in spin-calogero model.*, *Phys. Rev. B.* **80** (2009) 165105.

[16] A. P. Polychronakos, *Waves and solitons in the continuum limit of the calogero-sutherland model.*, *Phys. Rev. Lett* **74** (1995) 5153.

[17] I. Andric, V. Bardek, and L. Jonke, *Solitons in the calogero-sutherland collective-field model.*, *Phys. Lett. B* **357** (1995) 374.

[18] A. G. Abanov, A. Gromov, and M. Kulkarni, *Soliton solutions of calogero model in harmonic potential.*, *arXiv:1103.6231* (2011).

[19] P. F. Kolb and U. Heinz, *Quark Gluon Plasma 3*, p. 634. World Scientific, 2003.

[20] K. M. O'Hara, S. L. Hemmer, M. E. Gehm, S. R. Granade, and J. E. Thomas, *Observation of a strongly interacting degenerate Fermi gas of atoms*, *Science* **298** (2002) 2179.

[21] J. E. Thomas and M. E. Gehm, *Optically trapped Fermi gases*, *Am. Scientist* **92** (2004) 238.

[22] J. Kinast, A. Turlapov, and J. E. Thomas, *Damping of a unitary Fermi gas*, *Phys. Rev. Lett.* **94** (2005) 170404.

[23] M. Bartenstein, A. Altmeyer, S. Riedl, S. Jochim, C. Chin, J. H. Denschlag, and R. Grimm, *Collective excitations of a degenerate Fermi gas at the BEC-BCS crossover*, *Phys. Rev. Lett.* **92** (2004) 203201.

[24] J. Joseph, B. Clancy, L. Luo, J. Kinast, A. Turlapov, and J. E. Thomas, *Measurement of sound velocity in a Fermi gas near a feshbach resonance*, *Phys. Rev. Lett.* **98** (2007) 170401.

[25] B. Clancy, L. Luo, and J. E. Thomas, *Observation of nearly perfect irrotational flow in normal and superfluid strongly interacting Fermi gases*, *Phys. Rev. Lett.* **99** (2007) 140401.

[26] M. Bartenstein, A. Altmeyer, S. Riedl, R. Geursen, S. Jochim, C. Chin, J. H. Denschlag, R. Grimm, A. Simoni, E. Tiesinga, C. J. Williams, and P. S. Julienne, *Precise determination of ^{6}Li cold collision parameters by radio-frequency spectroscopy on weakly bound molecules*, *Phys. Rev. Lett.* **94** (2005) 103201.

[27] H. Heiselberg, *Fermi systems with long scattering lengths*, *Phys. Rev. A* **63** (2001) 043606.

[28] L. Luo and J. E. Thomas, *Thermodynamic measurements in a strongly interacting Fermi gas*, *J. Low Temp. Phys.* **154** (2009) 1.

[29] V. E. Zakharov and E. A. Kuznetsov, *Hamiltonian formalism for nonlinear waves*, *Physics Uspekhi* **40** (1997) 1087.

[30] C. Cao, E. Elliott, J. Joseph, H. Wu, T. S. J. Petricka, and J. E. Thomas, *Universal quantum viscosity in a unitary fermi gas*, *Science DOI: 10.1126/science.1195219* (2010).

[31] L. D. Landau and E. M. Lifshitz, *Fluid Mechanics*. Pergamon Press, New York, 1975.

[32] L. Landau, *An Introduction to the Theory of Superfluidity.* Addison-Wesley, New York, 1989.

[33] P. Capuzzi, P. Vignolo, F. Federici, and M. P. Tosi, *Sound propagation in elongated superfluid fermionic clouds*, *Phys. Rev. A* **73** (2006) 021603(R).

[34] G. Bertaina, L. Pitaevskii, and S. Stringari *Phys. Rev. Lett.* **105** (2010) 150402.

[35] C. Menotti, P. Pedri, and S. Stringari, *Expansion of an interacting fermi gas.*, *Phys. Rev. Lett.* **89** (2002) 250402.

[36] S. Giorgini, L. Pitaevskii, and S. Stringari *Rev. Mod. Phys.* **80** (2008) 1215.

[37] M. A. Hoefer, M. J. Ablowitz, I. Coddington, E. A. Cornell, P. Engels, and V. Schweikhard *Phys. Rev. A.* **74** (2006) 023623.

[38] F. D. M. Haldane, *'luttinger liquid theory' of one-dimensional quantum fluids: I. properties of the luttinger model and their extension to the general 1d interacting spinless fermi gas*, *J. Phys. C Solid State* **14** (1981) 2585.

[39] S. Brazovskii, S. Matveenko, and P. Nozières, *Spin excitations carry charge currents: one-dimensional hubbard model.*, *J. Phys. I* **4** (1994) 571.

[40] A. P. Polychronakos, *Exchange operator formalism for integrable systems of particles.*, *Phys. Rev. Lett.* **69** (1994) 703.

[41] Z. N. C. Ha and F. D. M. Haldane, *Models with inverse-square exchange.*, *Phys. Rev. B* **46** (1992) 9359.

[42] K. Hikami and M. Wadati, *Integrable spin-1/2 particle systems with long-range interactions.*, *Phys. Lett. A* **173** (1993) 263.

[43] B. Sutherland, *Beautiful Models. 10 Years of Exactly Solved Quantum Many-Body Problems.* World Scientific, Singapore, 2004.

[44] F. D. M. Haldane, *Fractional statistics in arbitrary dimensions - a generalization of the pauli principle.*, *Phys. Rev. Lett.* **67** (1991) 937.

[45] T. Fukui and N. Kawakami, *Fractional statistics in arbitrary dimensions - a generalization of the pauli principle.*, *Phys. Rev. B* **51** (1995) 5239.

[46] Y. Kato and Y. Kuramoto, *Fractional exclusion statistics for the multicomponent sutherland model.*, *J. Phys. Soc. Jpn.* **65** (1996) 77.

[47] A. Polychronakos., *Generalized statistics in one dimension.*, *Les Houches Lectures, Summer , arXiv:hep-th/9902157* (1999).

[48] Y. Kato, T. Yamamoto, and M. Arikawa, *Elementary excitations and dynamical correlation functions of the calogero-sutherland model with internal symmetry.*, *J. Phys. Soc. Jpn.* **66** (1997) 1954.

[49] H. Awata, Y. Matsuo, S. Odake, and J. Shiraishi, *Collective field theory, calogero-sutherland model and generalized matrix models.*, *Phy Lett B* **347** (1995) 49.

[50] H. Awata, Y. Matsuo, S. Odake, and J. Shiraishi, *Excited states of the calogero-sutherland model and singular vectors of the wn algebra.*, *Nucl Phys B* **449** (1995) 347.

[51] I. Andric, A. Jevicki, and H. Levine, *On the large-n limit in symplectic matrix models.*, *Nucl Phys B* **215** (1983) 307.

[52] I. Andric and V. Bardek, *1/n corrections in calogero-type models using the collective-field method.*, *J. Phys A* **21** (1988) 2847.

[53] A. G. Abanov and P. B. Wiegmann, *Quantum hydrodynamics, the quantum benjamin-ono equation, and the calogero model.*, *Phys. Rev. Lett* **95** (2005) 076402.

[54] H. Awata, Y. Matsuo, and T. Yamamoto, *Collective field description of spin calogero-sutherland models.*, *J. Phys. A* **29** (1996) 3089.

[55] I. Aniceto and A. Jevicki, *Notes on collective field theory of matrix and spin calogero models.*, *J. Phys. A: Math. Gen.* **39** (2006) 12765.

[56] G. B. Whitham, *Linear and Nonlinear Waves.* Wiley-Interscience, New York, 1999.

[57] A. P. Polychronakos, *Lattice integrable systems of haldane-shastry type.*, *Phys. Rev. Lett.* **70** (1993) 2329.

[58] A. Jevicki and B. Sakita, *The quantum collective field method and its application to the planar limit.*, *Nucl. Phys. B.* **165** (1980) 511.

[59] B. Sakita, *Quantum Theory of Many-variable Systems and Fields.* World Scientific, Singapore, 1985.

[60] A. Jevicki, *Nonperturbative collective field theory.*, *Nucl. Phys. B* **376** (1992) 75.

[61] M. Schick, *Flux quantization in a one-dimensional model.*, *Phys. Rev.* **404** (1968) 1968.

[62] D. Schmeltzer, *Bosonization in one and two dimensions.*, *Phys. Rev. B* **47** (1993) 11980.

[63] B. Sutherland and B. S. Shastry, *Solution of some integrable one-dimensional quantum systems.*, *Phys. Rev. Lett.* **71** (1993) 5.

[64] Y. Kato and Y. Kuramoto, *Exact solution of the sutherland model with arbitrary internal symmetry.*, *Phys. Rev. Lett.* **74** (1995) 1222.

[65] A. G. Abanov, *Hydrodynamics of correlated systems and spacing distribution in random matrices.*, *arXiv:cond-mat/0504307* (2005).

[66] F. D. M. Haldane, *Exact jastrow-gutzwiller resonating-valence-bond ground state of the spin-1/2 antiferromagnetic heisenberg chain with $1/r^2$ exchange.*, *Phys. Rev. Lett.* **60** (1988) 635.

[67] B. S. Shastry, *Exact solution of an s=1/2 heisenberg antiferromagnetic chain with long-ranged interactions.*, *Phys. Rev. Lett.* **60** (1988) 639.

[68] V. Bardek, J. Feinberg, and S. Meljanac, *Collective field formulation of the multi-species calogero model and its duality symmetries.*, *Nucl. Phys. B.* **767** (2007) 295.

[69] F. Franchini and M. Kulkarni, *Emptiness and depletion formation probability in spin models with inverse square interaction.*, *Nuclear Physics B.* **825** (2010) 320.

[70] F. Franchini and A. G. Abanov, *Emptiness formation probability for the anisotropic xy model in a magnetic field.*, *J. Phys. A: Math. Gen.* **38** (2005) 5069.

[71] A. G. Abanov, E. Bettelheim, and P. Wiegmann, *Integrable hydrodynamics of calogero-sutherland model: bidirectional benjamin-ono equation.*, *J. Phys. A: Math. Theor.* **42** (2009) 135201.

[72] W. Ketterle and M. Zwierlein, *Making, probing and understanding ultracold fermi gases.*, *Proceedings of the International School of Physics, Enrico Fermi, Course CLXIV, Varenna* (2006).

[73] E. Bettelheim, A. G. Abanov, and P. Wiegmann, *Nonlinear quantum shock waves in fractional quantum hall edge states.*, *Phys. Rev. Lett.* **97** (2006) 246401.

[74] R. Meppelink, S. B. Koller, J. M. Vogels, P. van der Straten, E. D. van Ooijen, N. R. Heckenberg, H. Rubinsztein-Dunlop, S. A. Haine, and M. J. Davis, *Observation of shock waves in a large bose-einstein condensate.*, *Phys. Rev. A.* **80** (2009) 043606.

[75] M. R. Andrews, D. M. Kurn, H.-J. Miesner, D. S. Durfee, C. G. Townsend, S. Inouye, and W. Ketterle, *Propagation of sound in a bose-einstein condensate.*, *Phys. Rev. Lett.* **79** (1997) 553.

[76] M. Stone, *Bosonization.* World Scientific, Singapore, 1994.

[77] A. Recati, P. Fedichev, W. Zwerger, and P. Zoller, *Spin-charge separation in ultracold quantum gases.*, *Phys. Rev. Lett.* **90** (2003) 020401.

[78] L. Kecke, H. Grabert, and W. Hausler, *Charge and spin dynamics of interacting fermions in a one-dimensional harmonic trap.*, *Phys. Rev. Lett.* **94** (2005) 176802.

[79] M. Polini and G. Vignale, *Spin drag and spin-charge separation in cold fermi gases.*, *Phys. Rev. Lett.* **98** (2007) 266403.

[80] C. Kollath, U. Schollwock, and W. Zwerger, *Spin-charge separation in cold fermi gases: A real time analysis.*, *Phys. Rev. Lett.* **95** (2005) 176401.

[81] W. Li, G. Xianlong, C. Kollath, and M. Polini, *Collective excitations in one-dimensional ultracold fermi gases: Comparative study.*, *Phys. Rev. B.* **78** (2008) 195109.

[82] G. Xianlong, *Effects of interaction and polarization on spin-charge separation: A time-dependent spin-density-functional theory study.*, *Phys. Rev. B.* **81** (2010) 104306.

[83] Y. Kuramoto and Y. Kato, *Dynamics of One-Dimensional Quantum Systems: Inverse-Square Interaction Models.* Cambridge University Press, 2009.

[84] K. Hikami, *Symmetry of the calogero model confined in the harmonic potential-yangian and w algebra.*, *J. Phys. A: Math. Gen.* **28** (1995) L131.

[85] C. N. Yang, *Some exact results for the many-body problem in one dimension with repulsive delta-function interaction.*, *Phys. Rev. Lett.* **19** (1967) 1312.

[86] V. Korepin, N. Bogoliubov, and A. Izergin, *Quantum Inverse Scattering Mehod and Correlation Functions.* Cambridge University Press, 1993.

[87] M. Shiroishi, M. Takahashi, and Y. Nishiyama, *Emptiness formation probability for the one-dimensional isotropic xy model.*, *J. Phys. Soc. Jap.* **70** (2001) 3535.

[88] F. Franchini, *On hydrodynamic correlations in low-dimensional interacting systems.*, *arXiv:0801.2734 (Ph.D. thesis, Stony Brook University)* (2006).

[89] A. Abanov and F. Franchini, *Emptiness formation probability for the anisotropic xy spin chain in a magnetic field.*, *Phys. Lett. A.* **316** (2003) 342.

[90] N. Kitanine, J. Maillet, N. Slavnov, and V. Terras, *Large distance asymptotic behaviour of the emptiness formation probability of the xxz spin-$\frac{1}{2}$ heisenberg chain.*, *J. Phys. A: Math. Gen.* **35** (2002) L753.

[91] V. Korepin, S. Lukyanov, Y. Nishiyama, and M. Shiroishi, *Asymptotic behavior of the emptiness formation probability in the critical phase of xxz spin chain.*, *Phys. Lett. B* **312** (2003) 21.

[92] K. Kozlowski, *On the emptiness formation probability of the open xxz spin-$\frac{1}{2}$ chain.*, *J. Stat. Mech.* **0802** (2008) 2006.

[93] F. Colomo and A. Pronko, *The arctic circle revisited.*, *Cont. Math.* **458** (2008) 361.

[94] F. Colomo and A. Pronko, *Emptiness formation probability in the domain-wall six-vertex model.*, *Nucl. Phys. B.* **798** (2008) 340.

[95] F. Colomo and A. Pronko, *The limit shape of large alternating sign matrices.*, *arXiv:0803.2697* (2008).

[96] T. Deguchi and C. Matsui, *Emptiness formation probability of the integrable higher-spin xxx and xxz spin chains through the fusion method.*, *arXiv:0907.0582* (2009).

[97] J. Stolze and T. Garske, *The emptiness formation probability correlation in homogeneous and dimerized xx chains.*, *arXiv:0904.3519* (2009).

[98] Z. Tsuboi and M. Shiroishi, *High temperature expansion of the emptiness formation probability for the isotropic heisenberg chain.*, *J. Phys. A: Math. Gen.* **38** (2005) 363.

[99] Z. Tsuboi, *A note on the high temperature expansion of the density matrix for the isotropic heisenberg chain.*, *Physica* **377** (2007) 95.

[100] F. Gohmann, A. Klumper, and A. Seel, *Emptiness formation probability at finite temperature for the isotropic heisenberg chain.*, *Physica B* **807** (2005) 359.

[101] A. Abanov and V. Korepin, *On the probability of ferromagnetic strings in antiferromagnetic spin chains.*, *Nucl Phys B* **647** (2002) 565.

[102] M. Mehta, *Random Matrices.* New York: Academic Press, 1991.

[103] J. des Cloizeaux and M. Mehta, *Asymptotic behavior of spacing distributions for eigenvalues of random matrices.*, *J. Math. Phys* **14** (1973) 1648.

[104] F. Dyson, *Fredholm determinants and inverse scattering problems.*, *Commun. Math. Phys.* **47** (1976) 171.

[105] J. Keating, F. Mezzadri, and M. Novaes, *A new correlator in quantum spin chains.*, *J. Phys. A* **39** (2006) L389.

[106] T. Giamarchi, *Quantum Physics in One Dimension.* Oxford University Press, 2004.

[107] D. Goldhaber-Gordon, J. Göres, M. A. Kastner, H. Shtrikman, D. Mahalu, and U. Meirav, *From the kondo regime to the mixed-valence regime in a single-electron transistor.*, *Phys. Rev. Lett.* **81** (1998) 5225.

[108] D. Goldhaber-Gordon, H. Shtrikman, D. Mahalu, D. Abusch-Magder, U. Meirav, and M. A. Kastner, *Kondo effect in a single-electron transistor.*, *Nature* **391** (1998) 156.

[109] S. M. Cronenwett, T. H. Oosterkamp, and L. P. Kouwenhoven, *A tunable kondo effect in quantum dots.*, *Science* **540** (1998) 281.

[110] W. G. van der Wiel, S. D. Franceschi, T. Fujisawa, J. M. Elzerman, S. Tarucha, and L. P. Kouwenhoven, *The kondo effect in the unitary limit*, *Science* **289** (2000) 2105.

[111] R. M. Potok, I. G. Rau, H. Shtrikman, Y. Oreg, and D. Goldhaber-Gordon, *Observation of the two-channel kondo effect*, *Nature* **446** (2007) 167.

[112] M. Lee, M.-S. Choi, R. Lopez, R. Aguado, J. Martinek, and R. Zitko, *Two-impurity anderson model revisited: Competition between kondo effect and reservoir-mediated superexchange in double quantum dots*, *Physical Review B* **81** (2010) 121311.

[113] E. Sela and I. Affleck, *Resonant pair tunneling in double quantum dots*, *Phys. Rev. Lett.* **103** (2009) 087204.

[114] E. Sela and I. Affleck, *Nonequilibrium transport through double quantum dots: Exact results near a quantum critical point*, *Phys. Rev. Lett.* **102** (2009) 047201.

[115] I. Weymann, *Effects of different geometries on the conductance, shot noise, and tunnel magnetoresistance of double quantum dots*, *Phys. Rev. B* **78** (2009) 045310.

[116] J. Malecki, E. Sela, and I. Affleck, *Prospect for observing the quantum critical point in double quantum dot systems*, *Phys. Rev. B* **82** (2010) 205327.

[117] Y. Nisikawa and A. Oguri, *Transport through a double quantum dot with interdot repulsion*, *J. Phys.: Conf. Ser.* **150** (2009) 022066.

[118] R. M. Konik, *Kondo physics and exact solvability of double dots systems*, *Phys. Rev. Lett.* **99** (2007) 076602.

[119] R. Zitko and J. Bonca, *Quantum phase transitions in systems of parallel quantum dots*, *Phys. Rev. B* **76** (2007) 241305.

[120] R. Zitko and J. Bonca, *Multiple-impurity anderson model for quantum dots coupled in parallel*, *Phys. Rev. B* **74** (2006) 045312.

[121] C.-H. Chung and W. Hofstetter, *Kondo effect in coupled quantum dots with rkky interaction: Effects of finite temperature and magnetic field*, *Phys. Rev. B* **76** (2007) 045329.

[122] G.-H. Ding, F. Ye, and B. Dong, *Quantum phase transition and underscreened kondo effect in electron transport through parallel double quantum dots*, *J. Phys. Cond.-Matt.* **21** (2009) 455303.

[123] D. Guo-Hui and Y. Fei, *Quantum phase transition and ferromagnetic spin correlation in parallel double quantum dots*, *Chin. Phys. Lett.* **24** (2007) 2926.

[124] R. Lopez, D. Sanchez, M. Lee, M.-S. Choi, P. Simon, and K. L. Hur, *Probing spin and orbital kondo effects with a mesoscopic interferometer*, *Phys. Rev. B* **71** (2007) 115312.

[125] E. Vernek, N. Sandler, S. Ulloa, and E. Anda, *Kondo regime of a quantum dot molecule: A finite-u slave boson approach*, *Physica E* **34** (2006) 608.

[126] G.-H. Ding, C. K. Kim, , and K. Nahm, *Fano resonance in electron transport through parallel double quantum dots in the kondo regime*, *Phys. Rev. B* **71** (2005) 205313.

[127] L. G. G. V. D. da Silva, N. P. Sandler, K. Ingersent, and S. E. Ulloa, *Zero-field kondo splitting and quantum-critical transition in double quantum dots*, *Phys. Rev. Lett.* **97** (2006) 096603.

[128] L. G. G. V. D. da Silva, K. Ingersent, N. Sandler, and S. E. Ulloa, *Finite-temperature conductance signatures of quantum criticality in double quantum dots*, *Phys. Rev. B.* **78** (2008) 153304.

[129] E. Sela and I. Affleck, *Nonequilibrium critical behavior for electron tunneling through quantum dots in an aharonov-bohm circuit*, *Phys. Rev. B.* **79** (2009) 125110.

[130] J. P. Dahlhaus, S. Maier, and A. Komnik, *Spin-polarized current generation and detection by a double quantum dot structure*, *Phys. Rev. B.* **81** (2010) 075110.

[131] J. C. Chen, A. Chang, and M. R. Melloch, *Transition between quantum states in a parallel-coupled double quantum dot*, *Phys. Rev. Lett.* **92** (2004) 176801.

[132] M. Sigrist, A. Fuhrer, T. Ihn, K. Ensslin, S. E. Ulloa, W.Wegscheider, and M. Bichler, *Magnetic-field-dependent transmission phase of a*

double-dot system in a quantum ring, *Phys. Rev. Lett.* **93** (2004) 066802.

[133] A. M. Chang and J. C. Chen, *The kondo effect in coupled-quantum dots*, *Rep. Prog. Phys.* **72** (2009) 096501.

[134] A. W. Holleitner, A. Chudnovskiy, D. Pfannkuche, K. Eberl, and R. H. Blick, *Pseudospin kondo correlations versus hybridized molecular states in double quantum dots*, *Phys. Rev. B* **70** (2004) 075204.

[135] A. Hubel, K. Held, J. Weis, and K. V. Klitzing, *Correlated electron tunneling through two separate quantum dot systems with strong capacitive interdot coupling*, *Phys. Rev. Lett.* **101** (2008) 186804.

[136] A. Posazhennikova and P. Coleman, *Anomalous conductance of a spin-1 quantum dot*, *Phys. Rev. Lett.* **94** (2005) 036802.

[137] R. M. Konik, H. Saleur, and A. Ludwig, *Transport in quantum dots from the integrability of the anderson model*, *Phys. Rev. B.* **66** (2002) 125304.

[138] Y. Tanaka and N. Kawakami, *Interference effects on kondo-assisted transport through double quantum dots*, *Phys. Rev. B.* **72** (2005) 085304.

[139] A. Tsvelik and P. Wiegmann, *Exact results in the theory of magnetic alloys*, *Adv. in Phys.* **32** (1983) 453.

[140] P. Wiegmann, V. Filyov, and A. Tsvelik, *Exact solution of the symmetric anderson model at t = 0.*, *Sov. Phys. JETP Lett.* **35** (1982) 77.

[141] T. Costi, A. Hewson, and V. Vlatic, *Transport coefficients of the anderson model via the numerical renormalization group.*, *J. Phys.: Cond. Mat.* **6** (1994) 2519.

[142] A. A. Gogolin, R. M. Konik, H. Saleur, and A. W. W. Ludwig, *Counting statistics for the anderson impurity model: Bethe ansatz and fermi liquid study*, *Ann. Phys. (Leipzig)* **16** (2007) 678.

[143] C. H. L. Quay, J. Cumings, S. Gamble, R. de Picciotto, H. Kataura, and D. Goldhaber-Gordon, *Magnetic field dependence of the spin- 1/2 and spin-1 kondo effects in a quantum dot*, *Phys. Rev. B* **76** (2007) 245311.

[144] A. Hewson, *The Kondo Problem to Heavy Fermions*. Cambridge University Press, 1993.

[145] D. M. Newns and N. Read, *Mean-field theory of intermediate valence/heavy fermion systems*, *Advances in Physics* **36** (1987) 799.

[146] D. Langreth, *Friedel sum rule for anderson's model of localized impurity states.*, *Phys. Rev.* **150** (1966) 516.

[147] A. A. Aligia and L. A. Salguero, *Magnetotransport through a quantum wire side coupled to a quantum dot*, *Phys. Rev. B* **70** (1987) 075307.

[148] K. Kang, S. Y. Cho, J.-J. Kim, and S.-C. Shin, *Anti-kondo resonance in transport through a quantum wire with a side-coupled quantum dot*, *Phys. Rev. B* **63** (2001) 113304.

[149] L. H. Nunes and M. F. M. Figueira, *Study of the kondo and high-temperature limits of the slave-boson and x-boson methods*, *Phys. Lett. A* **358** (2006) 313.

[150] P. Schlottmann, *Magnetic and thermal properties of nanoscale heavy-fermion particles*, *Phys. Lett. B* **65** (2001) 024431.

[151] J. Kroha, P. J. Hirschfeld, K. A. Muttalib, and P. Wolfle, *Conserving slave boson approach to strongly corelated fermi ssystems: Single-iimpurity anderson model*, *Solid States Communications* **83** (1992) 1003.

[152] P. Wolfle, *Slave boson theories of correlated electron systems*, *J. Low Temp. Phys.* **99** (1995) 625.

[153] M. Pustilnik and L. Glazman, *Kondo effect in real quantum dots*, *Phys. Rev. Lett.* **87** (2001) 216601.

[154] H. R. Krishna-murthy, J. W. Wilkins, and K. G. Wilson, *Renormalization-group approach to the anderson model of dilute magnetic alloys. i. static properties for the symmetric case.*, *Phys. Rev. B.* **21** (1980) 1003.

[155] K. G. Wilson, *The renormalization group: Critical phenomena and the kondo problem.*, *Rev. Mod. Phys.* **47** (1975) 773.

[156] R. M. Fye, *Quantum monte carlo study of the one-dimensional symmetric anderson lattice.*, *Phys. Rev. B* **41** (1990) 2490.

[157] Y. Meir and N. Wingreen, *Landauer formula for the current through an interacting electron region.*, *Phys. Rev. Lett.* **68** (1992) 2512.

[158] N. Kawakami, *Asymptotic bethe-ansatz solution of multicomponent quantum systems with $1/r^2$ long-range interaction.*, *Phys. Rev. B.* **46** (1992) 1005.

[159] K. Hikami and M. Wadati, *Conserved operators in calogero-moser spin system.*, *J. Phys. Soc. Jpn.* **62** (1993) 2525.

[160] F. D. M. Haldane, Z. N. C. Ha, J. C. Talstra, D. Bernard, and V. Pasquier, *Yangian symmetry of integrable quantum chains with long-range interactions and a new description of states in conformal field theory.*, *Phys. Rev. Lett.* **69** (1992) 2021.

[161] Z. N. C. Ha and F. D. M. Haldane, *Squeezed strings and yangian symmetry of the heisenberg chain with long-range interaction.*, *Phys. Rev. B.* **47** (1993) 12459.

[162] F. D. M. Haldane, *"spinon gas" description of the $s = \frac{1}{2}$ heisenberg chain with inverse-square exchange: Exact spectrum and thermodynamics.*, *Phys. Rev. Lett.* **66** (1991) 1529.

[163] Z. N. C. Ha, *Quantum Many-Body Systems in One Dimension.* World Scientific, Singapore, 1996.

[164] D. H. R. Courant, *Methods of Mathematical Physics: Volume 2.* Wiley-Interscience, 1991.

Appendix A

Asymptotic Bethe Ansatz solution of the spin Calogero Model and separation of variables in hydrodynamics

The spin Calogero model is solvable by an asymptotic Bethe Ansatz (ABA)[43, 63, 158]. This solution turns out to be the most convenient for our purposes.

The most important ingredient of the ABA is the scattering phase which is given by

$$\theta(k) = \pi\lambda\,\mathrm{sgn}(k) \tag{A.1}$$

for sCM. Here k is the relative momentum of two particles and the scattering phase does not depend on the species of particles. The expression for the dressed (true physical) momentum of the particle is given by

$$k(\kappa) = \frac{2\pi}{L}\left[\kappa + \frac{\lambda}{2}\int_{-\infty}^{\infty}\mathrm{sgn}(\kappa-\kappa')\nu(\kappa')\,\mathrm{d}\kappa'\right], \tag{A.2}$$

where κ is an integer-valued non-interacting momentum of the particle (quantum number) and $\nu(\kappa)$ is the number of particles with quantum number κ (see (3.18)). Here we replaced in the scattering phase $\mathrm{sgn}\,(k-k')$ by $\mathrm{sgn}\,(\kappa-\kappa')$[1].

[1]The function $k(\kappa)$ is monotonic and, therefore, $\mathrm{sgn}\,(k-k') = \mathrm{sgn}\,(\kappa-\kappa')$. This trick is specific for Calogero-type models with scattering phase given by $\mathrm{sgn}\,(k-k')$ and works for Haldane-Shastry model in the absence of umklapps.

We immediately obtain from (A.2)

$$L\frac{\mathrm{d}k}{2\pi} = [1+\lambda\nu(\kappa)]\ \mathrm{d}\kappa \tag{A.3}$$

and

$$\nu_{\uparrow(\downarrow)}(\kappa)\,\mathrm{d}\kappa = L\frac{\nu_{\uparrow(\downarrow)}(k)}{1+\lambda\nu(k)}\,\frac{\mathrm{d}k}{2\pi}. \tag{A.4}$$

We can see that the picture corresponding to (A.4) in a single-particle phase space requires that the number of particles in the phase space volume is given by $\frac{dx\,dk}{2\pi(\lambda+1)}$ if only one species is present and $\frac{dx\,dk}{2\pi(\lambda+1/2)}$ when both species are present. This justifies the picture we used (see Figs. 3.4 and C.1).

It is easy to write down the expressions for the conserved quantities using (A.4).

$$N_{\uparrow(\downarrow)} = L\int_{-\infty}^{+\infty}\frac{\mathrm{d}k}{2\pi}\,\frac{\nu_{\uparrow(\downarrow)}(k)}{1+\lambda\nu(k)} \tag{A.5}$$

$$P = L\int_{-\infty}^{+\infty}\frac{\mathrm{d}k}{2\pi}\,\frac{\nu(k)}{1+\lambda\nu(k)}\,k \tag{A.6}$$

$$P_s = L\int_{-\infty}^{+\infty}\frac{\mathrm{d}k}{2\pi}\,\frac{\nu_s(k)}{1+\lambda\nu(k)}\,k \tag{A.7}$$

$$E = L\int_{-\infty}^{+\infty}\frac{\mathrm{d}k}{2\pi}\,\frac{\nu(k)}{1+\lambda\nu(k)}\,\frac{k^2}{2}. \tag{A.8}$$

Here P_s is a conserved quantity proportional to $\mathcal{L}_1^z$ introduced in [159]:

$$\hat{P}_s \equiv -\mathrm{i}\sum_{j=1}^{N}\sigma_j^z\frac{\partial}{\partial x_j} - \mathrm{i}\frac{\lambda}{2}\,\frac{\pi}{L}\sum_{j\neq l}\cot\frac{\pi}{L}\,(x_j-x_l)\ \left[\sigma_j^z-\sigma_l^z\right]\mathrm{P}_{jl}\ . \tag{A.9}$$

One can think of, e.g., $P_\uparrow = (P+P_s)/2$ as of a sum of asymptotic values of momenta of spin-up particles. We have replaced summations by integrations as we need only continuous versions of these formulae. It can be shown that (A.5,A.6,A.8) are equivalent to (4.23,3.19,3.20) with the relation between physical and non-interacting momenta given by (A.2). Moreover, because the measure of integration $\frac{dk}{2\pi}\,\frac{\nu_{\uparrow(\downarrow)}(k)}{1+\lambda\nu(k)}$ is a piece-wise constant for the two-step distribution (3.24), one naturally obtains integrals of motion in a form which is completely separated in terms of Fermi momenta. Indeed for a two-step

distribution (3.24)

$$\nu_\alpha = \begin{cases} 1, & \text{if } k_{L\alpha} < k < k_{R\alpha} \\ 0, & \text{otherwise} \end{cases} \tag{A.10}$$

where $\alpha = \uparrow, \downarrow$. In the CO regime (3.50) we have

$$\begin{aligned} \int_{-\infty}^{\infty} \frac{\mathrm{d}k}{2\pi} \frac{\nu_\uparrow(k)}{1+\lambda\nu(k)}\, f(k) &= \int_{k_{L\uparrow}}^{k_{L\downarrow}} \frac{\mathrm{d}k}{2\pi} \frac{1}{1+\lambda}\, f(k) + \int_{k_{L\downarrow}}^{k_{R\downarrow}} \frac{\mathrm{d}k}{2\pi} \frac{1}{1+2\lambda}\, f(k) + \int_{k_{R\downarrow}}^{k_{R\uparrow}} \frac{\mathrm{d}k}{2\pi} \frac{1}{1+\lambda}\, f(k), \\ \int_{-\infty}^{\infty} \frac{\mathrm{d}k}{2\pi} \frac{\nu_\downarrow(k)}{1+\lambda\nu(k)}\, f(k) &= \int_{k_{L\downarrow}}^{k_{R\downarrow}} \frac{\mathrm{d}k}{2\pi} \frac{1}{1+2\lambda}\, f(k), \end{aligned} \tag{A.11}$$

where $f(k)$ is an arbitrary function. In particular, we obtain for the densities

$$2\pi(\lambda+1)\,\frac{N}{L} = k_{R\uparrow} - k_{L\uparrow} + \frac{1}{2\lambda+1}(k_{R\downarrow} - k_{L\downarrow}), \tag{A.12}$$

$$2\pi(\lambda+1)\,\frac{N_s}{L} = k_{R\uparrow} - k_{L\uparrow} - (k_{R\downarrow} - k_{L\downarrow}), \tag{A.13}$$

$$4\pi(\lambda+1)\,\frac{P}{L} = k_{R\uparrow}^2 - k_{L\uparrow}^2 + \frac{1}{2\lambda+1}(k_{R\downarrow}^2 - k_{L\downarrow}^2), \tag{A.14}$$

$$4\pi(\lambda+1)\,\frac{P_s}{L} = k_{R\uparrow}^2 - k_{L\uparrow}^2 - (k_{R\downarrow}^2 - k_{L\downarrow}^2), \tag{A.15}$$

$$12\pi(\lambda+1)\,\frac{E}{L} = k_{R\uparrow}^3 - k_{L\uparrow}^3 + \frac{1}{2\lambda+1}(k_{R\downarrow}^3 - k_{L\downarrow}^3). \tag{A.16}$$

So far we presented the values of the conserved quantities for the sCM in terms of dressed Fermi momenta. They are given by linear combinations of Fermi momenta raised to the same power. There are infinitely many integrals of motion of this type and they are all in involution (commute with each other). The latter is a pretty stringent requirement and we assume that the only way to satisfy it is to require that the corresponding classical hydrodynamic fields have the following Poisson's brackets

$$\{k_\alpha(x), k_\beta(y)\} = 2\pi s_\alpha \delta_{\alpha\beta} \delta'(x-y), \tag{A.17}$$

where α runs over all Fermi points and s_α are some numbers to be determined. We can determine these numbers, e.g., in the following way. The density of

current j (momentum per unit length) from (A.14) by

$$j(x) = \frac{1}{4\pi(\lambda+1)}\left[k_{R\uparrow}^2 - k_{L\uparrow}^2 + \frac{1}{2\lambda+1}(k_{R\downarrow}^2 - k_{L\downarrow}^2)\right]. \tag{A.18}$$

The total momentum of the system is a generator of the translation algebra $\{P, q(y)\} = \partial_y q(y)$, where $q(y)$ is any field. For the current density we should have

$$\{j(x), q(y)\} = q(x)\delta'(x-y). \tag{A.19}$$

Taking $q(y)$ to be $k_\alpha(y)$ and combining (A.19) with (A.17) we fix the unknown coefficients s_α

$$\begin{aligned} s_{R\uparrow} &= -s_{L\uparrow} = \lambda + 1, \\ s_{R\downarrow} &= -s_{L\downarrow} = (\lambda+1)(2\lambda+1). \end{aligned} \tag{A.20}$$

Computing Poisson's bracket of the hydrodynamic Hamiltonian (obtained from (A.16)

$$H = \frac{1}{12\pi(\lambda+1)}\int \mathrm{d}x\, \left[k_{R\uparrow}^3 - k_{L\uparrow}^3 + \frac{1}{2\lambda+1}(k_{R\downarrow}^3 - k_{L\downarrow}^3)\right] \tag{A.21}$$

with $k_\alpha(x)$ we obtain Riemann-Hopf equation (3.43) for every Fermi momentum field $k_\alpha(x,t)$.

Appendix B

Hydrodynamic velocities

In appendix A we did not use the notion of hydrodynamic velocity. Instead, our hydrodynamic equations were written directly in terms of dressed Fermi momentum fields $k_\alpha(x,t)$. We also know how to express other quantities like density, momentum, energy, etc in terms of these variables. Let us now find the expressions for the velocity fields $v_{\uparrow,\downarrow}$. We focus on the CO regime here and consider other regimes in appendix C.

First of all we, give the expressions for the conserved densities and conserved current densities which can be found from (A.12,A.13,A.14,A.15) as

$$\begin{aligned}
\rho_\uparrow &= \frac{\rho+\rho_s}{2} = \frac{1}{2\pi(\lambda+1)}\left[k_{R\uparrow}-k_{L\uparrow}-\frac{\lambda}{2\lambda+1}(k_{R\downarrow}-k_{L\downarrow})\right], \\
\rho_\downarrow &= \frac{\rho-\rho_s}{2} = \frac{1}{2\pi(2\lambda+1)}(k_{R\downarrow}-k_{L\downarrow}), \qquad \text{(B.1)} \\
j_\uparrow &= \frac{j+j_s}{2} = \frac{1}{4\pi(\lambda+1)}\left[k^2_{R\uparrow}-k^2_{L\uparrow}-\frac{\lambda}{2\lambda+1}(k^2_{R\downarrow}-k^2_{L\downarrow})\right], \\
j_\downarrow &= \frac{j-j_s}{2} = \frac{1}{2\pi(2\lambda+1)}(k^2_{R\downarrow}-k^2_{L\downarrow}). \qquad \text{(B.2)}
\end{aligned}$$

In hydrodynamics, the velocities are defined as variables conjugated to the conserved momenta. Namely, the differential of the energy density defines chemical potentials and velocities as

$$\mathrm{d}\epsilon = \mu_\uparrow \mathrm{d}\rho_\uparrow + \mu_\downarrow \mathrm{d}\rho_\downarrow + v^h_\uparrow \mathrm{d}j_\uparrow + v^h_\downarrow \mathrm{d}j_\downarrow. \qquad \text{(B.3)}$$

Using the energy density obtained from (A.21) we have

$$\mathrm{d}\epsilon = \frac{1}{4\pi(\lambda+1)}\left[k_{R\uparrow}^2\,\mathrm{d}k_{R\uparrow} - k_{L\uparrow}^2\,\mathrm{d}k_{L\uparrow} + \frac{1}{2\lambda+1}\left(k_{R\downarrow}^2\,\mathrm{d}k_{R\downarrow} - k_{L\downarrow}^2\,\mathrm{d}k_{L\downarrow}\right)\right] \tag{B.4}$$

and using (B.1,B.2) one can determine $\mu_{\uparrow,\downarrow}$ and $v_{\uparrow,\downarrow}$. The hydrodynamic velocities are given by linear combinations of Fermi momenta [1]

$$\begin{aligned} v_\uparrow^h &= \frac{1}{2}(k_{R\uparrow}+k_{L\uparrow}), \\ v_\downarrow^h &= \frac{1}{2(\lambda+1)}\left[\lambda(k_{R\uparrow}+k_{L\uparrow})+(k_{R\downarrow}+k_{L\downarrow})\right]. \end{aligned} \tag{B.5}$$

Using (A.17,A.20) one can check that the velocities (B.5) have canonical Poisson's brackets with densities (B.1)[2]

$$\{\rho_\alpha(x), v_\beta(y)\} = \delta_{\alpha\beta}\delta'(x-y), \tag{B.6}$$

where $\alpha,\beta = \uparrow,\downarrow$. The other Poisson's brackets vanish.

The hydrodynamic velocities (B.5) are precisely the ones used in the main body of this chapter for CO regime $v_{\uparrow,\downarrow} = v_{\uparrow,\downarrow}^h$. Equations (3.48,3.49) are the inverse to (B.1,B.5). Interestingly, in the CO regime the velocities and densities of different species can be naturally (simply) written in terms of bare non-interacting momenta (3.29,3.30).

The current density in terms of densities and velocities follows from (A.18) (compare with (3.31))

$$j(x) = \rho_\uparrow v_\uparrow + \rho_\downarrow v_\downarrow. \tag{B.7}$$

The density of "spin-current" which follows from (A.15) has a "correction" proportional to λ compared to the case of free fermions

$$j_s(x) = \rho_\uparrow v_\uparrow - \rho_\downarrow v_\downarrow + 2\lambda\rho_\downarrow(v_\uparrow - v_\downarrow). \tag{B.8}$$

In this appendix we focused on CO regime. Of course, the formalism reviewed here is applicable to all three hydrodynamic regimes (CO, PO, and

[1] This is a peculiar property of the spin-Calogero model and, moreover of CO regime. In PO regime this property does not hold, see appendix C for details.

[2] This is a peculiar property of the spin-Calogero model and, moreover of CO regime. In PO regime this property does not hold, see appendix C for details.

NO). We collect appropriate results in Appendix C.

Appendix C

Hydrodynamic regimes for the spin-Calogero model

Depending on the relative order of four quantum numbers $\kappa_{R,L;\uparrow,\downarrow}$ we distinguish six different hydrodynamic regimes of the sCM. These regimes can be reduced to three essentially different ones exchanging $\uparrow \leftrightarrow \downarrow$. In this appendix we consider these three regimes and then combine all six cases.

Before we proceed, let us remark that the function $k(\kappa)$ defined in (A.2) is monotonic and the order of the quantum numbers $\kappa_{R,L;\uparrow,\downarrow}$ is the same as the one of the physical dressed momenta $k_{R,\uparrow} = k(\kappa_{R,\uparrow})$ etc. Therefore, we can use the latter to define hydrodynamic regimes instead of the bare momenta κ.

C.1 Conserved densities and dressed Fermi momenta

Let us consider generally some integrable system which has two infinite families of mutually commuting conserved quantities. We assume further that the densities of these quantities are given in terms of four dressed Fermi momenta

$k_\alpha(x)$ with $\alpha = 1,2,3,4$ as

$$\begin{aligned} j_n(x) &= \frac{1}{n}\sum_{\alpha=1}^{4} a_\alpha (k_\alpha(x))^n, \\ j_n^s(x) &= \frac{1}{n}\sum_{\alpha=1}^{4} a_\alpha b_\alpha (k_\alpha(x))^n. \end{aligned} \tag{C.1}$$

Here $n = 1,2,3,\ldots$ and a_α, b_α are constant coefficients. We assumed that the conserved densities can be expressed locally in terms of k_α and neglected gradient corrections.

We identify the first several integrals with densities, currents, and the energy as

$$\begin{aligned} j_1(x) &= \rho(x), \\ j_1^s(x) &= \rho_s(x), \\ j_2(x) &= j(x), \\ j_2^s(x) &= j_s(x), \\ j_3(x) &= 2\epsilon(x). \end{aligned} \tag{C.2}$$

We notice here that due to (A.5-A.8) the identifications (C.2) (with (C.1)) are valid for sCM model in all its regimes. The higher order conserved densities (C.1) correspond to conserved quantities of sCM introduced in Ref.[159].

The requirement of vanishing Poisson's brackets between conserved quantities is very restrictive. It can be resolved by requiring canonical Poisson's brackets between Fermi momenta (A.17). If (A.17) is valid, it is easy to check that $\{\int dx\, j_n(x), \int dy\, j_m^s(y)\} = 0$ etc. Using the fact that the total current is the generator of translations (A.19) we can fix the coefficients s_α in (A.17) as $2\pi s_\alpha = 1/a_\alpha$ and obtain

$$\{k_\alpha(x), k_\beta(y)\} = \frac{1}{a_\alpha}\delta_{\alpha\beta}\delta'(x-y). \tag{C.3}$$

Using the Poisson's brackets (C.3) and the Hamiltonian $H = \int dx\, \epsilon(x)$ with (C.2,C.1) it is easy to obtain the Riemann-Hopf evolution equations for the

Table C.1: Summary of three regimes.

	α	$L\uparrow$	$R\uparrow$	$L\downarrow$	$R\downarrow$	
CO	$2\pi(\lambda+1)\,a_\alpha$	-1	1	$-\frac{1}{2\lambda+1}$	$\frac{1}{2\lambda+1}$	$k_{L\uparrow} < k_{L\downarrow} < k_{R\downarrow} < k_{R\uparrow}$
	b_α	1	1	$-(2\lambda+1)$	$2\lambda+1$	
PO	$2\pi(\lambda+1)\,a_\alpha$	-1	$\frac{1}{2\lambda+1}$	$-\frac{1}{2\lambda+1}$	1	$k_{L\downarrow} < k_{L\uparrow} < k_{R\downarrow} < k_{R\uparrow}$
	b_α	1	$2\lambda+1$	$-(2\lambda+1)$	-1	
NO	$2\pi(\lambda+1)\,a_\alpha$	-1	1	-1	1	$k_{L\downarrow} < k_{R\downarrow} < k_{L\uparrow} < k_{R\uparrow}$
	b_α	1	1	-1	-1	

dressed Fermi momenta

$$\partial_t k_\alpha + k_\alpha \partial_x k_\alpha = 0, \qquad \text{for } \alpha = 1,2,3,4 \tag{C.4}$$

and the evolution equations for all conserved densities as

$$\begin{aligned} \partial_t j_n + \partial_x j_{n+1} &= 0, \\ \partial_t j^s_n + \partial_x j^s_{n+1} &= 0. \end{aligned} \tag{C.5}$$

In the hydrodynamic regime only four of the densities are algebraically independent (as there are only four dressed Fermi momenta). Therefore, one can find constitutive relations, i.e., express the energy density in terms of ρ, ρ_s, j and j_s. Alternatively, one can use hydrodynamic velocities v^h and v^h_s defined by (B.3) instead of currents j, j_s.

We can see that the hydrodynamics (C.1,C.2,C.3) is fully defined by coefficients a_α, b_α. In fact, these coefficients are not totally independent. Requiring that densities ρ and ρ_s have vanishing Poisson's brackets with themselves and with each other gives three relations between the coefficients

$$\begin{aligned} \sum_\alpha a_\alpha &= 0, \\ \sum_\alpha b_\alpha a_\alpha &= 0, \\ \sum_\alpha b^2_\alpha a_\alpha &= 0. \end{aligned} \tag{C.6}$$

For CO, PO, and NO regimes of sCM these coefficients are summarized in the Table C.1. These coefficients do satisfy relations (C.6).

The matrix of Poisson's brackets of the dressed Fermi momenta k_α (C.3) is diagonal but not proportional to the unit matrix. It is interesting that the

Poisson's brackets of bare momenta κ_α satisfy

$$\{\kappa_\alpha(x), \kappa_\beta(y)\} = (-1)^\alpha \frac{L^2}{2\pi} \delta_{\alpha\beta} \delta'(x-y). \tag{C.7}$$

One then obtains that the "velocities" introduced in (3.29,3.30) are canonically conjugate to the corresponding densities and can be written as linear combinations of κ_α (and of k_α). The velocities (3.29,3.30) are defined just as conjugate variables to the densities. This definition is not unique. One can always shift $v_\uparrow \to v_\uparrow + 2\pi\gamma\rho_\downarrow$ and $v_\downarrow \to v_\downarrow - 2\pi\gamma\rho_\uparrow$ with any number γ without changing Poisson's brackets. The particular choice of variables (3.29,3.30) is convenient because it defines velocities continuously across all hydrodynamic regimes. Moreover, we have

$$\begin{aligned} v_{\uparrow,\downarrow} &= v^h_{\uparrow,\downarrow}, \qquad\qquad \text{for CO}, \\ v_{\uparrow,\downarrow} &= v^h_{\uparrow,\downarrow} \pm \pi\lambda\rho_{\downarrow,\uparrow}, \qquad \text{for NO}. \end{aligned} \tag{C.8}$$

In PO regime the hydrodynamic velocities are not linear combinations of k_α and their relations to the conjugated variables $v_{\uparrow,\downarrow}$ used in this chapter are more complicated.

C.2 Complete Overlap Regime (CO)

The Complete Overlap regime corresponds to the case when

$$-\frac{\pi}{2}\,|\rho_s| < v_s < \frac{\pi}{2}\,|\rho_s|\,. \tag{C.9}$$

In this case the support of $\nu_\downarrow$ is a subset of the support of $\nu_\uparrow$ (or vice versa). In the main body of the chapter we mostly concentrated on this case, but for convenience we recap the main formulae in this appendix as well. The dressed momenta (A.2) in the CO regime for $\rho_s > 0$, i.e., for the ordering

$$k_{L\uparrow} < k_{L\downarrow} < k_{R\downarrow} < k_{R\uparrow}\,, \tag{C.10}$$

are

$$\begin{aligned} k_{R\uparrow,L\uparrow} &= v_\uparrow \pm \pi\left[(\lambda+1)\rho_\uparrow + \lambda\rho_\downarrow\right] = v_\uparrow \pm \pi\rho_\uparrow \pm \lambda\pi\rho_c, \\ k_{R\downarrow,L\downarrow} &= (\lambda+1)v_\downarrow - \lambda v_\uparrow \pm \pi(2\lambda+1)\rho_\downarrow \\ &= v_\downarrow \pm \pi\rho_\downarrow + \lambda(-2v_s \pm 2\pi\rho_\downarrow). \end{aligned} \tag{C.11}$$

Poisson's brackets of k_α are given by (C.3) with coefficients from the Table C.1. One can express all conserved densities (C.1) in terms of dressed Fermi momenta using the Table C.1. For example, the Hamiltonian (see (C.2)) reads

$$H_{\rm CO} = \frac{1}{12\pi(\lambda+1)}\int \mathrm{d}x\,\left[k_{R\uparrow}^3 - k_{L\uparrow}^3 + \frac{1}{2\lambda+1}\left(k_{R\downarrow}^3 - k_{L\downarrow}^3\right)\right] \tag{C.12}$$

$$\begin{aligned} &= \int \mathrm{d}x\,\Bigg\{\frac{1}{2}\rho_\uparrow v_\uparrow^2 + \frac{1}{2}\rho_\downarrow v_\downarrow^2 + \frac{\lambda}{2}\rho_\downarrow\big(v_\uparrow - v_\downarrow\big)^2 \\ &\qquad + \frac{\pi^2\lambda^2}{6}\rho_c^3 + \frac{\pi^2}{6}\big(\rho_\uparrow^3 + \rho_\downarrow^3\big) \\ &+ \frac{\lambda\pi^2}{6}\big(2\rho_\uparrow^3 + 3\rho_\uparrow^2\rho_\downarrow + 3\rho_\downarrow^3\big)\Bigg\}. \end{aligned} \tag{C.13}$$

The evolution equations are given by (C.4) and can also be recast in terms of equations for densities and velocities (3.38,3.39).

C.3 Partial Overlap Regime (PO)

There are two regimes when the supports of $\nu_\uparrow$ and $\nu_\downarrow$ only partially overlap. Here we concentrate on the case for which

$$\frac{\pi}{2}\,|\rho_s| < v_s < \frac{\pi}{2}\,\rho_c\,, \tag{C.14}$$

corresponding to the ordering

$$k_{L\downarrow} < k_{L\uparrow} < k_{R\downarrow} < k_{R\uparrow}\,. \tag{C.15}$$

The other PO regime can be obtained by exchanging up and down particles, i.e. by changing $v_s \to -v_s$. In this case the dressed momenta (A.2) are

$$\begin{aligned}
k_{L\downarrow} &= v_\downarrow - \pi(\lambda+1)\rho_\downarrow - \pi\lambda\rho_\uparrow = v_\downarrow - \pi\rho_\downarrow - \lambda\pi\rho_c, \\
k_{L\uparrow} &= v_\uparrow + \lambda(v_\uparrow - v_\downarrow) - \pi(2\lambda+1)\rho_\uparrow = v_\uparrow - \pi\rho_\uparrow + \lambda(2v_s - 2\pi\rho_\uparrow), \\
k_{R\downarrow} &= v_\downarrow - \lambda(v_\uparrow - v_\downarrow) + \pi(2\lambda+1)\rho_\downarrow = v_\downarrow + \pi\rho_\downarrow - \lambda(2v_s - 2\pi\rho_\downarrow), \\
k_{R\uparrow} &= v_\uparrow + \pi(\lambda+1)\rho_\uparrow + \pi\lambda\rho_\downarrow = v_\uparrow + \pi\rho_\uparrow + \lambda\pi\rho_c
\end{aligned} \tag{C.16}$$

and the Hamiltonian becomes (see Table C.1 and (C.1,C.2))

$$H_{\mathrm{PO}} = \frac{1}{12\pi(\lambda+1)} \int \mathrm{d}x \left[k_{R\downarrow}^3 - k_{L\uparrow}^3 + \frac{1}{2\lambda+1} \left(k_{R\uparrow}^3 - k_{L\downarrow}^3 \right) \right] \tag{C.17}$$

$$\begin{aligned}
= \int \mathrm{d}x \Bigg\{ & \frac{1}{2}\rho_\uparrow v_\uparrow^2 + \frac{1}{2}\rho_\downarrow v_\downarrow^2 + \lambda\pi\rho_\uparrow\rho_\downarrow (v_\downarrow - v_\uparrow) - \frac{\lambda}{12\pi} \left[v_\uparrow - v_\downarrow - \pi(\rho_\uparrow + \rho_\downarrow) \right]^3 \\
& + \frac{\pi^2\lambda^2}{6} (\rho_\uparrow + \rho_\downarrow)^3 + \frac{\pi^2}{6}(1+2\lambda) \left(\rho_\uparrow^3 + \rho_\downarrow^3 \right) \Bigg\}.
\end{aligned} \tag{C.18}$$

Poisson's brackets of k_α are given by (C.3) with coefficients from the Table C.1 and evolution equations are given by (C.4).

C.4 No Overlap Regime (NO)

In this case, the supports of $\nu_\uparrow$ and $\nu_\downarrow$ do not overlap at all. For $v_s > 0$ the ordering of dressed Fermi momenta is

$$k_{L\downarrow} < k_{R\downarrow} < k_{L\uparrow} < k_{R\uparrow} \tag{C.19}$$

and momenta themselves are

$$\begin{aligned}
k_{R\uparrow,L\uparrow} &= v_\uparrow + \pi\lambda\rho_\downarrow \pm \pi(\lambda+1)\rho_\uparrow = v_\uparrow \pm \pi\rho_\uparrow \pm \lambda\pi\rho_{c,s}, \\
k_{R\downarrow,L\downarrow} &= v_\downarrow - \pi\lambda\rho_\uparrow \pm \pi(\lambda+1)\rho_\downarrow = v_\downarrow \pm \pi\rho_\downarrow - \lambda\pi\rho_{s,c}.
\end{aligned} \tag{C.20}$$

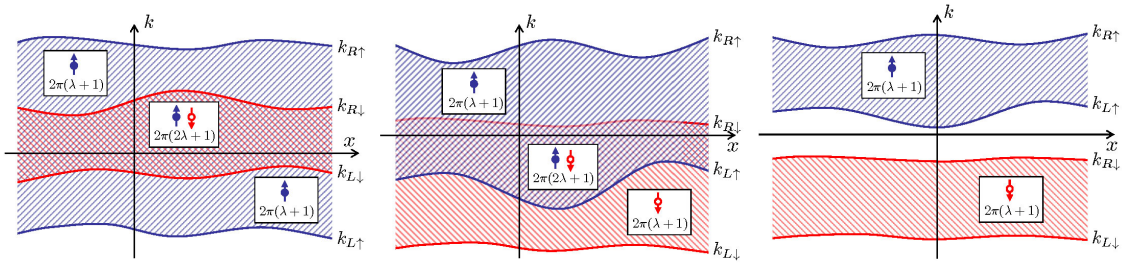

Figure C.1: Phase-space diagrams of a hydrodynamic states characterized by four space-dependent Fermi momenta in three regimes CO, PO, and NO respectively.

and the Hamiltonian becomes (see Table C.1 and (C.1,C.2))

$$H_{\rm NO} = \frac{1}{12\pi(\lambda+1)}\int {\rm d}x\,\left[k_{R\uparrow}^3 - k_{L\uparrow}^3 + k_{R\downarrow}^3 - k_{L\downarrow}^3\right] \tag{C.21}$$

$$\begin{aligned} &= \int {\rm d}x \Big\{ \frac{1}{2}\rho_\uparrow v_\uparrow^2 + \frac{1}{2}\rho_\downarrow v_\downarrow^2 + \lambda\pi\rho_\uparrow\rho_\downarrow\left(v_\uparrow - v_\downarrow\right) \\ &\qquad + \frac{\pi^2}{6}\left(\lambda+1\right)^2\left(\rho_\uparrow+\rho_\downarrow\right)^3 \\ &- \frac{\pi^2}{2}\left(1+2\lambda\right)\rho_\uparrow\rho_\downarrow\left(\rho_\uparrow+\rho_\downarrow\right)\Big\}. \end{aligned} \tag{C.22}$$

Poisson's brackets of k_α are given by (C.3) with coefficients from the Table C.1 and evolution equations are given by (C.4).

C.5 All cases combined

It is possible to combine all hydrodynamic regimes into relatively compact expressions introducing absolute values of hydrodynamic fields. A general Hamiltonian valid for all regimes takes a form

$$\begin{aligned} H &= \int {\rm d}x \Big\{ \frac{1}{2}\rho_\uparrow v_\uparrow^2 + \frac{1}{2}\rho_\downarrow v_\downarrow^2 + \frac{\pi^2}{6}\left(\rho_\uparrow^3+\rho_\downarrow^3\right) + \frac{\pi^2}{6}\lambda^2\rho_c^3 + \frac{\pi^2}{3}2\lambda(\rho_\uparrow^3+\rho_\downarrow^3) \\ &\qquad + \lambda\,\rho_c\xi_1\xi_2 - \frac{\lambda}{3\pi}\left(|\xi_1|^3+|\xi_2|^3\right) \\ &+ \frac{\lambda}{3\pi}\left[|\chi_1|^3 - \chi_1^3 + |\chi_2|^3 + \chi_2^3\right]\Big\}, \end{aligned} \tag{C.23}$$

k inequality	v_s	ρ_s	$\xi_1 = v_s + \frac{\pi}{2}\rho_s$	$\xi_2 = v_s - \frac{\pi}{2}\rho_s$	$\chi_1 = v_s + \frac{\pi}{2}\rho_c$	$\chi_2 = v_s - \frac{\pi}{2}\rho_c$	v_s inequality	Regime
$k_{L\uparrow} < k_{R\uparrow} < k_{L\downarrow} < k_{R\downarrow}$	$-$		$-$	$-$	$-$	$-$	$v_s < -\frac{\pi}{2}\rho_c$	NO
$k_{L\uparrow} < k_{L\downarrow} < k_{R\uparrow} < k_{R\downarrow}$	$-$		$-$	$-$	$+$	$-$	$-\frac{\pi}{2}\rho_c < v_s < -\frac{\pi}{2}\lvert\rho_s\rvert$	PO
$k_{L\downarrow} < k_{L\uparrow} < k_{R\uparrow} < k_{R\downarrow}$		$-$	$-$	$+$	$+$	$-$	$\frac{\pi}{2}\rho_s < v_s < -\frac{\pi}{2}\rho_s$	CO
$k_{L\uparrow} < k_{L\downarrow} < k_{R\downarrow} < k_{R\uparrow}$		$+$	$+$	$-$	$+$	$-$	$-\frac{\pi}{2}\rho_s < v_s < \frac{\pi}{2}\rho_s$	CO
$k_{L\downarrow} < k_{L\uparrow} < k_{R\downarrow} < k_{R\uparrow}$	$+$		$+$	$+$	$+$	$-$	$\frac{\pi}{2}\lvert\rho_s\rvert < v_s < \frac{\pi}{2}\rho_c$	PO
$k_{L\downarrow} < k_{R\downarrow} < k_{L\uparrow} < k_{R\uparrow}$	$+$		$+$	$+$	$+$	$+$	$\frac{\pi}{2}\rho_c < v_s$	NO

Table C.2: Classification of different regimes: + indicates that the field takes positive values, − that it is negative. A blank means that its sign is arbitrary.

where we introduced the following notations

$$\xi_{1,2} \equiv v_s \pm \frac{\pi}{2}\,\rho_s\,, \tag{C.24}$$

$$\chi_{1,2} \equiv v_s \pm \frac{\pi}{2}\,\rho_c\,. \tag{C.25}$$

The Hamiltonian (C.23) can be obtained from (3.20,3.21) for the general case of a two-step distribution function $\nu_{\uparrow,\downarrow}(\kappa)$. We collect in the Table C.2 the information necessary to go quickly from the general expression (C.23) to the particular ones valid in separate regimes (CO, PO or NO).

We can combine the evolution equations following from (C.23) in the spin/charge basis (3.12) as

$$\dot{\rho}_c = -\partial_x\Big\{\rho_c v_c + \rho_s v_s\Big\}, \tag{C.26}$$

$$\dot{\rho}_s = -\partial_x\left\{\rho_c v_s + \rho_s v_c - \frac{\lambda}{\pi}\Big[\xi_1|\xi_1| + \xi_2|\xi_2| - \chi_1|\chi_1| - \chi_2|\chi_2|\Big]\right\}, \tag{C.27}$$

$$\dot{v}_c = -\partial_x\left\{\frac{v_c^2 + v_s^2}{2} + \frac{\pi^2}{8}\Big[\big(4\lambda^2 + 2\lambda + 1\big)\,\rho_c^2 + (2\lambda+1)\,\rho_s^2\Big] + \frac{\lambda}{2}\Big[\chi_1|\chi_1| - \chi_2|\chi_2|\Big]\right\}, \tag{C.28}$$

$$\dot{v}_s = -\partial_x\left\{v_c v_s + \frac{\pi^2}{4}\,(2\lambda+1)\,\rho_c\rho_s - \frac{\lambda}{2}\Big[\xi_1|\xi_1| - \xi_2|\xi_2|\Big]\right\}. \tag{C.29}$$

For CO and PO regimes the Hamiltonian (C.23) takes an especially simple

form in terms of dressed momenta

$$H_{\mathrm{CO\,\&\,PO}} = \frac{1}{12\pi\,(2\lambda+1)}\int \mathrm{d}x\Bigg\{k^3_{R\uparrow}-k^3_{L\uparrow}+k^3_{R\downarrow}-k^3_{L\downarrow}+\frac{\lambda}{(\lambda+1)}\Big[\big|k^3_{L\uparrow}-k^3_{L\downarrow}\big| + \big|k^3_{R\uparrow}-k^3_{R\downarrow}\big|\Big]\Bigg\}\,, \tag{C.30}$$

which are related to density and velocity fields as

$$\begin{aligned} k_{R\uparrow,L\uparrow} &= v_\uparrow \pm \pi(\lambda+1)\rho_\uparrow + \lambda\chi_{1,2} \mp \lambda|\xi_{1,2}|\,, \\ k_{R\downarrow,L\downarrow} &= v_\downarrow \pm \pi(1+\lambda)\rho_\downarrow - \lambda\chi_{2,1} \mp \lambda|\xi_{1,2}|\,. \end{aligned} \tag{C.31}$$

As in the separate cases considered before, these momenta have canonical Poisson's brackets (A.17) with

$$\begin{aligned} s_{R\uparrow,R\downarrow} &= (\lambda+1)\left[\lambda+1\pm\lambda\,\mathrm{sgn}\,(\xi_1)\right] \\ s_{L\uparrow,L\downarrow} &= -(\lambda+1)\left[\lambda+1\mp\lambda\,\mathrm{sgn}\,(\xi_2)\right] \end{aligned} \tag{C.32}$$

and evolve independently according to the Riemann-Hopf equations (C.4).

Appendix D

Hydrodynamic description of Haldane-Shastry model from its Bethe Ansatz solution

The Haldane-Shastry model (HSM) is a Heisenberg spin chain with long-ranged interaction defined by the Hamiltonian:

$$H_{\text{HSM}} = \frac{1}{2} \sum_{j<l} \frac{\mathbf{K}_{jl}}{d\,(j-l)^2} \,, \tag{D.1}$$

where we K_{jl} is the spin-exchange operator[1]:

$$\mathbf{K}_{jl} = \frac{\vec{\sigma}_j \cdot \vec{\sigma}_l + 1}{2} \,, \tag{D.2}$$

and $d(j) \equiv (N/\pi)\,|\sin(\pi j/N)|$ is the chord distance between two points on a lattice with N sites and periodic boundary conditions. The model (D.1) has been introduced independently at the same time by Haldane[66] and by Shastry[67] and has been shown to be integrable. The energy spectrum of the HSM is equivalent to that of the Calogero-Sutherland model at $\lambda = 2$, but with a high degeneracy due to the Yangian symmetry [160, 161].

In this appendix we used the Bethe Ansatz solution [66, 162, 163] to construct a gradientless hydrodynamic description for the HSM similarly to what we have done for the sCM model in section 3.4 and appendix A. To this

[1] Note that for fermions $\mathbf{P}_{jl}\,\mathbf{K}_{jl} = -1$.

end, we consider a state with M overturned spins over an initial ferromagnetic configuration (say from up to down and $M < N/2$) and introduce M integer quantum numbers κ's to characterize the state in the Bethe Ansatz formalism. As before such state can be described by a distribution function $\nu(\kappa) = 0, 1$, depending on whether that quantum number is present or not in the BA solution. Following [66] we impose a condition on the integer numbers: $|\kappa| < (N - M - 1)/2$. [2]

The scattering phase for the HSM is

$$\theta(k) = \pi \, \mathrm{sgn}(k) \, , \tag{D.3}$$

which corresponds to setting $\lambda = 1$ into (A.1)[3]. Please note that since we are considering a lattice model, the momentum is defined within the Brillouin zone: $-\pi < k < \pi$, where we took the lattice spacing as unity.

At this point, all the derivations of appendix A can be repeated step by step for the HSM just by setting everywhere $\lambda = 1$, and remembering that the momentum is always defined modulo 2π. In particular, the dressed momentum is

$$k(\kappa) = \frac{2\pi}{L} \left[\kappa + \frac{1}{2} \int \mathrm{sgn}\,(\kappa - \kappa') \tilde{\nu}(\kappa') \mathrm{d}\kappa' \right] , \tag{D.4}$$

where again we replaced $\mathrm{sgn}\,(k - k')$ by $\mathrm{sgn}\,(\kappa - \kappa')$[4] and the distribution of the physical momenta is given by

$$\nu(\kappa)\mathrm{d}\kappa = \frac{N}{4\pi} \, \nu(k)\mathrm{d}k \, . \tag{D.5}$$

In terms of this distribution function, the conserved quantities can be writ-

[2] This corresponds to having a single compact support of ν within a single Brillouin zone. Other regimes will require an analysis of umklapp processes[158] and will not be considered here.

[3] This scattering phase is identical to the one in $\lambda = 2$ bosonic Calogero-Sutherland model [66].

[4] The function $k(\kappa)$ is monotonic and, therefore, $\mathrm{sgn}\,(k - k') = \mathrm{sgn}\,(\kappa - \kappa')$. This trick is specific for Calogero-type models with scattering phase given by $\mathrm{sgn}\,(k - k')$ and works for Haldane-Shastry model in the absence of umklapps.

ten as

$$M = N \int \frac{\mathrm{d}k}{4\pi}\, \nu(k), \tag{D.6}$$

$$P = N \int \frac{\mathrm{d}k}{4\pi}\, \nu(k)\, k, \tag{D.7}$$

$$E = E_0 + N \int \frac{\mathrm{d}k}{4\pi}\, \nu(k)\, \frac{k^2}{2}, \tag{D.8}$$

where the momentum is defined only modulo 2π. From now on, we will drop the constant energy shift E_0.

In a hydrodynamic description we assume a distribution of the uniform type

$$\nu(k) = \begin{cases} 1, & \text{if } -\pi < k_L < k < k_R < \pi, \\ 0, & \text{otherwise,} \end{cases} \tag{D.9}$$

where $k_{R,L}$ are some numbers. Using (D.9) and introducing space dependent fields instead of constants we write (D.6,D.7) as

$$M = \int \mathrm{d}x\, \frac{k_R - k_L}{4\pi} = \int \mathrm{d}x\, \rho, \tag{D.10}$$

$$P = \int \mathrm{d}x\, \frac{k_R^2 - k_L^2}{8\pi} = \int \mathrm{d}x\, \rho\, v, \tag{D.11}$$

which suggests the identification

$$k_{R,L} = v \pm 2\pi\rho\ . \tag{D.12}$$

Then the hydrodynamic Hamiltonian follows from (D.8):

$$H_{\mathrm{HSM}} = \int \mathrm{d}x\, \frac{k_R^3 - k_L^3}{24\pi} = \int \mathrm{d}x \left[\frac{1}{2}\, \rho\, v^2 + \frac{2}{3}\, \pi^2\, \rho^3 \right]\ , \tag{D.13}$$

which corresponds, as expected, to the (gradientless) hydrodynamic of a $\lambda = 1$ spin-less Calogero-Sutherland model (3.37).

We think of slowly varying fields $\rho(x,t)$ and $v(x,t)$ as of classical fields obeying the Poisson relation $\{\rho(x), v(y)\} = \delta'(x-y)$. Then (D.13) generates

the evolutions equations

$$\begin{aligned} \dot{\rho} &= -\partial_x \left(\rho v\right), \\ \dot{v} &= -\partial_x \left(\frac{v^2}{2} + \frac{\pi^2}{2} 4\rho^2\right). \end{aligned} \tag{D.14}$$

One can easily recognize in (D.14) the hydrodynamics of spinless Calogero-Sutherland model (3.37) for $\lambda = 1$. The correspondence between eigenstates and eigenenergies of Haldane-Shastry model with $\lambda = 2$ spinless Calogero-Sutherland model has been noticed in the original paper [66]. The degeneracy of the states due to the $SU(2)$ invariance and Yangian symmetry is lost in our classical hydrodynamics model.

For comparisons with the derivations from freezing trick [57] in section 3.6 we express (D.13,D.17) in terms of ρ_s and v_s used in the main body of the chapter. We identify the density $\rho = M/N = \rho_\downarrow$ as the density of spin-down particles and the velocity v as a velocity of spin-down particles relative to the static background of spin-up particles, i.e., $v = v_\uparrow - v_\downarrow = -2v_s$. The charge density corresponding to the lattice with spacing one is just $\rho_0 = 1$. We summarize

$$\rho = \rho_\downarrow = \frac{\rho_0 - \rho_s}{2}, \qquad v = -2v_s, \qquad \rho_0 = 1. \tag{D.15}$$

Using (D.15) we rewrite (D.13) as

$$H_{\rm HSM} = \int \mathrm{d}x \left\{ \rho_0 v_s^2 - \rho_s v_s^2 + \frac{\pi^2 \rho_0 \rho_s^2}{4} - \frac{\pi^2 \rho_s^3}{12} \right\}, \tag{D.16}$$

where we neglected a constant and a term linear in ρ_s, which amounts to a shift in the chemical potential. The evolution equations for the spin density and spin velocity follow from (D.14,D.15)

$$\begin{aligned} \dot{\rho}_s &= -\partial_x \left\{ 2v_s\rho_0 - 2v_s\rho_s \right\}, \\ \dot{v}_s &= -\partial_x \left\{ -v_s^2 + \frac{\pi^2}{2}\rho_0\rho_s - \frac{\pi^2}{4}\rho_s^2 \right\}. \end{aligned} \tag{D.17}$$

We notice that the above (D.16, D.17) is nothing but the strong interaction limit of the sCM (3.53,3.56,3.58).

Finally, we remark that it is easy to check that the distribution function (D.9) implies that $-\frac{\pi\rho_s}{2} \leq v_s \leq \frac{\pi\rho_s}{2}$ and therefore corresponds to the CO regime of spin-Calogero model.

Both in this appendix and in writing classical hydrodynamics for sCM we neglected the degeneracy of the corresponding quantum models due to the Yangian symmetry [160, 161]. We assumed that during the evolution string states are not excited. Of course, the degeneracy plays a very important role for perturbed integrable systems and for the hydrodynamics at finite temperatures.

Appendix E

Exact solution for Riemann-Hopf equation in arbitrary potential

In this appendix we find an exact solution $k(x,t)$ of the forced Riemann-Hopf equation,

$$k_t + \epsilon'(k)k_x = -V'(x). \tag{E.1}$$

Here $\epsilon(k)$ is some function referred to as "dispersion" and the prime means the derivative with respect to the independent variable (e.g., $\epsilon'(k) = \partial\epsilon/\partial k$). The problem is to solve (E.1) with an initial condition $k = k_0(x)$ at $t = 0$. This problem can be easily solved using the general method of characteristics [164]. In this appendix we solve the Euler-type Eq. (E.1) rewriting it in the Lagrange formulation. Namely, we notice that the left hand side of (E.1) can be interpreted as the time derivative in the reference frame of the moving particle. In other words (E.1) is equivalent to

$$\dot{x} = \epsilon'(k), \tag{E.2}$$

$$\dot{k} = -V'(x). \tag{E.3}$$

Here dot means time derivative and $\dot{k}(x(t),t) = \partial_t k + \dot{x}\,\partial_x k$ is nothing else but the left hand side of (E.1).

The system of equations (E.2,E.3) has a first integral of motion (energy)

$$\epsilon(k) + V(x) = E, \tag{E.4}$$

where E is a time-independent constant determined by an initial condition. We invert (E.4) and use it and (E.2) to find a solution of (E.2,E.3) and, therefore, of (E.1)

$$\begin{aligned} k(x) &= \epsilon^{-1}(E - V(x)), && \text{(E.5)} \\ t &= \int_s^x \frac{dy}{\epsilon'(k(y))}, && \text{(E.6)} \\ E &= \epsilon(k_0(s)) + V(s), && \text{(E.7)} \end{aligned}$$

where the last equation gives the value of the energy E in terms of initial data parametrically given as $x = s$ and $k = k_0(s)$.

The system (E.5-E.7) defines the solution $k(x,t)$ of (E.1) for a given initial profile $k_0(x)$.

Let us now assume that there is no external potential $V(x) = 0$ and the dispersion is quadratic $\epsilon(k) = k^2/2$. Excluding E and s from (E.5-E.7) we have

$$k = k_0(x - kt), \qquad \text{(E.8)}$$

which is being solved with respect to k gives a well-known exact solution $k(x,t)$ of (E.1). The solution (E.8) was extensively used in Ref. [15] for studies of the dynamics of sCM in the absence of an external potential.

In the presence of an external harmonic potential $V(x) = \omega^2 x^2/2$ (and $\epsilon(k) = k^2/2$) we have from (E.5-E.7)

$$\begin{aligned} k(x) &= \sqrt{2E - \omega^2 x^2}, && \text{(E.9)} \\ t &= \int_s^x \frac{dy}{\sqrt{2E - \omega^2 y^2}}, && \text{(E.10)} \\ E &= \frac{1}{2}\left[k_0(s)^2 + \omega^2 s^2\right]. && \text{(E.11)} \end{aligned}$$

Calculating the integral (E.10) and excluding E from the system (E.9-E.11) we obtain after straightforward manipulations

$$\begin{aligned} \omega\, x &= R(s)\sin\left[\omega t + \alpha(s)\right], && \text{(E.12)} \\ k &= R(s)\cos\left[\omega t + \alpha(s)\right], && \text{(E.13)} \end{aligned}$$

where we introduced

$$\alpha(s) = \tan^{-1}\left(\frac{\omega s}{k_0(s)}\right), \tag{E.14}$$

$$R(s) = \sqrt{\omega^2 s^2 + k_0(s)^2}. \tag{E.15}$$

The equations (E.12,E.13) together with definitions (E.14,E.15) give a parametric (s is the running parameter) solution of (E.1) for the case of quadratic dispersion and harmonic external potential. Putting $\omega \to 1$ in (E.12-E.15) we reproduce (4.32-4.35) used in the main body of the chapter.

Appendix F

Action for the DFP solution

In this appendix, we will revise the calculation presented in [65] and adapt it to our case. We want to find the value of the hydrodynamic action calculated on a given solution satisfying the DFP boundary conditions.

The gradientless hydrodynamic action in imaginary time $\tau \equiv it$ can, in general, be written as

$$\mathcal{S} = \int \mathrm{d}^2x \; \mathcal{L}[v,\rho] = \int \mathrm{d}x \, \mathrm{d}\tau \, \rho \left\{ \frac{v^2}{2} + \epsilon(\rho) - \mu \right\} , \tag{F.1}$$

where

$$\epsilon(\rho) = \frac{\lambda^2\pi^2}{6}\rho^2 \tag{F.2}$$

is the internal energy per particle of a Calogero system and

$$\mu \equiv \partial_\rho \left[\rho\epsilon(\rho)\right]_{\rho=\rho_0} = \frac{\lambda^2\pi^2}{2}\rho_0^2 \tag{F.3}$$

is the chemical potential. The action (F.1) has to be supplemented with the continuity equation

$$\partial_\tau \rho + \partial_x \left(\rho v\right) = 0 \, , \tag{F.4}$$

which can be considered as a constraint relating the two conjugated fields ρ and v. This constraint can be resolved by introducing the displacement field $\phi(x,\tau)$:

$$\rho = \rho_0 + \partial_x\phi \, , \qquad\qquad j = \rho v = -\partial_\tau\phi \, . \tag{F.5}$$

Physically, the displacement field counts the number of particles to the left

of a point. We can use (F.5) to write the Lagrangian as a functional of ϕ: $\mathcal{L}[\rho, v] = \mathcal{L}[\phi]$. Its variation then gives the Euler equation for the fluid, which can be written more simply as

$$\partial_\tau v + v\partial_x v = \partial_x \partial_\rho \left[\rho\epsilon(\rho)\right] = \lambda^2\pi^2\rho\partial_x\rho \; . \tag{F.6}$$

For the particular choice of internal energy (F.2), corresponding to the Calogero-Sutherland interaction or exclusion statistics, the Euler equation and the continuity equation can be combined into a single complex Riemann-Hopf equation:

$$\partial_\tau k - \mathrm{i}k\partial_x k = 0 \; , \qquad\qquad k(\tau, x) \equiv \lambda\pi\rho(\tau, x) + \mathrm{i}v(\tau, x) \; . \tag{F.7}$$

This equation has a simple, implicit, solution of the form

$$k = F(x + \mathrm{i}k\tau) \; . \tag{F.8}$$

In the body of the chapter, we argued that a solution satisfying the DFP boundary conditions is of the form

$$F(z) \equiv F(z; \rho_0, \eta) = \lambda\pi\rho_0 + \lambda\pi\eta\left(\frac{z}{\sqrt{z^2 - R^2}} - 1\right) \; . \tag{F.9}$$

Here, ρ_0 is the background (equilibrium) density at infinity (where moreover $v = 0$), and η is a, possibly complex, constant specifying the DFP.

To calculate the Depletion Formation Probability, we need to compare the action (F.1) calculated on the solution (F.8,F.9) to the action of an equilibrium configuration:

$$\mathcal{S} - \mathcal{S}_0 = \int \mathrm{d}x\, \mathrm{d}\tau \left\{\rho\frac{v^2}{2} + \rho\epsilon(\rho) - \rho_0\epsilon(\rho_0) - \mu(\rho - \rho_0)\right\} \; . \tag{F.10}$$

To take advantage of the fact that (F.8) is a solution of the equations of motion, we first take the variation of (F.10) with respect to the parameters of the solution. In this way, we will reduce a two-dimensional integration to a contour integral over the boundaries, since the bulk terms are proportional to

the Euler-Lagrange equations and vanish:

$$\mathrm{d}\left(\mathcal{S}-\mathcal{S}_0\right)=\partial_{\rho_0}\left(\mathcal{S}-\mathcal{S}_0\right)\ \mathrm{d}\rho_0+\partial_\eta\left(\mathcal{S}-\mathcal{S}_0\right)\ \mathrm{d}\eta+\partial_{\bar\eta}\left(\mathcal{S}-\mathcal{S}_0\right)\ \mathrm{d}\bar\eta\ . \qquad \text{(F.11)}$$

We have:

$$\begin{aligned}\partial_\eta\left(\mathcal{S}-\mathcal{S}_0\right) &= \int \mathrm{d}^2x\left\{-v\partial_\tau\phi_\eta-\left[\frac{v^2}{2}-\partial_\rho\left(\rho\epsilon\right)+\mu\right]\partial_x\phi_\eta\right\}\\ &= \int \mathrm{d}^2x\left\{-\partial_\tau\left[v\,\phi_\eta\right]-\partial_x\left[\left(\frac{v^2}{2}-\partial_\rho\left(\rho\epsilon\right)+\mu\right)\phi_\eta\right]\right.\\ &\qquad\left.+\left[\partial_\tau v+v\partial_x v-\partial_x\partial_\rho\left(\rho\epsilon\right)\right]\phi_\eta\right\}\\ &= -\oint\left\{\left[v\,\phi_\eta\right]\mathrm{d}x+\left[\left(\frac{v^2}{2}-\partial_\rho\left(\rho\epsilon\right)+\mu\right)\phi_\eta\right]\mathrm{d}t\right\}\ , \qquad \text{(F.12)}\end{aligned}$$

where $\phi_\eta\equiv\partial_\eta\phi$.

The boundaries over which the contour integral is taken are, by Stoke's theorem, the points where the integrand has a discontinuity. It is easy to check that this contour comprises only two paths: one at infinity ($C_0\equiv\{|x+\mathrm{i}k\tau|=\infty\}$) and one around the branch cut of (F.9), which we take along the real axis ($C_1=\{\tau=0^{\pm},-R<x<R\}$).

From (F.8,F.9), at infinity we have

$$\rho(|z_0|\to\infty) \simeq \rho_0+\frac{R^2}{4}\left(\frac{\eta}{z_0^2}+\frac{\bar\eta}{\bar z_0^2}\right)+\dots\ , \qquad \text{(F.13)}$$

$$v(|z_0|\to\infty) \simeq -\mathrm{i}\lambda\pi\frac{R^2}{4}\left(\frac{\eta}{z_0^2}-\frac{\bar\eta}{\bar z_0^2}\right)+\dots\ , \qquad \text{(F.14)}$$

$$\phi(|z_0|\to\infty) \simeq -\frac{R^2}{4}\left(\frac{\eta}{z_0}+\frac{\bar\eta}{\bar z_0}\right)+\dots\ , \qquad \text{(F.15)}$$

and we see that the integrand in (F.12) along C_0 vanishes too fast and the contour integral gives no contribution.

Close to the cut on the real axis we have

$$\rho(\tau=0^{\pm};-R<x<R) = \rho_0 - \frac{\eta+\bar\eta}{2} \mp \mathrm{i}\frac{\eta-\bar\eta}{2}\frac{x}{\sqrt{R^2-x^2}}\,, \quad \text{(F.16)}$$

$$v(\tau=0^{\pm};-R<x<R) = \mathrm{i}\lambda\pi\frac{\eta-\bar\eta}{2} \mp \lambda\pi\frac{\eta+\bar\eta}{2}\frac{x}{\sqrt{R^2-x^2}}\,, \quad \text{(F.17)}$$

$$\phi(\tau=0^{\pm};-R<x<R) = -\frac{\eta+\bar\eta}{2}x \pm \mathrm{i}\frac{\eta-\bar\eta}{2}\sqrt{R^2-x^2}\,. \quad \text{(F.18)}$$

Therefore

$$\begin{aligned}\partial_\eta\left(\mathcal{S}-\mathcal{S}_0\right) &= \int_{-R}^{R}\left[v(x,0^+)\phi_\eta(x,0^+) - v(x,0^-)\phi_\eta(x,0^-)\right]\mathrm{d}x \\ &= \frac{\lambda\pi^2R^2}{2}\bar\eta\,. \end{aligned} \quad \text{(F.19)}$$

Similarly, we have

$$\begin{aligned}\partial_{\bar\eta}\left(\mathcal{S}-\mathcal{S}_0\right) &= -\oint\left\{\left[v\,\phi_{\bar\eta}\right]\mathrm{d}x + \left[\left(\frac{v^2}{2} - \partial_\rho\left(\rho\epsilon\right)+\mu\right)\phi_{\bar\eta}\right]\mathrm{d}t\right\} \\ &= \frac{\lambda\pi^2R^2}{2}\eta\,. \end{aligned} \quad \text{(F.20)}$$

The derivative with respect to ρ_0 is a bit more complicated as it involves more terms. After a bit of algebra and an additional integration by parts we obtain:

$$\begin{aligned}\partial_{\rho_0}\left(\mathcal{S}-\mathcal{S}_0\right) &= -\oint\left\{\Big[v\left(\phi_{\rho_0}-x\right)\Big]\mathrm{d}x\right. \\ &\quad \left.+\left[\left(\frac{v^2}{2} - \partial_\rho\left(\rho\epsilon\right)+\mu\right)\left(\phi_{\rho_0}+x\right) + \left(\partial_{\rho_0}\mu\right)\phi\right]\mathrm{d}t\right\} \end{aligned} \quad \text{(F.21)}$$

where $\phi_{\rho_0}\equiv\partial_{\rho_0}\phi$. Substituting the behaviors (F.13-F.15) and (F.16-F.18), the integrals around the two contours gives equal but opposite results ($\pm\frac{1}{2}\lambda\pi^2(\eta+\bar\eta)R^2$), which means

$$\partial_{\rho_0}\left(\mathcal{S}-\mathcal{S}_0\right) = 0\,, \quad \text{(F.22)}$$

as one could have expected.

We can now integrate (F.11) using (F.19,F.20,F.22) to find

$$\mathcal{S}_{\mathrm{DFP}} = \mathcal{S}-\mathcal{S}_0 = \frac{1}{2}\,\lambda\,\pi^2\,\eta\,\bar\eta\,R^2\,. \quad \text{(F.23)}$$

Appendix G

Linearized Hydrodynamics and DFP

Let us linearize the hydrodynamic equations, by expanding the theory and retaining only the quadratic part of the Lagrangian. This *linearized hydrodynamics* is usually referred in the literature on one-dimensional models as *bosonization*.

From the previous section, we have that the gradientless hydrodynamic Lagrangian for a one-component system is

$$\mathcal{L}[j,\rho] = \frac{j^2}{2\rho} + \rho\Big[\epsilon(\rho) - \mu\Big] \,, \tag{G.1}$$

where $j = \rho v$. We expand the fields around a background value and we parametrize the fluctuations around this background through the *displacement field* ϕ as in (F.5), so that the constraint (F.4) is automatically satisfied. Keeping terms up to the quadratic order we have

$$\begin{aligned} \mathcal{L}[\phi] &= \frac{1}{2\rho_0}\left(\partial_\tau\phi\right)^2 + \frac{1}{2}\partial_\rho^2\left(\rho\epsilon\right)_{\rho=\rho_0}\left(\partial_x\phi\right)^2 + \rho_0\Big[\epsilon(\rho_0) - \mu\Big]\ldots \\ &= \frac{\kappa}{2u}\left(\partial_\tau\phi\right)^2 + \frac{\kappa\, u}{2}\left(\partial_x\phi\right)^2 + \mathcal{L}[0,\rho_0] + \ldots \,, \end{aligned} \tag{G.2}$$

where in the last line we introduce the standard parameters of bosonization: the interaction parameter $\kappa = \kappa(\rho_0)$ and the sound velocity $u = u(\rho_0)$. The

displacement field evolves according to a linear wave equation:

$$\partial_\tau^2\phi + u^2\partial_x^2\phi = 0 \; . \tag{G.3}$$

The linearized treatment is valid for small fluctuations around the background ρ_0, i.e. as long as the gradients of ϕ are small and only low energy excitations are involved. For this reason, it is not possible to calculate the EFP through standard bosonization, but we can consider a DFP with very small depletion.

It is simple to see [65] that the solution that satisfies the DFP boundary conditions is of the form:

$$\phi(\tau, x) = \mathrm{Re}\left[\eta\left(\sqrt{z_0^2 - R^2} - z_0\right)\right] \; , \tag{G.4}$$

where $z_0 \equiv x + \mathrm{i}u(\rho_0)\tau$. For this solution to be compatible with the linearized approximation we need $|\eta|/\rho_0 \ll 1$.

It is easy to calculate the DFP by evaluating the linearized action

$$\mathcal{S} - \mathcal{S}_0 \simeq \int \mathrm{d}x\mathrm{d}\tau \left\{\frac{\kappa}{2u}\left(\partial_\tau\phi\right)^2 + \frac{\kappa\, u}{2}\left(\partial_x\phi\right)^2\right\} \tag{G.5}$$

on the solution (G.4). One immediately observes that, at zero temperature, this action does not depend on the sound velocity, as we can rescale the time as $y \equiv u\tau$:

$$\mathcal{S} - \mathcal{S}_0 \simeq \frac{\kappa}{2}\int \mathrm{d}x\mathrm{d}y \left\{\left(\partial_y\phi\right)^2 + \left(\partial_x\phi\right)^2\right\} \; . \tag{G.6}$$

We can further rescale the lengths by R and substituting (G.4) in (G.6) we get

$$\mathcal{S} - \mathcal{S}_0 \simeq \frac{\kappa}{2}\,\eta\bar{\eta}R^2 \int \mathrm{d}\tilde{x}\mathrm{d}\tilde{y} \left|\tilde{\phi}'(\tilde{x} + \mathrm{i}\tilde{y})\right|^2 \; , \tag{G.7}$$

where

$$\tilde{\phi}(z) = \sqrt{z^2 - 1} - z \; . \tag{G.8}$$

Now all the physical parameters have been explicitly extracted and one has just to perform an integral that contributes only with a numerical factor. The result is

$$\mathcal{S} - \mathcal{S}_0 \simeq \frac{\pi}{2}\,\kappa\,\eta\,\bar{\eta}R^2 \; . \tag{G.9}$$

Since for a Calogero-Sutherland system $\kappa = \lambda\pi$, we notice that (G.9) exactly coincide with (F.23). This is quite surprising, since, as we argued above, the linearized result should be trusted to be approximately correct only for small depletions. However, the Calogero kind of interaction is very special and we can extend (G.9) to higher depletion, without loosing accuracy. In section 5.8 we discuss the meaning of this observation. Let us remark that this result is specific for the EFP and it is not to say that for Calogero-Sutherland systems the effects of non-linearity are in general not important. For instance, effects of non-linear spin-charge interactions were observed and discussed in [15].

This DFP calculation can also be performed using the line integral technique explained in the previous section. In this case, the variation of the action (G.5) gives simply:

$$\begin{aligned} \partial_\eta \left(\mathcal{S} - \mathcal{S}_0 \right) &\simeq \oint \left\{ \frac{\kappa}{u} \left(\partial_\tau \phi \right) \phi_\eta \, \mathrm{d}x + \kappa \, u \left(\partial_x \phi \right) \phi_\eta \, \mathrm{d}\tau \right\} \\ &= \kappa \oint \left\{ \left(\partial_y \phi \right) \phi_\eta \, \mathrm{d}x + \left(\partial_x \phi \right) \phi_\eta \, \mathrm{d}y \right\} . \end{aligned} \tag{G.10}$$

One can then proceed as we showed in the previous section to easily recover (G.9).

Appendix H

Analysis of the Ground State Entropy via the TBA Equations

Here it is demonstrated that the ground state entropy of the double dot system at zero temperature is zero and thus the ground state is a singlet. The procedure outlined below can be found for a single dot in Section 8.3.3 of Ref. [139].

We start with the observation that the free energy of the system can be expressed as sums over all excitations in the system, that is, over all possible solutions of the Bethe ansatz equations (see Eqn. 10 of Ref. [3]). Specifically it takes the form

$$\Omega = E - TS, \tag{H.1}$$

where the energy of the system equals

$$E = \int dk \rho(k) k + \sum_{n=1}^{\infty} \int d\lambda \sigma_n'(\lambda) \epsilon_{0n}(\lambda), \tag{H.2}$$

where

$$\begin{aligned} \epsilon_{0n}(\lambda) &= -n(2\epsilon_{d1} + U_1/2) + 2\int_{-\infty}^{\infty} a_n(\lambda - g(k)) g(k) dk; \\ a_n(x) &= \frac{2}{\pi} \frac{1}{n^2 + 4x^2}; \end{aligned}$$

$$g(k) = \frac{(k-\epsilon_{d1}-\frac{U_1}{2})^2}{2U_1\Gamma_1}, \tag{H.3}$$

and the entropy, S, is given by

$$\begin{aligned} S &= \int dk\Big[(\rho(k)+\tilde{\rho}(k))\log(\rho(k)+\tilde{\rho}(k)) - \rho(k)\log\rho(k) - \tilde{\rho}(k)\log(\rho(k))\Big] \\ &+\sum_{n=0}^{\infty}\Big[(\sigma_n(\lambda)+\tilde{\sigma}_n(\lambda))\log(\sigma_n(\lambda)+\tilde{\sigma}_n(\lambda)) - \sigma_n(\lambda)\log\sigma_n(\lambda) - \tilde{\sigma}_n(\lambda)\log(\sigma_n(\lambda))\Big] \\ &+\sum_{n=0}^{\infty}\Big[(\sigma'_n(\lambda)+\tilde{\sigma}'_n(\lambda))\log(\sigma'_n(\lambda) \\ &+ \tilde{\sigma}'_n(\lambda)) - \sigma_n(\lambda)\log\sigma'_n(\lambda) - \tilde{\sigma}'_n(\lambda)\log(\sigma'_n(\lambda))\Big]. \end{aligned} \tag{H.4}$$

Here $\rho(k), \sigma_n(\lambda)$, and $\sigma'_n(\lambda)$ are the particle densities while $\tilde{\rho}(k), \tilde{\sigma}_n(\lambda)$, and $\tilde{\sigma}'_n(\lambda)$ are the hole densities of the various excitations (i.e. solutions of the Bethe ansatz equations). The particle and hole densities can be shown to obey the following equations:

$$\tilde{\rho}(k)+\rho(k) = \rho_0(k) - g'(k)\int d\lambda s(\lambda-g(k))(\tilde{\sigma}_1(\lambda)+\tilde{\sigma}'_1(\lambda)), \tag{H.5}$$

where

$$\begin{aligned} \rho_0(k) &= \frac{1}{2\pi}+\frac{1}{L}\Delta(k) + g'(k)\int d\lambda s(\lambda-g(k))(-\frac{1}{2\pi}\epsilon'_{01}(\lambda)+\frac{1}{L}\tilde{\Delta}_1(\lambda)); \\ \Delta(k) &= \frac{1}{2\pi}\partial_k\delta(k); \\ \tilde{\Delta}_n(\lambda) &= -\frac{1}{\pi}Re\Delta(\sqrt{2U_1\Gamma_1}(\lambda+\frac{in}{2})); \\ s(x) &= \frac{1}{2\cosh(\pi x)}, \end{aligned} \tag{H.6}$$

and

$$\begin{aligned} \tilde{\sigma}_n(\lambda)+\sigma_n(\lambda) &= \int d\lambda' s(\lambda-\lambda')(\tilde{\sigma}_{n+1}(\lambda')+\tilde{\sigma}_{n-1}(\lambda')) + \delta_{n1}\int dk\rho(k)s(\lambda-g(k)); \\ \tilde{\sigma}'_n(\lambda)+\sigma'_n(\lambda) &= \int d\lambda' s(\lambda-\lambda')(\tilde{\sigma}'_{n+1}(\lambda')+\tilde{\sigma}'_{n-1}(\lambda')) + D_n(\lambda), \end{aligned} \tag{H.7}$$

where

$$\begin{aligned} D_n(\lambda) &= \delta_{n1}\int dk\rho(k)s(\lambda - g(k)) \\ &- \int d\lambda' s(\lambda-\lambda'))(\tilde{\Delta}_{n+1}(\lambda') + \tilde{\Delta}_{n-1}(\lambda')); \end{aligned} \tag{H.8}$$

One sees that the density equations have source terms that involve a bulk piece and a piece scaling as $1/L$, where L is the system size.

One defines the energies of the excitations at finite temperature via the relations,

$$\epsilon(k) = T\log(\frac{\tilde{\rho}(k)}{\rho(k)});\ \epsilon_n(\lambda) = T\log(\frac{\tilde{\sigma}_n(\lambda)}{\sigma_n(\lambda)});\ \epsilon'_n(\lambda) = T\log(\frac{\tilde{\sigma}'_n(\lambda)}{\sigma'_n(\lambda)}). \tag{H.9}$$

These energies are given by the relations $\epsilon(k), \epsilon_n(\lambda)$, and $\epsilon'_n(\lambda)$ which are governed by the equations,

$$\begin{aligned} \epsilon(k) &= k + \int d\lambda \epsilon_{01}(\lambda)s(\lambda - g(k)) + T\int d\lambda s(\lambda - g(k))\log\left(\frac{n(\epsilon_1(\lambda))}{n(\epsilon'_1(\lambda))}\right); \\ \epsilon_n(\lambda) &= \delta_{n1}T\int dk g'(k)s(\lambda - g(k))\log(n(-\epsilon(k))) \\ &\qquad -T\int d\lambda' s(\lambda-\lambda')\log(n(\epsilon'_{n-1}(\lambda))n(\epsilon'_{n+1}(\lambda))); \\ \epsilon'_n(\lambda) &= \delta_{n1}T\int dk g'(k)s(\lambda - g(k))\log(n(\epsilon(k))) \\ &\qquad -T\int d\lambda' s(\lambda-\lambda')\log(n(\epsilon'_{n-1}(\lambda))n(\epsilon'_{n+1}(\lambda))), \end{aligned} \tag{H.10}$$

where $n(x) = (1+\exp(x/T))^{-1}$ is the Fermi function. The equations for the ϵ's and the bulk pieces of the densities (i.e. the pieces not scaling as $1/L$) are the same as for a single level dot. As noted in the manuscript, the Bethe ansatz equations for the double dots in parallel are identical to the single level dot up to the impurity scattering phase.

Substituting the energies and densities in the expression for the free energy,

one can rewrite it in a much more simple fashion:

$$\begin{aligned}
\Omega &= E_{gs} + T\int dk\rho_0(k)\log(n(-\epsilon(k))) + T\int d\lambda \sum_{n=0}^{\infty}\rho_{gs}^n(\lambda)\log(n(\epsilon_n'(\lambda)));\\
E_{gs} &= \sum_{n=0}^{\infty}\int d\lambda\epsilon_{0n}(\lambda)\rho_{gs}^n(\lambda);\\
\rho_{gs}^n(\lambda) &= \delta_{n1}\int\frac{dk}{2\pi}s(\lambda-g(k)) + \frac{1}{L}D_n(\lambda). \qquad \text{(H.11)}
\end{aligned}$$

Here E_{gs} is the ground state energy of the system.

One now wants to consider how Ω behaves at $T\to 0$. If one can show that the leading order correction in Ω at low temperatures is T^2 then as $S=-\partial_T\Omega$ one will have shown that the entropy vanishes as $T\to 0$, and so the ground state of the system is a singlet.

In order to see that Ω has no term linear in T, it is sufficient to consider the zero temperature values of the energies, $\epsilon(k)$ and $\epsilon_n'(\lambda)$. At the particle-hole symmetric point, one has

$$\begin{aligned}
\epsilon(k,T=0)>0 \quad &, \quad \text{for all k;}\\
\epsilon_1'(\lambda,T=0)<0 \quad &, \quad \text{for all } \lambda;\\
\epsilon_n'(\lambda,T=0)=0 \quad &, \quad n>1, \text{ for all } \lambda. \qquad \text{(H.12)}
\end{aligned}$$

If one substitutes these expressions into the expression for Ω and uses the fact that $\int d\lambda\rho_{gs}^n(\lambda)=0$, $n>1$, one sees that $\Omega = E_{gs}+\mathcal{O}(T^2)$.

Now if one is away from the particle-hole symmetric point, one has instead

$$\begin{aligned}
\epsilon(k,T=0)>0 \quad &, \quad \text{for all k;}\\
\epsilon_n'(\lambda,T=0)=n(\frac{U_1}{2}+\epsilon_1) \quad &, \quad \text{for all } \lambda. \qquad \text{(H.13)}
\end{aligned}$$

Now while $\epsilon_1'(\lambda)$ is neither solely positive nor solely negative at zero temperature, its leading order finite temperature correction is (see Section 8.3.7 of Ref. [139]),

$$\epsilon_1'(\lambda,T)=\epsilon_1'(\lambda,T=0)+\mathcal{O}(T^2). \qquad \text{(H.14)}$$

Substituting these forms of the energies into the expression for the free energy, one again sees that there is no term in Ω that is linear in T.

Appendix I

Derivation of the Conductance in SBMFT

Here we present a derivation of the conductance in the general case of asymmetrically coupled dots. To determine the conductance we solve the one-particle Schrödinger equation of the SBMFT Hamiltonian, $H_{SBMFT}|\psi\rangle = E|\psi\rangle$ where $|\psi\rangle$ equals

$$\begin{aligned} |\psi > &= \int_{-\infty}^{+\infty} dx g_1(x) c_1^\dagger(x)|0> + \int_{-\infty}^{+\infty} dx g_2(x) c_2^\dagger(x)|0> \\ &+\epsilon_1 d_1^\dagger|0> +\epsilon_2 d_2^\dagger|0> . \end{aligned} \tag{I.1}$$

This gives the following four equations:

$$\begin{aligned} -i\partial_x g_1(x) + \epsilon_1 \tilde{V}_{11}\delta(x) + \epsilon_2 \tilde{V}_{12}\delta(x) &= E g_1(x); & \text{(I.2)} \\ -i\partial_x g_2(x) + \epsilon_1 \tilde{V}_{21}\delta(x) + \epsilon_2 \tilde{V}_{22}\delta(x) &= E g_2(x); & \text{(I.3)} \\ (\tilde{\epsilon}_{d_1} - E)\,\epsilon_1 + \tilde{V}_{11} g_1(0) + \tilde{V}_{21} g_2(0) &= 0; & \text{(I.4)} \\ (\tilde{\epsilon}_{d_2} - E)\,\epsilon_2 + \tilde{V}_{22} g_2(0) + \tilde{V}_{12} g_1(0) &= 0. & \text{(I.5)} \end{aligned}$$

We then take the functions $g_{1,2}(x)$ found in the one particle wavefunction $|\psi\rangle$ to be of the following form:

$$\begin{aligned} g_1(x) &= e^{iEx}\left(\theta(-x) + R_{11}\theta(x)\right); & \text{(I.6)} \\ g_2(x) &= e^{iEx}\theta(x) T_{12}. & \text{(I.7)} \end{aligned}$$

Substituting the ansatz (Eqns. I.6 and Eq. I.7) into the above four equations, we obtain four equations from which one can solve for T_{12}. The conductance G, equal to $G = \frac{2e^2}{h} T_{12} T_{12}^*$, is then

$$\begin{aligned} G &= \frac{2e^2}{h}\frac{N}{D} \\ N &= 16\left[\tilde{V}_{12}\tilde{V}_{22}\tilde{\epsilon}_{d_1} + \tilde{V}_{11}\tilde{V}_{21}\tilde{\epsilon}_{d_2}\right]^2 \\ D &= 8\left[\tilde{V}_{11}\tilde{V}_{12} + \tilde{V}_{21}\tilde{V}_{22}\right]^2 \tilde{\epsilon}_{d_1}\tilde{\epsilon}_{d_2} + 16\tilde{\epsilon}_{d_1}^2\tilde{\epsilon}_{d_2}^2 + \left[\tilde{V}_{12}\tilde{V}_{21} - \tilde{V}_{11}\tilde{V}_{22}\right]^4 \\ &\quad + 4\tilde{\epsilon}_{d_1}^2\left[\tilde{V}_{12}^2 + \tilde{V}_{22}^2\right]^2 + 4\tilde{\epsilon}_{d_2}^2\left[\tilde{V}_{11}^2 + \tilde{V}_{21}^2\right]^2. \end{aligned} \tag{I.8}$$

We have also computed the transmission amplitude using Ref. [157]:

$$T = \mathrm{Tr}\left\{G^a \tilde{\Gamma}_R G^r \tilde{\Gamma}_L\right\}, \tag{I.9}$$

where $G^{a/r}$ are advanced and retarded Green's function matrix and $\tilde{\Gamma}_R$ and $\tilde{\Gamma}_L$ are defined by

$$\tilde{\Gamma}_R = \begin{bmatrix} \tilde{V}_{21}^2 & \tilde{V}_{21}\tilde{V}_{22} \\ \tilde{V}_{21}\tilde{V}_{22} & \tilde{V}_{22}^2 \end{bmatrix}, \qquad \tilde{\Gamma}_L = \begin{bmatrix} \tilde{V}_{11}^2 & \tilde{V}_{11}\tilde{V}_{12} \\ \tilde{V}_{11}\tilde{V}_{12} & \tilde{V}_{12}^2 \end{bmatrix}. \tag{I.10}$$

We find that this trace formula (Eq. I.9) gives exactly the same result.

Appendix J

SBMFT for double dots in the symmetric case

In this appendix we review the SBMFT approach for the symmetric case ($\epsilon_{d1} = \epsilon_{d2} \equiv \epsilon_d$). In this limit, the mean field equations (Eq. 6.7 and Eq. 6.8) reduce to

$$\sum_{\sigma} < f_{\sigma}^{\dagger}(t) f_{\sigma}(t) > + r^2 = 1 \tag{J.1}$$

$$\sqrt{2}\tilde{V}\mathrm{Re}\left[\sum_{k,\sigma}\left\langle c_{ke\sigma}^{\dagger}(t) f_{\sigma}(t)\right\rangle\right] + i\lambda r^2 = 0. \tag{J.2}$$

The above equations can be equivalently written as

$$\frac{1}{2\pi}\sum_{\sigma}\int d\omega < f_{\sigma}^{\dagger}(\omega) f_{\sigma}(\omega) > + r^2 = 1$$

$$\frac{\sqrt{2}\tilde{\mathrm{V}}}{2\pi}\mathrm{Re}\left[\sum_{\sigma}\int d\omega \left\langle c_{ke\sigma}^{\dagger}(\omega) f_{\sigma}(\omega)\right\rangle\right] + i\lambda r^2 = 0$$

The correlation functions turn out to be

$$< f_{\sigma}^{\dagger}(\omega) f_{\sigma}(\omega) >= \frac{2\tilde{\Delta}}{\left(k - \tilde{\epsilon}_d\right)^2 + 4\tilde{\Delta}^2} F(\omega) \tag{J.3}$$

$$\left\langle c_{ke\sigma}^{\dagger}(\omega) f_{\sigma}(\omega)\right\rangle = \frac{\sqrt{2}\tilde{V}}{k - \tilde{\epsilon}_d - 2i\tilde{V}^2} F(\omega) \tag{J.4}$$

where $F(\omega)$is a Fermi-function.

Upon substituting these expressions for correlation functions the mean field equations read

$$\frac{\tilde{\Delta}}{\Delta} - 1 + \frac{1}{\pi}\arctan[\frac{2\cdot\tilde{\Delta}}{\tilde{\epsilon}_d}] = 0 \tag{J.5}$$

$$\frac{\tilde{\epsilon}_d - \epsilon_d}{\Delta} + \frac{1}{\pi}\log[\frac{(\tilde{\epsilon}_d^2 + 4\cdot\tilde{\Delta}^2)}{D^2}] = 0 \tag{J.6}$$

Notice that the SBMFT equations (Eq. J.5 and Eq. J.6) for double dots are strikingly similar to the single-dot case which differ from the above just by different coefficents (for single dot/impurity see Ref. [144]). However, it is this slight difference in coefficients that gives rise to completely different physics in the Kondo regime for the double dots. To ellaborate this point we will compute the conductance which is given by $G = 2\frac{e^2}{h}\sin^2\left(\frac{\delta(k=0)}{2}\right)$ where $\delta(k) = -2\tan^{-1}\left(\frac{2\tilde{\Delta}}{k-\tilde{\epsilon}_d}\right)$. In the Kondo limit, $\tilde{\Gamma}\to 0$ and hence Eq. J.5 becomes $\tan^{-1}\left(\frac{2\tilde{\Gamma}}{\tilde{\epsilon}_d}\right) = \pi$. Since we know that the conductance is given by $G = \frac{2e^2}{h}\sin^2\left[\tan^{-1}\left(\frac{2\tilde{\Gamma}}{\tilde{\epsilon}_d}\right)\right]$ this immediately tells us that linear conductance vanishes in the Kondo limit. One should bear in mind that the three results in the Kondo limit, namely, $\tilde{\Gamma}\to 0$, $\tilde{\epsilon}_d\to 0$ and $\tan^{-1}\left(\frac{2\tilde{\Gamma}}{\tilde{\epsilon}_d}\right) = \pi$ are consistent with each other as long as one takes the correct branch-cut for arctangent, namely, the branch, $\tan^{-1}x = \pi + \mathrm{PV}\left[\tan^{-1}x\right]$ where PV denotes the principle value of arctangent which belongs to domain $[-\frac{\pi}{2}, \frac{\pi}{2}]$. The vanishing of conductance in the double dot case is a result of $\tilde{\Delta}$ falling off to zero faster than the magnitude of the renormalized energy level does.